CORRELATION BETWEEN ELASTIC AND THERMAL PROPERTIES OF CHALCOGENIDE MEMORIES BY SURFACE BRILLOUIN SCATTERING

Mmapula Baloi

A dissertation submitted to the Faculty of Science, University of the Witwatersrand, Johannesburg,
in fulfilment of the requirements for the degree of
Master of Science.

June 9, 2019

Declaration

I, Mmapula Baloi, declare that the dissertation entitled "Correlation Between Elastic and Thermal Properties of Chalcogenide Memories by Surface Brillouin Scattering" is my own unaided work. It is being submitted to the University of the Witwatersrand for the degree of Master of Science. This work has not been submitted before for any degree or examination purposes in any other University. Moreover, where assistance has been received, this will be clearly stated and acknowledged.

Signature: 

Date: 09/06/2019

Abstract

Phase change materials based on Ge-Sb-Te are of technological importance due to their successful commercial application for optical recording. These alloys are also candidates for emerging phase change random access memory (PRAM) devices, which aims at bridging the memory gap as found in modern Von Neumann's computer architecture. However, setbacks such as the high reset programming current and the amorphous resistance drift phenomenon hinder the successful implementation of this technology. Thus said, this study aims to understand the origin of thermal management in PRAM devices as associated with these problems, from a phonon point of view.

Two technologically important chalcogenide alloys, $Ge_2Sb_2Te_5$ and GeTe were studied using various material characterization techniques. The main aim of this study was to find the correlation between the elastic properties and the lattice thermal conductivity of the two alloys by using surface Brillouin scattering (SBS) as the main investigative tool. Thin films were prepared using radio frequency (RF) magnetron sputtering at room temperature. As-deposited, the films have a disordered structure. Crystallization was induced by thermal annealing in a furnace in an Argon atmosphere at various temperatures.

The film's thickness and mass density were scrutinized by X-ray reflectivity (XRR). Thickness reduction associated with density increase upon structural transformation was evident. This was one of the expected characteristics of PCMs. The Rutherford Backscattering spectrometry (RBS) probe of the tandem linear accelerator at iThemba LABS (Gauteng), was used to determine the atomic density and chemical composition, by irradiating the films with 3.6 MeV He^{2+} particles. Energy dispersive X-ray spectroscopy (EDS) coupled with field emission scanning electron microscopy (FESEM) was used as a complementary technique to RBS for verifying the chemical composition. The crystal structures of the annealed films were confirmed by grazing incidence X-ray diffraction (GIXRD). The optical and acoustic modes of the two materials were studied by micro-Raman spectroscopy and SBS. The optical vibration modes provided additional information about the chemical bonding present in different structural phases.

SBS measurements allow one to derive phonon velocity dispersion curves which were fitted with the surface elastodynamic Green's function for extrac-

tion of two independent elastic constants, C_{11} and C_{44}, respectively. Subsequently, other engineering moduli were determined from the elastic constants, C_{11} and C_{44}. In general, the results suggest progressive elastic stiffening between the amorphous and crystalline phases of $Ge_2Sb_2Te_5$ and GeTe. This was also supported by the values of the longitudinal and transverse velocities. In general, both $Ge_2Sb_2Te_5$ and GeTe exhibit low thermal conductivities in all structural phases. The low thermal conductivity of $a - Ge_2Sb_2Te_5$ encourages good thermal management of PRAM devices during programming. The higher lattice thermal conductivity of $a-$GeTe compared to $c-$GeTe, could be the reason for its instability and hence the drift behaviour observed in PRAM applications. This is not good for data retention and the cyclability of the device. Thus new ways of reducing the lattice thermal conductivity must be employed and further studies on these properties must be done to provide more insight.

Acknowledgements

I would like to thank God Almighty for granting me this opportunity to carry-out this research; Your forever presence in the journey of my life means a lot to me! To my supervisor, Prof. Daniel Wamwangi, thanks for your time, advice, suggestions and sharing your knowledge with me. Even though I never mentioned this before, you gave me hope and reason to continue with this work at times when I have already given up. This gave me encouragement to finish what I have started; now it is done and it is all thanks to you. It has not been easy completing this work with all the challenges I have faced in the past two years. I would not have chosen a different supervisor other than you; thank you for taking me in as your student. Appreciation is also granted to co-supervisor Dr. Bhekumusa Mathe for the fruitful suggestions regarding surface Brillouin Scattering.

Special gratitude to Dr. Rudolph Erasmus for performing Raman micro-spectroscopy measurements. I would also love to thank the NRF iThemba LABS (Gauteng) for giving me permission to use the Rutherford Backscattering spectrometer (RBS) facility. Appreciation is granted to Dr. Morgan Madhuku and Dr. Phillip Sechogela for carrying out RBS measurements and introducing me to RBS analysis methods. The Schools of Chemistry, Physics and, Chemical and Metallurgical engineering are thanked for providing access to their research facilities. Last but not least, this section will not be complete without thanking the following people. Adam, your patience and time while undertaking training to operate the X-ray reflectivity equipment is appreciated. Dr. Francis Otieno, your suggestions and advices regarding magnetron sputtering and thermal annealing were useful in sample preparation for this and certainly, for future work. Wilfred, Hlosani and Charsline for the useful discussion we had in office PM4. My fellow collegues in office PM5, Sandile, Chad, Tresor, Tahir and Khaled for being there when I need help.

To my friends, Kamogelo, Mpho and Lerato, my sisters, Mary, Hellen and Emily for their support. Many thanks to Armand for accommodating me in your busy work schedule; much appreciation for assistance in compiling this work in LaTEX, this skill will never be forgotten. To my former mentor, Dr. Emily Aradi, thanks for sharing your time, love and wisdom with me. You are more than a sister to me, may God bless you. Thanks to my father, Ernest, for encouragement and lastly, I would love to dedicate this dissertation to my late

mother, Christinah. The University of the Witwatersrand and the DST/NRF Centre of Excellence in Strong Materials (CoE-SM) are highly acknowledged for financial assistance that made this work to be possible. Note that the views expressed in this work are not necessarily of the DST/NRF CoE-SM but of the author.

Contents

List of Abbreviations

MOSFETS	Metal Oxide Semiconductor Field Effect Transistor
CMOS	Complementary Metal Oxide Semiconductors
SCM	Storage Class Memory
DRAM	Dynamic Random Access Memory
HDD	Hard Disk Drives
MRAM	Magnetic Random Access Memory
FeRAM	Ferroelectric Random Access Memory
RRAM	Resistive Random Access Memory
PCRAM	Phase Change Random Access Memory
PRAM	Phase Change Random Access Memory
PCM	Phase Change Materials and or Phase Change Memory
CD	Compact Discs
DVD	Digital Versatile Discs
BD	Blue-ray Discs
HDDVD	High Definition Digital Versatile Discs
MLC	Multi-Level Cell
IBM	International Business Machines corporation
BLS	Brillouin Light Scattering
SBS	Surface Brillouin Scattering
RBS	Rutherford Backscattering Spectrometry
XRR	X-ray Reflectometry

XRD ..... X-ray Diffraction

GIXRD ..... Grazing Incidence X-Ray Diffraction

SEM ..... Scanning Electron Microscopy

FESEM ..... Field Emission Scanning Electron Microscopy

EDS ..... Energy Dispersive X-ray Spectroscopy

EDX ..... Energy Dispersive X-ray spectroscopy

WDX ..... Wavelength Dispersive X-ray spectroscopy

XPS ..... X-ray Photoemission Spectroscopy

PIXE ..... Particle-Induced X-ray Emission

AS ..... Auger Spectroscopy

BSD ..... BackScatter Detector

FTIR ..... Fourier Transform Infrared Spectroscopy

CCD ..... Charge Coupled Detector

RF ..... Radio Frequency

MCA ..... Multi-Channel Analyzer

DPSS ..... Diode Pumped Solid State laser

SLM ..... Single Longitudinal Mode

TEM ..... Transverse Electro-Magnetic

FPI ..... Fabry-Perot Interferometer

TFPI ..... Tandem Fabry-Perot Interferometer

FSR ..... Free Spectral Range

AOM ..... Acouto-Optic Modulator

SAW ..... Surface Acoustic Waves

AM ..... Acoustic Microscopy

LSAW ..... Laser-generated Surface Acoustic Wave

RSAW ..... Rayleigh Surface Acoustic Wave

SW ..... Sezawa Waves

AC ..... Alternating Current

DC ..... Direct Current

PVD ..... Physical Vapor Deposition

CVD ..... Chemical Vapor Deposition

SIMNRA ..... Simulation of Nuclear Reaction Analysis

CPS ..... Counts Per Second

DFT ..... Density Functional Theory

DFPT ..... Density Functional Perturbation Theory

LDA ..... Local Density Approximation

TDTR ..... Time Domain Thermoreflectance

List of Figures

List of Tables

Chapter 1

Introduction

1.1 Motivation

The current semiconductor industry has been dominated by silicon based electronic devices for data processing. In the past three decades we have seen a trend in diminishing size of electronic devices in order to fulfil the demand for high density nano-sized devices with fast processing speeds. This has seen silicon reaching its scaling limits in conformity to Moore's Law [16]. Therefore, there is a need to find alternative technologies to replace the metal oxide semiconductor field effect transistors (MOSFETs). Data processing has become very slow due to the scaling of MOSFETs and nowadays modern computers are facing the problem known as the Von Neumann bottleneck. One of the emerging technologies that can solve this problem is the storage class memory (SCM) [16].

Storage class memory is a kind of memory/storage hybrid technology that aims at bridging the gap between main and secondary memories in the computer memory/storage hierarchy [16]. Candidates within SCM technology are non-volatile solid state memories such as resistive random access memory (RRAM), phase change RAM (PCM or PRAM), Ferroelectric RAM (FeRAM) and Magnetorestive RAM (MRAM) [4]. Figure 1.1 shows the storage capacity of these SCM technologies in comparison to that of NAND flash memory. PRAM has gained a lot of attention in the last two decades due to its non-volatility, high operating speed and scaling capabilities [16], [17]. It is envisioned to bridge the latency gap between Dynamic RAM (DRAM) and NAND flash memory [16], [4], [5].

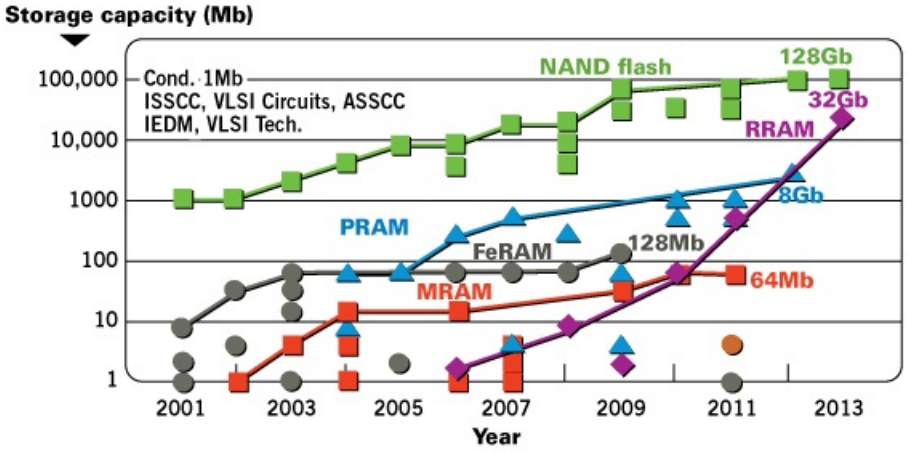

Figure 1.1: Storage capacity trend of emerging SCM candidates with NAND flash technology. [4]

Phase change materials (PCMs) are chalcogenide alloys based on tellurium (Te), and contain elements such as Germanium (Ge) and Antimony (Sb) to stabilize their random network. Typical PCMs are found on the pseudo-binary tie line of GeTe and Sb_2Te_3 in the ternary phase diagram of Ge-Sb-Te as shown in Figure 1.2. Elements such as Silver (Ag), Bismuth (Bi), Indium (In), Tin (Sn), Arsenic (As) and other chalcogens, can be used as stabilizing dopants to obtain eutectic binary alloy systems [2]. These chalcogenide glasses are classified as amorphous semiconductors and are poor glass formers. [18], [19].

However, this idea of chalcogenide memories is not new as amorphous semiconductors have been studied in the past, dating back to the 1960s [20]. It was S.R. Ovshinsky (1968) who found that amorphous semiconductors can be reversibly switched between a conductive and a highly resistive state by an electric field [21]. These states are structural phases, amorphous and crystalline, and constitute different electronic properties. It was found that the amorphous phase is highly resistive whilst the crystalline phase is semiconducting. It is these structural and electrical properties that made phase change materials good candidates for data storage [20].

1.2 Phase Change Materials: Principle, Applications and Challenges

Phase change materials can exist in the disordered phase (amorphous) with a driving force for recrystallization into a highly symmetric, metastable Sodium chloride (NaCl) like structure and a more thermodynamically stable, hexagonal phase [2], [19], [22]. Thus the mechanism of kinetic crystallization is usually used to classify these materials into two categories, namely nucleation-

and growth-dominated mechanisms. In the former category, crystallization proceeds by formation of homogeneous nuclei in the matrix that subsequently grow into a preferred phase through thermal activation. In the latter category, growth proceeds via the crystal rim of the volume matrix [19]. Nucleation-dominated materials are Ge-Sb-Te alloys with stoichiometric composition derived from GeTe and Sb_2Te_3 components along the pseudo-binary tie line, that is, $(GeTe)_m(Sb_2Te_3)_n$, where m, n are integers, respectively. Examples of growth-dominated materials are GeSb and binary eutectic Sb-Te compounds with lesser amounts of Ag, In and or Ge, and tend to form stoichiometric quaternary $AgIn - Sb_2Te$ alloys.

Application in optical recording media relies on the optical properties of PCMs. The optical reflectance contrast between the amorphous and crystalline phases plays an important role in optical data storage. The amorphous phase has a low reflectivity while the crystalline phase is highly reflective [2]. According to Wuttig and Yamada (2007), a change in this optical property tends to increase in Ge-rich alloys (that is, in nucleation-dominated materials) [3]. The first optical product was produced commercially two decades after Ovshinsky's discovery of the reversible switching effect. This resulted in the discovery of other PCMs for applications in rewritable optical storage media such as compact discs (CDs), digital versatile discs (DVDs). The discovery of Blu-ray disc (BD) technology or high-definition DVD (HD-DVD) in the early 2000s saw the storage capacity increasing by a factor of 100 times compared to DVDs [23]. BD technology's storage capacity was improved by optimizing the optical reflectivity for shorter laser wavelengths (in the blue and violet region) in the visible light range of the electromagnetic spectrum [3].

Since optical data storage is dependent on the application of a laser pulse (this is because the storage density is inversely proportional to the laser wavelength) to reversibly switch the multiple states of PCMs, this technology is disadvantaged by the diffraction limit of visible light. Currently, wavelengths of 780nm, 650nm and 405nm are being used in CDs, DVDs and BDs, respectively [3], [19]. However, the use of local photon scattering (effect of plasmonic resonance) in super resolution near-field structure (super-RENS) discs has been implemented in overcoming this setback [3], [19]. The commercial success of applying PCMs for data storage sparked an interest in developing electronic solid state memory devices based on PCMs (PRAM), which takes advantage of the reversible switching phenomena due to Ovshinsky [21], [22]. Figure 1.2 illustrates the typical PCMs and historical discovery of commercial optical products and prototypes of PRAM devices developed thus far [2].

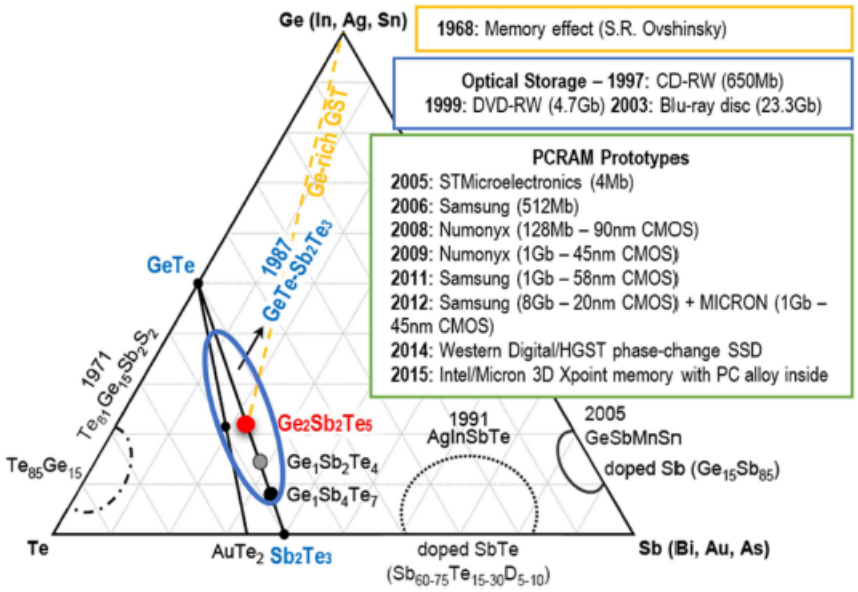

Figure 1.2: Phase diagram of Ge-Sb-Te showing the materials used for applications in optical storage and for PRAM devices.[2]

Phase change random access memory depends on the change in electrical resistivity upon structural transformation between the amorphous and crystalline phases; this is known as memory switching. The amorphous phase is highly resistive whereas the crystalline phase is highly conductive. Therefore, data can be stored by reversibly switching between the two states using current pulses of different magnitudes and duration [5]. This phenomenon makes PRAM to be non-volatile; this is the ability of a memory device to preserve information in the absence of power or an applied electric field.

However, memory switching cannot take place without threshold switching. This effect occurs on sub-nanosecond time scales and manifests itself during current-voltage characterization of PRAM devices, as shown in Figure 1.3. This figure shows that upon application of a voltage, the amorphous phase remains highly resistive (amorphous OFF). Only when the applied voltage reaches a certain value known as the threshold switching voltage, the resistance of the amorphous phase decreases (amorphous ON). Due to heat dissipation, the amorphous phase crystallizes via Joule's heating [5]-[16]. Essentially, threshold switching is due to negative-differential resistance which can be explained by several models, such as impact ionization and Shockely-Hall-Read recombination, Poole-Frenkel transport mechanism, amongst others (for further details, see Ref. [22])

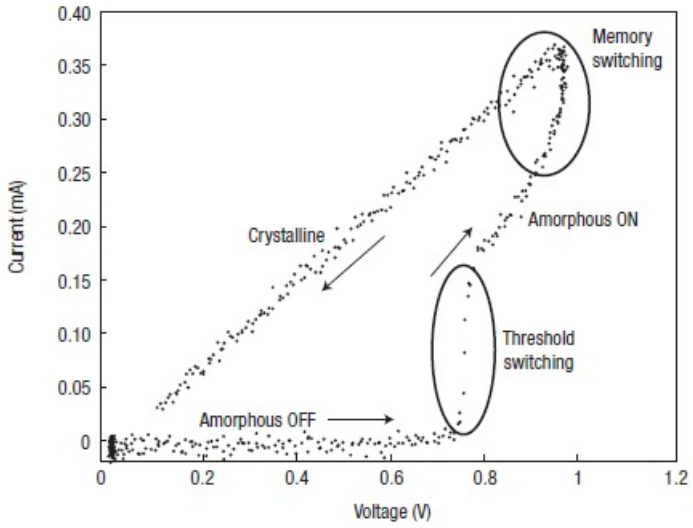

Figure 1.3: Typical current-voltage characteristics of PCMs illustrating the concepts of threshold and memory switching, respectively.[3]

The principle of electronic switching plays an important role for data storage in PRAM devices. This is governed by the WRITE, ERASE and READ processes during programming of the memory device, as shown in Figure 1.4. In the WRITE process, a short intense current pulse is applied to the material to induce local melting above the melting temperature of the material. Then the melt is quenched very fast before it crystallizes to engender disorder; this is the amorphization process or RESET operation. It is during this process where a change in electrical resistivity (as well as optical reflectivity) is observed upon structural transition from the crystalline to amorphous phases respectively [5]-[16].

PCMs are characterized as poor glass formers due to their temperature dependent activation energy in the under-cooled region. However, their low recrystallization temperature makes them good candidates for memory applications [18], [19]. In the ERASE process or SET operation, a long duration, moderate current pulse is used to heat the amorphous phase above the glass transition but below the melting temperature to recrystallize the material. Then data is read (and stored) as binary "0" (RESET state) or "1" (SET state) by an intermediate current pulse to differentiate the electrical resistivity between the two states; this is the READ process. A decrease in electrical resistivity up to three orders in magnitude has been observed between the two phases [5]-[16].

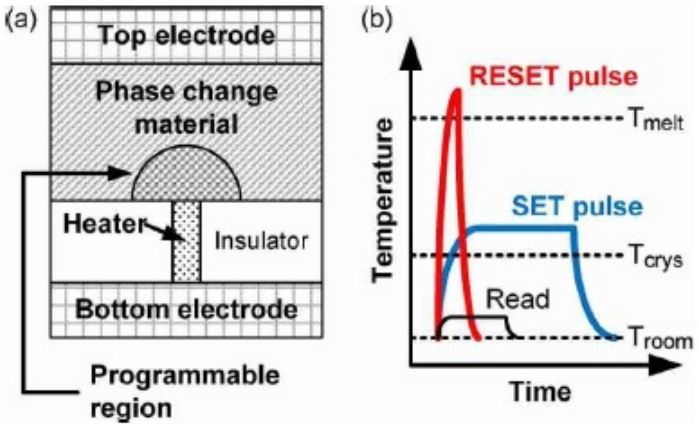

Figure 1.4: (a)The mushroom architecture of the PRAM cell, and (b) temperature-time profile illustrating the SET-RESET operation using current pulses during programming of the cell. Adapted from Refs. [4] and [5]

The number of times that the WRITE-ERASE-READ processes can be cycled or repeated determines the latency of a memory device. For PRAM to be a viable SCM technology, its latency must match that of DRAM, which is in the order of 10^{16} and this is still a challenge [20]. Nevertheless, PRAM has the capability of replacing NOR flash memory and has a good latency of about $10^9 - 10^{11}$. The industry also requires fast switching speeds, hence shorter recrystallization times during programming of the memory cell [5]-[16]. This is a challenge for this technology since the ERASE process is a time limiting process, due to the long duration current pulse needed to recrystallize the material. Also, the highly resistive amorphous phase limits the SET current when phase transition is induced. However, this can be overcome by threshold switching phenomena [18].

Another requirement that PRAM must fulfil is that the amorphous phase must be thermally stable against spontaneous recrystallization for high data retention. Therefore, the resistance drift behaviour in the amorphous phase during programming, could induce degradation of the material. This phenomenon is the increase in resistivity of the RESET state over time attributed to the structural relaxation of weaker bonds [5]. The consequences of this behaviour is that it leads to poor data retention and inhibits multi-level cell (MLC) or multi-bit storage in PRAM [17]. Phase change alloys with high melting temperatures require RESET current of $\sim 100\mu$A [5]. This is high compared to the selector or access device (transistor or diode) which must be connected to the memory cell for programming purposes [4]. Thus the resulting high power consumption ($\sim$ 45 pJ) poses a major challenge to this novel technology. This hinders fast memory switching and is not good for energy efficiency of the device [5]-[16].

One of the questions that arises is how the RESET switching current can be reduced to optimize the performance of PRAM cells. This has been addressed

by reducing the volume of the PCM that can be accessed during programming. This has been achieved by developing new device architectures such as the line cell (IBM), edge contact cell, a modified top bottom approach or mushroom cell (Samsung) and more recently, 3D X-point (Intel) [2], [22]. These approaches have led to a significant reduction in the RESET current. As seen from Figure 1.4(a), the design of the mushroom PRAM cell consists of the PCM sandwiched between the top and bottom electrodes that serve as current pathways for Joule's heating. Thus the contribution of the thermal conductivity κ must be known since it influences the thermal dissipation of the device [20].

Low thermal conductivities are desirable as they determine the energy efficiency of the memory device during programming and assist in reducing thermal losses. These materials have been shown to have significantly lower thermal conductivities (~ 0.25 and ~ 0.44 $Wm^{-1}K^{-1}$ for the amorphous and crystalline $Ge_2Sb_2Te_5$ films) than those of covalent semiconductors. For instance, GaAs and GaSb have κ of 45 and 60 $Wm^{-1}K^{-1}$ in their crystalline phases, respectively [24]. This could be related to the nature of chemical bonds which determine the vibrational properties [24]. Therefore, it is hypothesized that the correlation between the elastic and thermal properties in PCMs will provide insights of thermal management and thereby enhance PRAM performance. The thermoelastic properties of PCMs affect the mechanical properties, and subsequently the drift resistance in the amorphous phase.

1.3 Hypothesis, Aims and Objectives

An approach to understand the evolution of the resultant high RESET current and drift resistance in the amorphous phase is presented in this study. It is known that thermal energy can be stored in the vibrational normal modes of materials known as phonons. There are two types, acoustic and optical phonons, respectively. Acoustic modes are essentially elastic or sound waves propagating in a solid medium. Therefore, the thermal energy can be transported through the lattice by an appropriate wave packet of the normal modes [15]. Phonons are important for our understanding of elasticity, acoustics, thermal properties such as heat capacity and lattice thermal conductivity, and electrical resistivity in solids. Considering the above statements, the following question arises: how does the lattice thermal conductivity correlate with the elastic constants of phase change materials?

Thus the study aims to correlate the elastic properties with the lattice thermal conductivity of $Ge_2Sb_2Te_5$ and GeTe. Surface Brillouin scattering is therefore chosen in this work as a direct method of measuring elastic properties (acoustic phonon velocities and hence elastic constants). Therefore the following set of objectives are selected to validate the hypothesis:

- Perform surface Brillouin scattering (SBS) measurements on $Ge_2Sb_2Te_5$ and GeTe films with varying thickness; this is done to obtain the phonon velocity dispersion curve.
- Extract elastic constants from the phonon velocity dispersion curve in different structural phases of the two materials.
- Calculate the transverse and longitudinal velocities and other engineering moduli from two independent elastic constants as determined from the phonon velocity dispersion curve.
- Apply the Debye Model to calculate the minimum lattice thermal conductivity.
- Perform a comparative study of the elastic constants (since these are under-reported in literature) and lattice thermal conductivity between the structural phases of $Ge_2Sb_2Te_5$ and GeTe.

1.4 Dissertation Layout

This dissertation consists of six chapters. The first chapter started with the historical background of chalcogenide semiconductors. The related phase change materials based on Ge-Sb-Te are classified according to their mechanisms of kinetic crystallization. Their optical and electronic properties as well as their relation to optical recording and electronic memory applications are also discussed. The significant role of phase change alloys in surmounting the existing memory gap in computer memory hierarchy serves as an important motivation for this study as outlined in the previous section.

Chapter 2 starts with the fundamentals of elasticity and proceeds to the discussion of bulk and surface acoustic waves, and their means of propagation. Next, the theory of surface Brillouin scattering is outlined and attention is given to the two mechanisms governing the scattering of acoustic phonons, namely the surface ripple and elasto-optic mechanisms. Then the Green's function formalism is outlined. These concepts form the basis of this study and are important in the understanding of elastic properties of materials. The last section focuses on thermal transport in solids. The formulation of the Debye Model of the specific heat and the lattice thermal conductivity is given. This section concludes with Cahill's formulation of minimum lattice thermal conductivity of amorphous semiconductors. This model was used in this study to calculate the minimum lattice thermal conductivity of the two chalcogenide alloys, $Ge_2Sb_2Te_5$ and GeTe.

Chapter 3 discusses the experimental methods used for the growth and subsequent characterization of chalcogenide films. In this respect, the principle of radio frequency (RF) magnetron sputtering as the main technique used to

prepare the samples is discussed. This is followed by numerous non-destructive techniques used for film characterization, such as Rutherford Backscattering spectroscopy (RBS), X-ray reflectivity (XRR) and grazing incidence X-ray diffraction (GIXRD). Energy dispersive X-ray spectroscopy (EDS) coupled with field-emission scanning electron microscopy (FESEM) was also used as a complementary destructive technique to RBS for elemental analysis. The last section focuses on two techniques used to probe vibrational properties (phonon modes), namely Raman and surface Brillouin Scattering (SBS), respectively. These are direct methods widely used for probing optical and acoustic phonon modes in materials.

Chapter 4 is dedicated to structural characterization results of $Ge_2Sb_2Te_5$ and GeTe. Chapter 5 presents a comparative study by surface Brillouin scattering of the elastic properties of the structural phases of the two alloys. The first section discusses various surface acoustic modes measured by SBS. As outlined in section 5.2, the frequencies of these modes are important in deriving phonon velocity dispersion curves from which the isotropic elastic properties were determined. This is followed by the determination of the longitudinal and the transverse velocities in section 5.3. Lastly, a correlation of the elastic properties (particularly, the longitudinal and transverse velocities) and the lattice thermal conductivity is evaluated using the Cahill's Model.

A summary of the main results obtained in chapters 4 and 5 is given in chapter 6. Emphasis is placed on the differences in the material properties of the various structural phases, and recommendations on improving the study are also stated. Suggestions about how the study could help in improving thermal management in PRAM are also given. Lastly, the future prospects of these materials are discussed.

Chapter 2

Literature Review

This chapter gives the theoretical background related to the elastic and thermal properties of solids. It starts with the fundamentals of elasticity and proceeds to the discussion of bulk and surface acoustic waves, followed by how they propagate in a medium. Next, the principle of surface Brillouin scattering is outlined with a focus on two mechanisms governing the scattering of acoustic phonons, namely the surface ripple and elasto-optic mechanisms. This section is followed by the surface elastodynamic Green's Function approach; a useful way of predicting spectroscopic spectra. These past three topics form the basis of surface Brillouin scattering, the main investigative tool in this work. They are important in the understanding of elastic properties of opaque solids. The last section focuses on the formulation of the Debye Model of the specific heat and the lattice thermal conductivity. This section concludes with Cahill's formalism on minimum lattice thermal conductivity of disordered crystals. This model was used in this study to determine the minimum lattice thermal conductivity of chalcogenide memories.

2.1 Elasticity

The ability of a material to withstand stress whilst under strain is known as elasticity. It was a British Physicist Robert Hooke who realised that the deformation of an elastic material is related linearly to the applied force or stress [25]. In this section, the linear elasticity for a homogeneous anisotropic solid will be considered. The stress and deformation are defined by the stress tensor, σ_{ij} and strain tensor, ϵ_{ij}. The stress tensor is related to the force F_i the solid is subjected to [26] by the following relation

$$F_i = \frac{\partial \sigma_{ij}}{\partial x_j} \tag{2.1}$$

Strain causes deformation in a solid leading to changes in the displacement between two neighbouring points. The particle displacement vector, $\mathbf{u}$ is given by $\mathbf{u} = \mathbf{r}' - \mathbf{r}$ [27]. Thus the strain tensor can be expressed in terms of $\mathbf{u}$ such that:

$$\eta_{ij} = \frac{1}{2}\left(\frac{\partial u_i}{\partial x_j} + \frac{\partial u_j}{\partial x_i} + \frac{\partial u_i}{\partial x_j} \cdot \frac{\partial u_j}{\partial x_i}\right) \tag{2.2}$$

For small deformation of a solid, infinitesimal displacements are considered in the three dimensional elastic continuum theory and thus the last term in Equation 2.2 can be dropped, resulting in infinitesimal strain ϵ_{ij}:

$$\epsilon_{ij} = \frac{1}{2}\left(\frac{\partial u_i}{\partial x_j} + \frac{\partial u_j}{\partial x_i}\right) \tag{2.3}$$

Thus the tensor components of the stress applied to an elastic material are related to the strain tensor components by;

$$\sigma_{ij} = C_{ijkl}\epsilon_{kl} \qquad i, j, k, l = 1, 2, 3., \tag{2.4}$$

where C_{ijkl} are the elastic stiffness or elastic constants (with units of force per unit area) and depend on the type of material [28]. This elastic moduli define the material's resistance to elastic deformation and it is a fourth rank tensor with $3^4 = 81$ components [29]. Equation 2.3 is sometimes referred to as Hooke's law [26], [29]. Since both the stress and strain tensors are symmetric (that is, $\sigma_{ij} = \sigma_{ji}$ and $\epsilon_{ij} = \epsilon_{ji}$), the above equation demands C_{ijkl} to be symmetric as well [29]. Also, the elastic constant tensor is invariant under the transpositions $i \leftrightarrow j$ or $k \leftrightarrow l$ [15] such that $C_{ijkl} = C_{jikl}$ and $C_{ijkl} = C_{jilk}$ [25], [28]. This reduces the the number of independent components to 36. This is because, from definition of an elastic material [28], the strain energy density is a function of strain ($U_0 = U_0(\epsilon_{ij})$) such that its second derivative is given by

$$\frac{\partial^2 U_0}{\partial \epsilon_{ij} \partial \epsilon_{kl}} = C_{klij} \tag{2.5}$$

$$\frac{\partial^2 U_0}{\partial \epsilon_{kl} \partial \epsilon_{ij}} = C_{ijkl} \tag{2.6}$$

Thus one can conclude that the order is not important, implying that the elastic constant tensor must be symmetric, that is, $C_{ijkl} = C_{jikl} = C_{jilk}$. Therefore, the following notation (known as the Voigt contracted notation [26], [29]) will be adopted for simplicity; $ij \leftrightarrow \alpha$ and $kl \leftrightarrow \beta$ such that $c_{ijkl} = c_{\alpha\beta}$. Thus Equation (2.4) becomes

$$\sigma_\alpha = C_{\alpha\beta}\epsilon_\beta \qquad (\alpha, \beta = 1, 2, \ldots 6) \tag{2.7}$$

This notation results in a 6×6 matrix with the number of components reduced to 21 (notice that the matrix is symmetric about the diagonal components)

such that

$$\begin{pmatrix}\sigma_1\\ \sigma_2\\ \sigma_3\\ \sigma_4\\ \sigma_5\\ \sigma_6\end{pmatrix} = \begin{pmatrix}C_{11} & C_{12} & C_{13} & C_{14} & C_{15} & C_{16}\\ C_{21} & C_{22} & C_{23} & C_{24} & C_{25} & C_{26}\\ C_{31} & C_{32} & C_{33} & C_{34} & C_{35} & C_{36}\\ C_{41} & C_{42} & C_{43} & C_{44} & C_{45} & C_{46}\\ C_{51} & C_{52} & C_{53} & C_{54} & C_{55} & C_{56}\\ C_{61} & C_{62} & C_{63} & C_{64} & C_{65} & C_{66}\end{pmatrix} \begin{pmatrix}\epsilon_1\\ \epsilon_2\\ \epsilon_3\\ 2\epsilon_4\\ 2\epsilon_5\\ 2\epsilon_6\end{pmatrix} \tag{2.8}$$

This is representative of a triclinic crystal system whose elastic properties depend on the direction of propagation of elastic waves; known as a triclinic material. Depending on the plane or axis of crystal symmetry, these elements can be reduced even further [28]. For instance, a material with only one plane of symmetry referred to as a monoclinic crystal system (hence mono for "one plane"), the number of components is only 13 as shown below:

$$\begin{pmatrix}\sigma_1\\ \sigma_2\\ \sigma_3\\ \sigma_4\\ \sigma_5\\ \sigma_6\end{pmatrix} = \begin{pmatrix}C_{11} & C_{12} & C_{13} & C_{14} & 0 & 0\\ C_{12} & C_{22} & C_{23} & C_{24} & 0 & 0\\ C_{13} & C_{23} & C_{33} & C_{34} & 0 & 0\\ C_{14} & C_{24} & C_{34} & C_{44} & 0 & 0\\ 0 & 0 & 0 & 0 & C_{55} & C_{56}\\ 0 & 0 & 0 & 0 & C_{56} & C_{66}\end{pmatrix} \begin{pmatrix}\epsilon_1\\ \epsilon_2\\ \epsilon_3\\ 2\epsilon_4\\ 2\epsilon_5\\ 2\epsilon_6\end{pmatrix} \tag{2.9}$$

When there are two and/or three planes of symmetry, the above equation results in 9 components. For such a material, two of the three planes of symmetry are mutually orthogonal to one another; this system is orthorhombic. Proceeding in this manner, one can show that introducing one, two and three axes of symmetry in addition to the planes, the elastic constants can be reduced even further [28]. For instance, a material with three axes of symmetry and three planes, is or has a cubic crystal system. By solving the stress-strain equation for several scenarios (refer to Kundu (2003) for a derivation [28]), one can reach several constraints that must be satisfied: $C_{11} = C_{22} = C_{33}$, $C_{12} = C_{13}$ and $C_{44} = C_{55} = C_{66}$. This results in only 3 independent elastic constants, C_{11}, C_{12} and C_{44} respectively, that is:

$$\begin{pmatrix}\sigma_1\\ \sigma_2\\ \sigma_3\\ \sigma_4\\ \sigma_5\\ \sigma_6\end{pmatrix} = \begin{pmatrix}C_{11} & C_{12} & C_{12} & 0 & 0 & 0\\ C_{12} & C_{11} & C_{12} & 0 & 0 & 0\\ C_{12} & C_{12} & C_{11} & 0 & 0 & 0\\ 0 & 0 & 0 & C_{44} & 0 & 0\\ 0 & 0 & 0 & 0 & C_{44} & 0\\ 0 & 0 & 0 & 0 & 0 & C_{44}\end{pmatrix} \begin{pmatrix}\epsilon_1\\ \epsilon_2\\ \epsilon_3\\ 2\epsilon_4\\ 2\epsilon_5\\ 2\epsilon_6\end{pmatrix} \tag{2.10}$$

Due to isotropic deformation of one of the planes of symmetry, the third elastic constant can be obtained from the famous Cauchy relation: $C_{12} = C_{11} - 2C_{44}$ [28], [29]. Thus materials with only two independent elastic constants are known as isotropic solids. Amorphous and polycrystalline materials are examples of such materials. From Hooke's law, one can say the principle axes of the stress are equivalent to those of the strain [25]. Summarised in table 2.1

are the number of independent elastic constants for the seven crystal systems and their corresponding point groups as given in Ref.[15].

Crystal System	Point Groups	Number of Elastic constants
Triclinic	all	21
Monoclinic	all	13
Orthorhombic	all	9
Tetragonal	C_4, C_{4h}, S_4	7
	C_{4v}, D_4, D_{4h}, D_{2d}	6
Rhombohedral	C_3, S_6	7
	C_{3v}, D_3, D_{3d}	6
Hexagonal	all	5
Cubic	all	3

Table 2.1: Number of independent elastic constants in seven crystal systems. Adapted from Ref.[15].

Equation 2.10 can be expressed in terms of Lamé's constants, μ and λ such that; $\mu = C_{44}$, $\lambda = C_{12}$ and $\lambda + 2\mu = C_{11}$ [25], [28], [29]. In the same way, the engineering moduli for isotropic materials can be derived from the two constants such that:

$$\begin{aligned} E &= \frac{\mu(3\lambda + 2\mu)}{\lambda + \mu} \\ K &= \frac{3\lambda + 2\mu}{3} \\ \nu &= \frac{\lambda}{2(\lambda + \mu)} \\ G &= \mu, \end{aligned} \tag{2.11}$$

where E and K are the Young and Bulk moduli, ν is the Poisson ratio and G is the shear modulus. The Bulk modulus is the material's resistance to volumetric deformation due to hydrostatic pressure. The Young's Modulus is a measure of the stiffness, whilst the shear modulus decribes the material's resistance to reversible plastic deformation upon shear stress. Lastly, the Poisson's ratio is the ratio of the transverse compression to the longitudinal extension [25], [30]. The engineering moduli equations for anisotropic materials are not discussed here, since the materials investigated in this study, are amorphous and polycrystalline films and hence are isotropic materials.

2.2 Bulk and Surface Acoustic Waves

A knowledge of any two of the elastic constants or engineering moduli (Equation 2.11) is sufficient to describe the elastic properties of isotropic materials.

Often, the propagation of surface acoustic waves (SAWs) in materials is used to derive these properties. There are several methods that are widely employed in probing near surface elastic properties of thin supported films or solids by coupling SAWs. These are, acoustic microscopy (AM), laser-generated surface acoustic waves (LSAW) and surface Brillouin scattering (SBS) [31]. The latter is the main characterization technique chosen for this work, simply because it is a direct non-contact method of probing thermally excited acoustic waves. Details of the principles of this technique will be provided in the next two sections of this chapter.

There are two types of acoustic waves, namely bulk acoustic waves and surface acoustic waves, respectively. Bulk acoustic waves propagating in an infinite elastic solid are the P-wave (P for primary) and the S-wave (S for secondary), respectively. P-waves are generated when a material is subjected to normal compressional or longitudinal stress. S-waves propagate in a material if the applied stress is parallel to the free surface and generates shear stress only. This wave is sometimes called the shear wave. Generally, the P-wave and the S-wave are known as longitudinal and transverse acoustic waves respectively [28]. A wave is referred to as a longitudinal or transverse wave if their polarization vector is parallel or perpendicular to the propagation vector [6]. However, this is determined by the symmetry of the propagation direction (more details on the acoustic wave propagation are presented in the next section). When bulk waves encounter an interface or a stress-free surface of a semi infinite isotropic medium, they undergo reflection and transmission, resulting in surface acoustic waves [28].

Surface acoustic waves are characterized by evanescent acoustic displacement fields that decay exponentially below the surface of a layer, that is inside the bulk of the medium. One such wave is the Rayleigh surface acoustic wave (RSAW); this is a true surface wave with its displacement field and energy confined near the surface of a layer [6], [32]. Higher frequency surface modes are known as Sezawa waves (SW). These are SAWs whose particle displacements are localized in the layer and decay exponentially in the substrate supporting the layer. These kinds of surface waves are observed for a system comprising of an opaque layer supported by a substrate [33].

The contrast between the elastic properties of the layer and those of the substrate also determines the propagation of SWs. Therefore, these waves are observed when the velocity of the bulk transverse wave propagating in the layer, is smaller than that of the substrate, that is, $v_t^l \leq v_t^s$ [33]. This depends on the material mass density ρ, and the product of the wave vector of the phonon propagating parallel to the surface $k_{//}$, and layer thickness d. For larger $k_{//}d$, more Sezawa waves are observable and even pseudo-Sezawa waves appear as sharp resonances at higher frequency shifts in the supersonic region [32]. These waves have larger amplitudes and can couple to bulk acoustic waves. Other waves that can be observed depending on a number of factors, are the Stoneley interfacial waves, Love waves and Lamb waves [32], [31].

The Stoneley wave is one whose displacements decay with distance from the interface in both directions. It occurs when $v_t^l \approx v_t^s$ [6].

2.3 Acoustic Wave Propagation

We will consider the displacement field that must satisfy the wave equation for a homogeneous elastic medium

$$\rho \frac{\partial^2 u_i}{\partial t^2} = C_{ijkl} \frac{\partial^2 u_l}{\partial x_j \partial x_k}, \tag{2.12}$$

where ρ is the mass density of the material and u_i are the particle displacement components which are the solutions to the above equation and are given by [6]:

$$u_i = U_i \exp\left[i(\vec{k} \cdot \vec{x} - vt)\right] = U_i \exp\left[ik(l_1 x_1 + l_2 x_2 + l_3 x_3 - vt)\right], \tag{2.13}$$

where U_i are the polarization vectors of the plane waves and (l_1, l_2, l_3) are the direction cosines of the wavevector $\vec{k}$ in the (x_1, x_2, x_3) directions of the coordinate system as shown in Figure 2.1. For a surface acoustic wave, the amplitudes of all the displacement components vanish as $x_3 \longrightarrow \infty$. Therefore, the x_3 component becomes part of the amplitude and the SAW propagates parallel to the surface in the plane $\mathbf{x}_{//} = (x_1, x_2)$ with wavevector $\mathbf{k}_{//} = (k_1, k_2)$ [6], [26]. Equation 2.13 is thus regarded as a linear combination of the plane waves in the form:

$$u_i = \sum_{n=1}^{3} D_n U_i^{(n)} \exp(ikl_3^{(n)} x_3) \exp\left(i\mathbf{k}_{//} \cdot \mathbf{x}_{//} - vt\right), \tag{2.14}$$

where D_n are the weighting factors and depend on C_{ijkl} and ρ [32]. The polarisation vector can be obtained from the secular equation:

$$(\Gamma_{ij} - \delta_{ij}\rho v^2)U_i = 0 \tag{2.15}$$

The components $l_3^{(n)}$ are the three complex roots of the Christoffel equation given by

$$|\Gamma_{ij} - \delta_{ij}\rho v^2| = 0, \tag{2.16}$$

where δ_{ij} is the Kronecker delta function and Γ_{ij} is the second rank Christoffel tensor given by $\Gamma_{ij} = C_{ijkl} l_k l_l$.

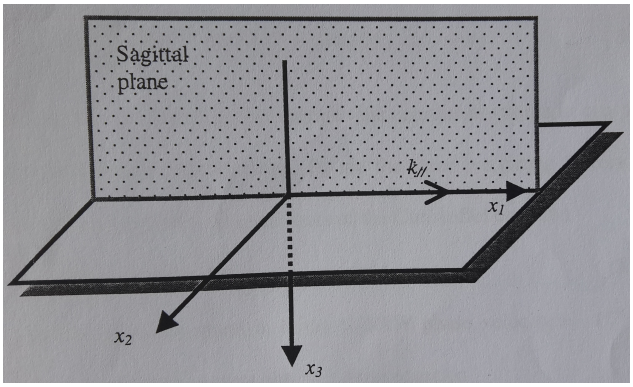

Figure 2.1: The co-ordinate system for surface acoustic wave propagation. The sagittal plane is a plane that contains the propagation vector $k_{//}$ and is normal to the free surface [6].

It can be shown that by substituting the solutions into the above equation, non-trivial solutions are obtained such that the determinant of the boundary condition matrix, $\mathbf{B}$, vanishes [32], that is:

$$det|\mathbf{B}| = 0 \tag{2.17}$$

For a surface wave such as the Rayleigh SAW propagating in an isotropic half-space, solving the above equation analytically yields the velocity of the RSAW via the famous Rayleigh equation [28] in terms of the elastic constants:

$$\xi^2 C_{44}(C_{11} - \xi) - C_{11}(C_{44} - \xi)(C_{11} - C_{12}^2/C_{11} - \xi)^2 = f(\xi) = 0, \tag{2.18}$$

where $\xi = \rho v_R^2$, $C_{12} = C_{11} - 2C_{44}$ and v_R is the velocity of the RSAW, respectively. Since the RSAW can be measured directly by SBS [7]-[31] and with ξ known, one can find the lower bound of the shear or transverse velocity, v_T for positive Poisson ratios of less than 0.5 from the two equations:

$$v_R = \frac{0.87 + 1.12\nu}{1 + \nu} v_T \tag{2.19}$$

or

$$v_R = 0.919 v_T \tag{2.20}$$

For Bulk acoustic waves, following from Equation 2.22 (next page), the polarization vectors are related to the direction cosines [6] via the linear equation

$$(C_{ijkl} l_k l_l - \delta_{ij} \rho v^2) U_i = 0 \tag{2.21}$$

One needs to determine the elements of the Christoffel tensor, $\Gamma_{ij} = C_{ijkl} l_k l_l$ which leads to a cubic equation in v^2 (Equation 2.21) as given on the next page.

The evaluation of Equation 2.22 solely depends on the direction of propagation, that is, the cosines direction (l_1, l_2, l_3). For instance, for waves moving

$$\begin{vmatrix} l_1^2C_{11} + (l_2^2 + l_3^2)C_{44} - \rho v^2 & l_1l_2(C_{12} + C_{44}) & l_1l_3(C_{12} + C_{44}) \\ l_1l_2(C_{12} + C_{44}) & l_2^2C_{11} + (l_1^2 + l_3^2)C_{44} - \rho v^2 & l_2l_3(C_{12} + C_{44}) \\ l_1l_3(C_{12} + C_{44}) & l_2l_3(C_{12} + C_{44}) & l_3^2C_{11} + (l_1^2 + l_2^2)C_{44} - \rho v^2 \end{vmatrix} = 0 \tag{2.22}$$

along $l_1 = 1, l_2 = 0, l_3 = 0$, that is, the wavevector $\mathbf{k}$, propagates in the [100] direction in an infinite cubic solid or isotropic solids such equation is given by

$$\begin{vmatrix} C_{11} - \rho v^2 & 0 & 0 \\ 0 & C_{44} - \rho v^2 & 0 \\ 0 & 0 & C_{44} - \rho v^2 \end{vmatrix} = 0 \tag{2.23}$$

The solutions obtainable from the above equation gives three velocities of the bulk waves and the polarisation vectors;

$$\begin{aligned} v_L &= \sqrt{\frac{C_{11}}{\rho}}; \qquad (U_1 = 1, U_2 = 0, U_3 = 0) \\ v_T &= \sqrt{\frac{C_{44}}{\rho}}; \qquad (U_1 = 0, U_2 = 1, U_3 = 0) \\ v_T &= \sqrt{\frac{C_{44}}{\rho}}; \qquad (U_1 = 0, U_2 = 0, U_3 = 1) \end{aligned} \tag{2.24}$$

The bulk longitudinal velocity depends on the elastic constant C_{11}, while the fast and slow transverse velocities depend on C_{44} only. Thus for isotropic materials, the two transverse waves are degenerate and their velocities (as well as the longitudinal wave velocity) [6] in any propagation direction, are given by the three relations in Equation 2.24. These relations indicate that the elastic constants can be obtained by measuring the velocities of the acoustic waves. In general, the velocity relations are determined by the propagation direction of the acoustic waves. Hence they are different for different systems. For instance, when propagation is along the [110] and [111], the velocity relations adopt a dependence on the elastic constant C_{12} [6].

2.4 Theory of Surface Brillouin Scattering

The inelastic scattering of light by thermally excited elastic waves propagating in a solid is known as Brillouin light scattering (BLS). When this occurs on the surface of a material, it is referred to as surface Brillouin scattering (SBS). The first theoretical study of light scattering due to thermal phonons was carried out by Mandelstam in 1918. However, Brillouin also predicted this phenomenon individually and later, Gross (1930) presented evidence by performing experiments in liquids and crystals [6], [26], [7], [34]. Nowadays, SBS has emerged as the only technique that can directly detect SAWs in the frequency region of $2 - 30$ GHz. Thus it can be used to study near-surface elastic properties of materials.

In this section, Brillouin scattering will be described as bulk or surface depending on the type of SAWs propagating in the material either as bulk or surface phonons. As such, there are two scattering mechanisms that govern

BLS, depending on the optical transparency of the medium in question; these are the bulk opto-elastic and surface ripple scattering mechanisms respectively. The former occurs in optically transparent materials and is due to light scattering by bulk acoustic waves. The latter, occurs in semi-opaque and opaque supported thin films or layers and hence is due to phonons propagating near the surface. These mechanisms can be understood when BLS is viewed as the transfer of momentum and energy between photons of incident light and the phonon field through either the bulk and / or the surface scattering.

2.4.1 Kinematics of Brillouin Scattering

Consider an incident photon with wavevector $\vec{k_i}$ and frequency ω_i that is inelastically scattered by a thermally induced elastic wave or acoustic phonon with a wavevector $\vec{K}$ and frequency $\omega(\vec{K})$. In this case, the phonons can inelastically scatter the photon in two ways; by Stokes or anti-Stokes scattering. Stokes scattering generates a phonon whereas in anti-Stokes scattering the annihilation of an acoustic phonon occurs [6], [26]. The law of conservation of total momentum and energy is obeyed during the scattering event due to bulk phonons and is governed by the following relations:

$$\begin{aligned} \mathbf{k}_s - \mathbf{k}_i &= \pm\mathbf{K} \\ \omega_s - \omega_i &= \pm\omega(\mathbf{K}), \end{aligned} \tag{2.25}$$

where $\mathbf{k_s}$ and ω_s is the wavevector and frequency of the scattered photon. In Equations 2.25, the plus and minus signs correspond to the anti-Stokes and Stokes scattering respectively. Compared to Raman Scattering, the phonon frequencies probed (and hence the velocities) are smaller compared to those of the photon by a factor of 10^{-5} [32]. As a result, the absorbed or created energy is very small and therefore the following assumption holds for scattering by bulk phonons; $\omega_s \approx \omega_i$ and $|\mathbf{k}_s| \approx |\mathbf{k}_i|$ [6]. Therefore taking this assumption into account, the magnitude of the phonon wavevector is given by

$$|\mathbf{K}| = 2|\mathbf{k}_i| \sin\varphi/2, \tag{2.26}$$

where φ is the scattering angle. Since the phonons involved in Brillouin scattering are acoustic phonons, their dispersion relation takes a linear form

$$\omega(\mathbf{K}) = v|\mathbf{K}|, \tag{2.27}$$

where v is the phase velocity of the bulk acoustic wave. Combining Equations $2.25 - 2.27$ one obtains frequency shifts $(\omega_s - \omega_i)$ that can be probed by BLS [6]; these are related to the acoustic phonon phase velocity by;

$$\omega_s - \omega_i = 2v|\mathbf{k}_i| \sin\varphi/2 \tag{2.28}$$

In most BLS experiments, the backscattering geometry is usually employed; here $\varphi = 180°$; this is shown in Figure 2.2 below.

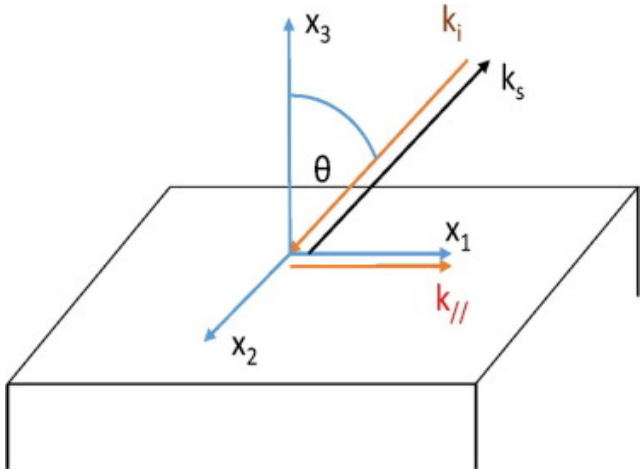

Figure 2.2: Backscattering geometry employed in SBS experiments. [7]

2.4.2 Bulk Elasto-Optic Scattering Mechanism

Bulk scattering usually occurs in a transparent medium with a refractive index n. Therefore Equations 2.26 and 2.28 are transformed to

$$\begin{aligned} |\mathbf{K}| &= 2n|\mathbf{k_i}| \\ \omega_s - \omega_i &= 2nv|\mathbf{k_i}| \end{aligned} \tag{2.29}$$

Thus bulk phonons that satisfy the above equation in the elasto-optic scattering process result in discreet phonon peaks in a typical SBS spectrum [6]. Usually, this scattering mechanism arises from bulk longitudinal and transverse waves whose velocities can be calculated from the frequency shifts [32]. According to Beghi *et al.* (2003), in this mechanism, the dynamic fluctuation in the elastic strain field, $\epsilon_{\alpha\beta}$, induce small fluctuation in the dielectric constant [32], which in turn further translate in the refractive index such that [6]:

$$\delta\epsilon_{\alpha\beta}(\mathbf{r},t) = \sum_{\gamma\lambda} k_{\alpha\beta\gamma\lambda} u_{\gamma\lambda}(\mathbf{r},t), \tag{2.30}$$

where the phonon displacements are given by

$$u_{\gamma\lambda}(\mathbf{r},t) = \frac{\partial u_\gamma(\mathbf{r},t)}{\partial x_\lambda} \tag{2.31}$$

In Equation 2.30, $k_{\alpha\beta\gamma\lambda}$ are the photoelastic constants and are related to the Pockels' elasto-optic constants [34]. It is due to the coupling between the elasto-optic constants and the dielectric constants of the acoustic phonons, that this bulk scattering process gives rise to the term elasto-optic scattering mechanism [6].

2.4.3 Surface Ripple Scattering mechanism

For opaque and semi-opaque material, the penetration of incident laser light is limited to small depths within the material. Thus, it does not penetrate through the entire volume or bulk of the medium due to the high optical absorption. The inelastic scattering process is therefore confined near the surface of the medium [32]. The dominant mechanism is mediated by dynamic rippling of the surface derived from thermal fluctuations in waves propagating near the surface, that is, SAWs. Herein, the particle displacement components perpendicular to the surface result in a dynamic corrugation of the surface. Hence the surface can be seen to act as a moving diffraction grating [6], [7]. Therefore the frequency of the incident light diffracted on the surface is modulated through the Doppler effect.

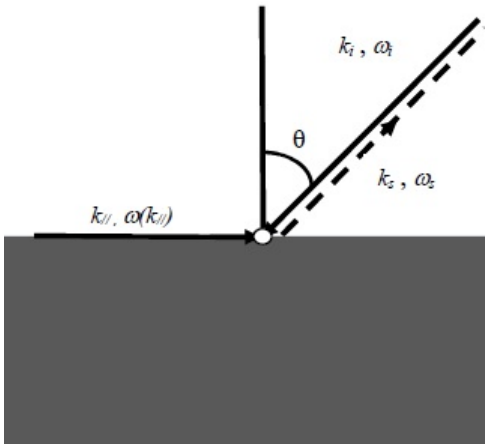

Figure 2.3: Ripple scattering mechanism by surface phonons in backscattering configuration. Adapted from Ref.[6]

One should note that for this mechanism, scattering is not limited to surface phonons only but scattering is possible by bulk phonons as well [6]. However, momentum is only conserved for those wavevector components parallel to the surface (see Figure 2.3 above). In backscattering geometry, this is given by

$$|\mathbf{k}_{//}| = 2|\mathbf{k}_i| \sin\theta, \tag{2.32}$$

where θ is the incident angle of the photon emitted from the laser and the wavevector has two components, that is, $\mathbf{k}_{//} = (k_1, k_2)$ such that its magnitude is given by the modulus of the component $\mathbf{k}_s - \mathbf{k}_i$. Here the assumption that $|\mathbf{k}_s| \approx |\mathbf{k}_i|$ still holds [7]. The change in frequency of the inelastically scattered light is related to the phonon phase velocity by a combination of the above equation with the conservation of the total energy:

$$\omega_s - \omega_i = 2|\mathbf{k}_i| v \sin\theta \quad \text{or} \quad v = \frac{\Delta f \lambda}{2 \sin\theta}, \tag{2.33}$$

where Δf is the frequency shift of the scattered photons. The above equation gives the constraints that must be satisfied by the scattering of various SAWs. Since the frequency shifts are discreet, a typical SBS spectrum of an opaque material is dominated by a sharp peak due to scattering by the RSAW and higher frequency peaks due to Sezawa waves. It must be noted that bulk waves closer to the surface can scatter the incident light by this mechanism [6], [7] (see Figure 2.4).

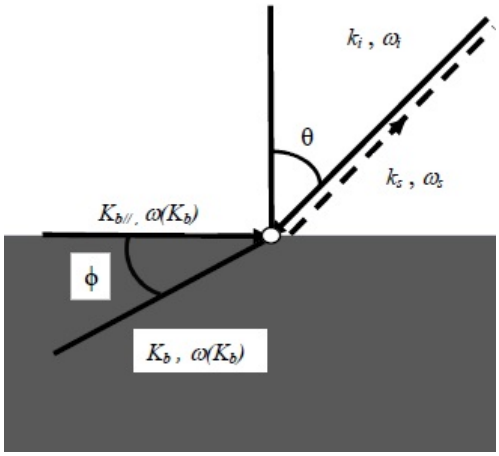

Figure 2.4: Surface scattering by bulk phonons in backscattering configuration. Adapted from Ref.[6]

Surface scattering by bulk phonons is possible if and only if the scattering occurs in the sagittal plane; this plane is orthogonal to the surface and contains the wavevector of the acoustic wave propagating parallel to the surface. By conservation of momentum components parallel to the surface:

$$2|\mathbf{k}_i| \sin\theta = |\mathbf{K}_{b//}| = |\mathbf{K}_b| \cos\phi, \tag{2.34}$$

where ϕ is the angle between the surface and the bulk wavevector, $|\mathbf{K}_b|$. The Brillouin frequency shifts are related to the bulk wave velocities by the expression [6]:

$$\omega_s - \omega_i = 2\nu|\mathbf{k}_i| \sin\theta / \cos\phi \tag{2.35}$$

Thus Equations $2.34 - 2.35$ give the conditions for inelastic scattering of light by bulk phonons near the surface. Again, since the frequency shifts are discreet, the SBS spectrum contains broad peaks associated with scattering from bulk waves. However, the scattering by SAWs is much more prominent than bulk waves near the surface [6]. In general, the ripple scattering mechanism depends on the reflectivity (and opacity) of the material since the scattered Brillouin intensity is directly proportional to this optical property [6]. In formal terms, this intensity is proportional to the power spectrum of the displacement components normal to the surface of the material. This can be shown by following the formulation by Subbaswamy and Marandudin (1978) and Loudon and Sandercock (1980) (cited in Refs. [6], [32]), which is presented in the next section.

2.5 Green's Function for the Free Surface of a Semi-infinite Supported Layer

The formulation presented in this section follows the surface Green's function approach as in [33]. Revisiting the Surface Ripple Scattering mechanism, it can be shown from the fluctuation dissipation theorem that the power spectrum (Brillouin intensity) of the normal displacement of the surface is directly proportional to the surface Green's function:

$$I(\omega) = \langle |u_3(k_{//}, x_3 = -d; \omega)|^2 \rangle \propto \frac{k_B T}{\pi \omega} \mathrm{Im}\{G_{33}(k_{//}, x_3 = -d; \omega)\}, \qquad (2.36)$$

where $\hbar$ is Planck's constant, and k_B is Boltzmann's constant. $G_{33}(k_{//}, x_3 = -d; \omega)$ is the dissipative (x_3, x_3) component of the Fourier$(\mathbf{k}, \omega)$ domain surface Green's function tensor $G_{ij}(\mathbf{x}, t)$ for the normal displacement and a harmonic time dependence force, $\vec{F}(\mathbf{x}, t)$ acting on the surface of the layer [33], [6], [32]. This takes into account that the temperature, T, must be sufficiently high, that is, $T \gg \hbar\omega/k_B$. The Green's function tensor is defined by the integral:

$$G_{ij}(\mathbf{k}_{//}, x_3, \omega) = \int_{-\infty}^{+\infty} \mathrm{d}^2\mathbf{x}_{//} g_{ij}(\mathbf{x}, x_3, \omega) \exp\{-i\mathbf{k}_{//}\mathbf{x}_{//}\}, \qquad (2.37)$$

where $\mathbf{k}_{//} = (k_1, k_2)$ and $\mathbf{x}_{//} = (x_1, x_2)$. To derive the relation given by Equation 2.36, one needs to consider a system of an anisotropic opaque layer bonded onto a substrate. Here the layer of thickness d, occupies the region $(-d < x_3 < 0)$, and the substrate occupies a half-space $x_3 > 0$. This is shown in Figure 2.5 below.

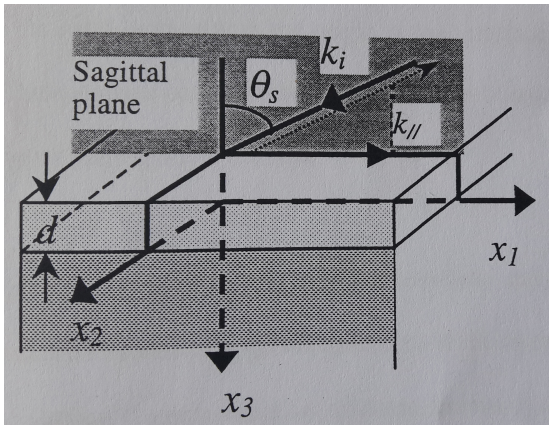

Figure 2.5: The co-ordinate system and the scattering geometry with the sagittal plane perpendicular to the surface layer with thickness d supported by a substrate occupying a half-space $x_3 > 0$. [6]

The boundary conditions that must be satisfied are:

$$\sigma_{l3}(k_{//}, x_3 = 0, \omega), \quad \text{for} \quad l = 1, 2, 3; \quad \mathbf{u}(\mathbf{x}, t); \quad \sigma_{l3}(k_{//}, x_3 = -d, \omega) = -\delta_{l3} \qquad (2.38)$$

These constraints are the continuity of stress components and displacement field at the interface of the layer and the substrate; the third relation in Equation (2.38) shows the response (indicated by the negative sign) of the stress components to the applied force at the free surface. Here δ_{l3} is the two dimensional delta function. The displacement field solutions in the layer region $(-d < x_3 < 0)$ that must satisfy the above constraints, are in form of a superposition of six incoming plane waves in the layer;

$$u_i^-(k_{//}, x_3, \omega) = \sum_{n=1}^{6} A_3^{(n)} U_i^{(n)} \exp\{ik_3^{(n)} x_3\} \tag{2.39}$$

and three outgoing plane waves in the substrate ;

$$u_i^+(k_{//}, x_3, \omega) = \sum_{n=7}^{9} A_3^{(n)} U_i^{(n)} \exp\{ik_3^{(n)} x_3\} \tag{2.40}$$

The displacement field must satisfy the wave Equation (2.12) for the layer as well as the substrate. Equation 2.12 must take six plane-wave solutions for each value of ω and $k_{//}$. The third component of the wavevector k_3, can be obtained from the secular equation (2.15) as roots given by $k_3^{(n)} \quad (n = 1.2, \ldots 6)$ for the layer. For the substrate, the roots are real if the three outgoing plane-waves $(k_3^{(n)} \quad (n = 7, 8, 9))$ are propagating into the bulk of the substrate (i.e. are bulk waves) with group velocity $\mathbf{v} = \partial\omega/\partial\mathbf{k}$. Complex or imaginary roots are obtained if the three waves are evanescent waves decaying into the bulk of the substrate [33], [6]. It follows from Equation 2.39 and the stress-strain relation, $\sigma_{lm} = C_{lmpq} \dfrac{\partial u_p}{\partial x_q}$ that the stress components at the surface of the layer are given by

$$\sigma_{l3}(k_{//}, x_3 = -d, \omega) = i\omega \sum_{n=1}^{6} A_3^{(n)} B_l^{(n)}, \tag{2.41}$$

where the boundary matrix $B_l^{(n)}$;

$$B_l^{(n)} = \sum_{pq} C_{3lpq}^- U_p^{(n)} k_q^{(n)} \exp\{-ik_3^{(n)} d\}/\omega \qquad n = 1, 2, \ldots 6; \quad l = 1, 2, 3 \tag{2.42}$$

with

$$B_l^{(n)} = 0 \quad n = 7, 8, 9; l = 1, 2, 3$$

In the above equation, the negative superscript sign of C_{3lpq}^- shows that the elastic component is being calculated in the layer (a positive superscript applies for the substrate) [32]. Comparing the last relation in Equation 2.38 with Equation 2.41 yields the first set of three linear equations for the partial wave amplitudes $A_3^{(n)}$

$$\sum_{n=1}^{6} B_l^{(n)} A_3^{(n)} = \frac{i}{\omega} \delta_{l3} \qquad l = 1, 2, 3 \tag{2.43}$$

The continuity of the stress at the interface of the layer and the substrate

$$\sigma^{+}_{j3}(k_{//}, x_3 = 0_+, \omega) = \sigma^{-}_{j3}(k_{//}, x_3 = 0_-, \omega) \tag{2.44}$$

gives the second set of equations for the partial wave amplitude

$$\sum_{n=1}^{6} B^{(n)}_l A^{(n)}_3 = 0 \qquad l = 4, 5, 6 \tag{2.45}$$

where

$$B^{(n)}_l = \sum_{pq} C^{+}_{3(l-3)pq} U^{(n)}_p k^{(n)}_q / \omega \qquad n = 7, 8, 9; \quad l = 4, 5, 6 \tag{2.46}$$

and

$$B^{(n)}_l = -\sum_{pq} C^{+}_{3(l-3)pq} U^{(n)}_p k^{(n)}_q / \omega \qquad n = 1, 2, \ldots, 6; \quad l = 4, 5, 6 \tag{2.47}$$

The continuity of the displacement field at the boundary

$$u^{+}_i(k_{//}, x_3 = 0_+, \omega) = u^{-}_i(k_{//}, x_3 = 0_-, \omega) \tag{2.48}$$

gives the last set of three equations for the partial plane waves

$$\sum_{n=1}^{6} B^{(n)}_l A^{(n)}_j = 0 \qquad l = 7, 8, 9 \tag{2.49}$$

where

$$B^{(n)}_l = U^{(n)}_{l-6} \qquad l = 7, 8, 9; \quad n = 7, 8, 9 \tag{2.50}$$

and

$$B^{(n)}_l = -U^{(n)}_{l-6} \qquad l = 7, 8, 9; \quad n = 1, 2, \ldots, 6 \tag{2.51}$$

Combining Equations 2.43, 2.45 and 2.49 gives the solution of the nine equations outlined previously

$$A^{(n)}_3 = \frac{i}{\omega} (B^{-1})^{(n)}_3 \qquad j = 1, 2, 3, \tag{2.52}$$

where B^{-1} is the inverse of the boundary condition matrix and it was introduced in Section 2.3 via Equation 2.17, which gives the condition upon which a true surface wave will propagate on the layer and hence will be observable in the SBS spectrum. Substituting the solution, Equation 2.52, into Equation 2.39 gives the displacement Green's function at the surface of the layer

$$G_{33}(k_{//}, x_3 = -d_-; \omega) = \sum_{n=1}^{6} \frac{i}{\omega} (B^{-1})^{(n)}_3 U^{(n)}_3 \exp\{-i k^{(n)}_3 d\} \tag{2.53}$$

and for the interface [32]

$$G_{33}(k_{//}, x_3 = 0; \omega) = \sum_{n=1}^{6} \frac{i}{\omega} (B^{-1})^{(n)}_3 U^{(n)}_3 \tag{2.54}$$

It follows from this Equation (2.53) that the scattered Brillouin intensity is given by

$$I(\omega) \propto \mathrm{Im}\{G_{33}(k_{//}, x_3 = -d_-; \omega)\} \tag{2.55}$$

with the corresponding scattering cross section defined as

$$\frac{\mathrm{d}^2\sigma}{\mathrm{d}\Omega \mathrm{d}\omega} = \frac{AT}{\omega}\mathrm{Im}\{G_{33}(k_{//}, x_3 = -d_-; \omega)\}, \tag{2.56}$$

where A is a constant that depends on a number of factors [6]:

- The scattering geometry that the user chooses upon performing a SBS experiment.
- Measured angular frequency shift (ω).
- Polarization of the incoming laser light.
- Optical properties of the material.

Equation 2.55 not only gives the desired result (that is, the Green's function for the free surface of a supported layer), but most importantly, it gives a description of the Brillouin scattering process that occurs at the free surface in terms of the power spectrum or intensity [6]. The crucial outcome is that the poles (peaks) of the Green's function correspond to a range of acoustic excitations. This will be the case provided that the determinant of the boundary condition matrix vanishes (Equation 2.17 must be satisfied) [32].

Generally, whether the determinant of the boundary condition matrix is a minimum or not, tells whether the Green's function poles are due to true or pseudo-SAWs. The SBS spectrum can be obtained by performing computer calculations for any system or a combination thereof [31], [32]. These include scattering from

- The surface of an opaque film adhered to a substrate.
- Isotropic and anisotropic solids supported by a substrate.
- Single crystals.
- The interface between two perfectly bonded solids with different optical transparency.

For the first two combinations, one can have a scenario of a slow on fast system or fast on slow system due to elastic softening or hardening. In conclusion, a combination of the optical properties and thickness of the materials (films and substrate) and the SBS scattering configuration, determines the type of acoustic excitations that can be probed experimentally.

2.6 Thermal Transport in Solids

The previous sections demonstrated that acoustic waves are essentially lattice phonons and are present in any solid material. These vibrational modes are brought about by thermal fluctuations and are essential for the understanding of the elastic properties of materials. It is known that one way of transporting thermal energy is by phonons [15], [8]. Therefore, the discussion will be incomplete if the lattice thermal conductivity is excluded. This fundamental property describes the ability of a material to conduct heat or thermal energy. But first, the specific heat will be derived. Unlike the previous sections where the classical formulation was sufficient to explain the concepts (however, note that a quantum formulation leads to similar results), a quantum formulation will be followed here.

Most formulations in the field of physics are inspired by downsides of previous discoveries that leave room for improvement for future scientists. Such a noticeable aspect is that of the quantum theory of lattice specific heat or heat capacity at constant volume. There exists two models of specific heat, namely the Einstein and Debye Models, respectively. The Einstein Model came about after it was argued that the classical law of specific heat by Dulong and Petit failed to explain the low temperature behaviour of materials. This is because the Dulong-Petit law simply shows that the specific heat is a constant, that is, $C_v = 3nk_B$, where n is the number of atoms per unit volume [15].

To correct this, Einstein considered the atoms in a lattice as identical quantum harmonic oscillators whose vibration is governed by mainly optical phonons with identical constant frequency ω_E that does not depend on the wavevector k [15], [35]. The phonon dispersion curves showing the ideal optical and acoustic phonon branches are displayed in Figure 2.6. This results in the specific heat converging to the law of Dulong and Petit at high temperatures only and decays exponentially at low temperatures due to difficulty in exciting high energy modes. Due to this failure, Debye saw a good opportunity to improve this model. His formulation is given below.

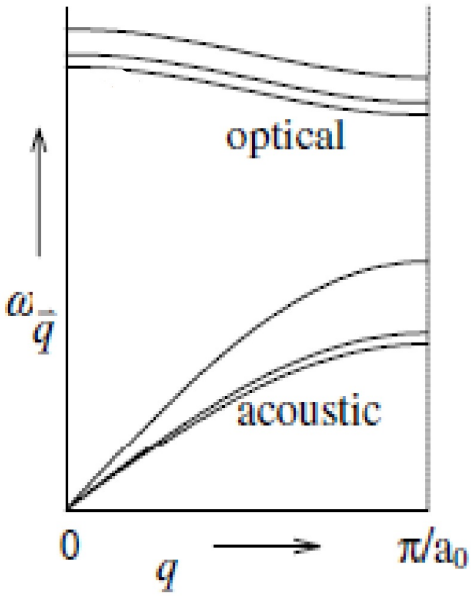

Figure 2.6: Phonon dispersion curves of a diatomic molecule showing the optical and acoustic phonon branches in the first Brillouin zone.[8]

2.6.1 The Debye Model of Specific Heat

In the Debye formulation, all phonon branches in Figure 2.6 are replaced with three acoustic phonons with a linear dispersion given by $\omega(k) = vk$, in the vicinity of the Γ point of the band structure. The wavevector k in this case is the radius of a sphere occupied by N allowed modes in the first Brillouin zone [15], [35], [8]. Then in this scheme, all allowed modes must occupy a space equal to a sphere with radius k_D such that the number of atoms per unit volume N/V (where N is equal to the number of acoustic phonon modes) are given by

$$n = \frac{k_D^3}{6\pi^2} \tag{2.57}$$

All allowed acoustic modes must have a Debye cutoff frequency of

$$\omega_D = vk_D = v\left(6\pi^2 n\right)^{1/3} \tag{2.58}$$

The specific heat is determined from the total thermal energy which is given by

$$U = \int \mathrm{d}\omega D(\omega)\left\langle n(\omega)\right\rangle \hbar\omega, \tag{2.59}$$

where $n(\omega)$ is the Bose-Einstein distribution and $D(\omega)$ is the phonon density of states given by

$$D(\omega) = \frac{Vk^2}{2\pi^2}\frac{\mathrm{d}k}{\mathrm{d}\omega} = \frac{V\omega^2}{2\pi^2 v^3} \tag{2.60}$$

Thus Equation 2.59 becomes

$$U = \int_0^{\omega_D} \left(\frac{V\omega^2}{2\pi^2 v^3} \right) \frac{\hbar\omega}{e^{\beta\hbar\omega} - 1} \mathrm{d}\omega, \tag{2.61}$$

where $\beta = 1/k_B T$. The change of variables $x = \hbar\omega/k_B T$ is adopted in order to define the Debye temperature using $x_D = \hbar\omega_D/k_B T = \Theta_D/T$;

$$\Theta_D = \frac{\hbar v}{k_B} \left(6\pi^2 n\right)^{1/3} \tag{2.62}$$

Considering this and the first statement made in this subsection, it can be shown that Equation 2.61 can be rewritten as

$$U = 9nk_B \left(\frac{T}{\Theta_D} \right)^3 \int_0^{\Theta_D/T} \mathrm{d}x \frac{x^3}{e^x - 1} \tag{2.63}$$

Then the specific heat is found by simply integrating the above expression with respect to temperature

$$C_v = 9nk_B \left(\frac{T}{\Theta_D} \right)^3 \int_0^{\Theta_D/T} \frac{x^4 e^x \mathrm{d}x}{(e^x - 1)^2} \tag{2.64}$$

Thus, unlike the Einstein Model, at temperatures below the Debye temperature, C_v shows a T^3 dependence, and therefore can be used to explain the quantum mechanical behaviour of phonons. At high temperatures, it also follows the Dulong-Petit law.

2.6.2 Lattice Thermal Conductivity

Consider a solid subjected to a slow variation in temperature. Assuming that there are no heat sinks, then this temperature gradient ∇T causes a heat current density, $\mathbf{j}^q$ that flows from a hot side to a colder end given by Fourier's law [15], [8]:

$$\mathbf{j}^q = -\kappa \nabla T, \tag{2.65}$$

or

$$\kappa = \frac{1}{3} v^2 \tau C_v, \tag{2.66}$$

where κ is the thermal conductivity, v is the average phonon velocity and $\tau = v l_{mfp}$ is the scattering rate of a phonon propagating over a mean free path, l_{mfp} [36]. Using Equations 2.64 and 2.66, the lattice thermal conductivity can be written as

$$\kappa = \frac{k_B}{2\pi^2 v} \left(\frac{k_B T}{\hbar} \right)^3 \int_0^{\Theta_D/T} \frac{x^4 e^x \mathrm{d}x}{\tau^{-1}(e^x - 1)^2} \tag{2.67}$$

This result is similar to the Callaway model (1959); however, he argues that it is not possible that the term τ^{-1} in Equation 2.67 can be due to normal phonon scattering processes only (where the crystal momentum is conserved) [37]. Therefore, other phonon scattering processes contribute to the frequency and temperature dependent relaxation times. These scattering processes are:

- Boundary scattering
- Normal three phonon scattering processes
- Impurity scattering
- Umklapp scattering

Another assumption is the neglection of the dispersion of the phonon branches in the vibrational spectrum since the material is elastically isotropic [37]. Cahill *et al.* (1992) formulated a model that can determine the lower limit of the thermal conductivity for disordered crystals [38]. This approach can be considered as a modification of Einstein's formulation through the use of Debye's model. The formulation is that the material is subdivided into $\lambda/2$ regions vibrating with a frequency $\omega = 2\pi v/\lambda$ (where λ is the phonon wavelength). It is assumed that the phonon relaxation time is given by $\tau = \pi/\omega$. The minimum lattice thermal conductivity due to thermal transport between nearest neighbour atom is then given by:

$$\kappa_{min} = \left(\frac{\pi}{6}\right)^{1/3} k_B n^{2/3} \sum_i v_i \left(\frac{T}{\Theta_i}\right)^2 \int_0^{\Theta_i/T} \frac{x^3 e^x \mathrm{d}x}{(e^x - 1)^2}, \tag{2.68}$$

where n is the atomic density or number density, Θ_i is the Debye temperature and $\sum_i v_i$ is the sum of the three sound velocities, namely the longitudinal velocity v_l and two transverse velocities v_t, respectively. Since n and v_i are known, Equation 2.68 contains no free parameters since the integral is given by a constant, and therefore, can be rewritten as

$$\kappa_{min} = \frac{1}{2}\left(\frac{\pi}{6}\right)^{1/3} k_B n^{2/3}(v_l + 2v_t) \tag{2.69}$$

This equation serves a crucial purpose for this investigation since it will be used to find the correlation between the sound velocities and κ_{min} of phase change alloys. Just to emphasize, the sound velocities will be determined from SBS studies.

Chapter 3

Experimental Methodology

This chapter gives details about experimental techniques utilized in this study. Thin films of $Ge_2Sb_2Te_5$ *and* GeTe *were deposited by radio frequency (RF) magnetron sputtering. This was followed by structural characterization by various non-destructive techniques chosen to evaluate the quality of the films. These are: Rutherford backscattering spectrometry (RBS), field emission scanning electron microscopy (FESEM) coupled with energy dispersive x-ray spectroscopy (EDS), X-ray reflectivity (XRR) and grazing incidence X-ray diffraction (GIXRD). Information about the atomic and mass densities, chemical composition, film's thickness and crystal structure was obtained. Lastly, the chapter concludes with the study of the vibrational properties, namely Raman and surface Brillouin scattering spectroscopies. These are useful tools for probing optical and acoustic phonons in materials*

3.1 Magnetron Sputtering

Sputtering remains one of the most extensively used physical vapor deposition (PVD) technique for the fabrication of thin films. It has become one of several commercialized high vacuum technologies that is central in semiconductor processing. It complements other PVD techniques such as thermal and electron beam evaporation, for the deposition of thin films and fabrication of semiconductor devices [39]. However, it must be mentioned that there are other methods for producing thin films for the microelectronic industry, with the widely used method known as chemical vapor deposition (CVD). CVD is a process whereby a thin solid layer is formed by chemically reacting gaseous reactants on a metal catalyst. There are various types of CVD and more information can be found in chapter 9 of Ref.[40]. Next, a more detailed description of sputtering is presented.

Sputtering is a process in which energetic ions are bombarded onto a solid

target material to remove the atoms from the surface. The target material can be any composition of metals, alloys, semiconductors, metal oxides etc. The ejected or sputtered atoms are then deposited onto a substrate to form or grow a film. Semiconductor wafers are widely used as substrates even though magnetic media can also be utilized. The energy required to generate discharge ions from an inert gas, is supplied electrically. Inert gases widely used to produce sputter ions include Argon, Krypton and diatomic gas molecules such as Nitrogen and Oxygen. An applied electric field is used to accelerate current-carrying electrons from the cathode to the anode, which is the target material. Thus collisions with the inert gas atoms cause this non-reactive gas to be converted into a electrically conducting gaseous medium known as a plasma [39], [40], [41].

This impact ionization process is self-sustaining, since for every Ar atom, two electrons plus an argon ion (Ar^+), are ejected and hence the plasma will glow continuously provided that the applied electric field is not quenched. This peculiar fourth state of matter (plasma), as it is known, sparked much interest in developing new plasma technologies [40]. As mentioned before, microwave plasma technology, electron beam, laser assisted and plasma enhanced CVD are among the emerging plasma technologies, in addition to the sputter deposition process. Nevertheless, various sputtering configurations make this method to be widely used in preparation of technologically important coatings in the semiconductor industry. The simplest convectional sputtering system is the diode sputtering configuration. This is basically an anode and cathode separated by a low pressure gas vacuum system. It is also known as the cathodic and or direct current (DC) sputtering. Owing to lower deposition rates and charge build-up on insulating targets, alternating current (AC) or radio frequency (RF) configurations are also available to overcome this problem [39], [40], [41].

RF sputtering is just diode sputtering but with the electrodes electrically reversed and with the power supply operated at a high frequency of 13.56 MHz. This is because at radio frequencies, the voltage can be coupled through any impedance and thus the electrical conductivity of the electrodes can be ignored, since the target self-biases to a negative potential [39]. As such, more secondary electrons are produced at lower energies and the impact ionization process becomes more self-sustaining. The advantage of RF sputtering over DC sputtering is that insulators can be sputtered, as well as metal targets, through reactive sputtering. In reactive sputtering, a reactive gas such as Oxygen (O_2), alkane gases such as methane or ethane, Nitrogen (N_2), etc., is injected together with an inert gas to facilitate the sputtering of a metal target. It is usually utilized to produce oxides, nitrides, carbides, etc. [39]. When the convectional diode sputtering system is operated in the presence of an electric field and a magnetic field, which are perpendicular to one another, but with the magnetic field parallel to the surface of the cathode, an effect known as the magnetron effect arises, and the corresponding configuration is called magnetron sputtering. This effect causes the secondary electrons to condense

much closer to the cathode, thus forming a denser plasma plume. Magnetron sputtering comes in many forms that merely depend on the shape of the magnetron, and whether it is balanced (convectional) or unbalanced, respectively [39], [40], [41]. In summary magnetron sputtering has many advantages [41] over the variants discussed earlier and that is why it is the most widely used configuration to date.

In this work, RF magnetron sputtering was the main preparative method and the details about sample preparation are given in the next section. Figure 3.1 shows the sputtering system used in this study. During operation, the deposition chamber is evacuated using the two rotary pumps to a roughing pressure of 1.0×10^{-2} mbar. Then base pressures in the order of 10^{-5} mbar is attained by using the two turbo molecular pumps. This is for obtaining a high vacuum and it is also good for removing any residual gases in the chamber. The pressure is read on the pressure gauge as in Figure 3.1. The mass flow controller is used to regulate the amount of Argon gas (and other reactive gases which were not used in this case) flowing into the chamber. As standard practice, before the plasma can be ignited by setting the desired power and bias voltage on the RF generator, the magnetron (not shown in the Figure) must be supplied with deionized water for cooling it. This is because in this configuration (magnetron sputtering), high current densities are produced even when operated with low voltages [40]. Pre-sputtering for several minutes helps in cleaning the surface of the target.

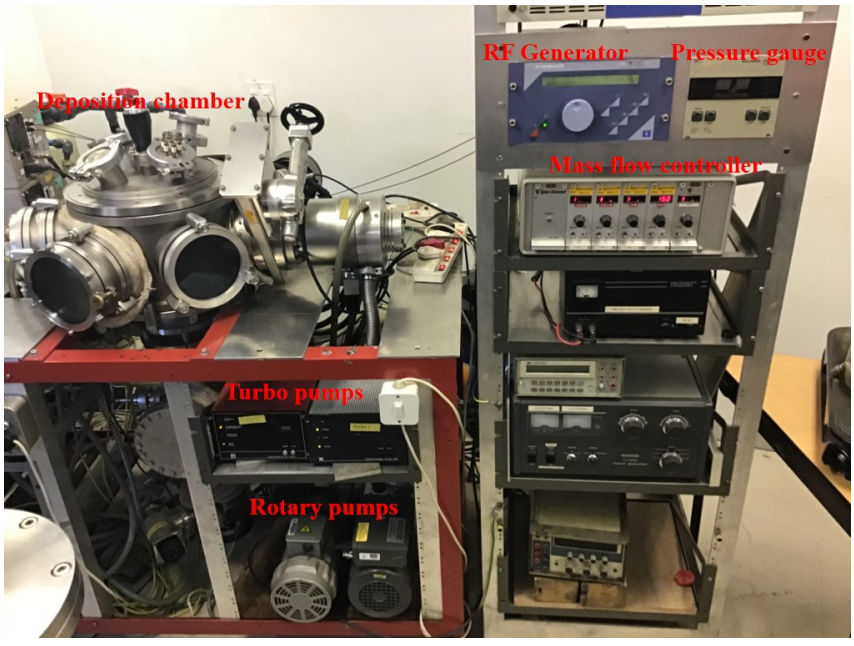

Figure 3.1: A labelled photo of the radio frequency (RF) magnetron sputtering system used to deposit films for this study.

3.1.1 Sample Preparation

Thin films of two technologically important alloys, $Ge_2Sb_2Te_5$ and GeTe, were prepared using RF magnetron sputtering. These chalcogenide alloys are narrow bandgap ($0.5 - 0.7$ eV), degenerate p-type semiconductors in their crystalline phases. There exits three structural phases of $Ge_2Sb_2Te_5$, namely amorphous, metastable cubic and hexagonal phases, respectively. The metastable cubic phase can be viewed as a NaCl type of structure with 20% vacancies, whilst the hexagonal phase is a thermodynamically stable structure of $Ge_2Sb_2Te_5$. GeTe exhibits two crystalline phases: a low temperature $\alpha-$GeTe and high temperature $\beta-$GeTe, respectively. The latter phase is a face centered cubic with a rocksalt structure. The $\alpha-$GeTe is said to be a rhombohedrally distorted form of $\beta-$GeTe. This structure is known to be ferroelectric below a critical temperature of around 700 K [42], [43].

Targets of $Ge_2Sb_2Te_5$ and GeTe, and a silicon substrate, Si (100), with 99.999% purity were purchased from Semiconductor Wafer Inc. The targets were used to fabricate identical sets of films with thickness in the range of $50 - 500$ nm, on the Si substrate; three and two sets for $Ge_2Sb_2Te_5$ and GeTe, respectively. Deposition was carried-out at room temperature with the base pressure in the range of $1.8 - 2.5 \times 10^{-5}$ mbar and a working or deposition pressure ranging from $3.7 - 4.4 \times 10^{-4}$ mbar. The deposition rate of these two materials were determined from XRR measurements. The target was self-biased at a voltage of $137 - 151$ V with the RF sputtering power kept at 20 W throughout the study. The Argon gas was flown at a fixed rate of 20 standard cubic centimeter (sccm). All sets of the as-deposited films exhibited a disordered or amorphous structure.

Crystalline phases were obtained by thermal annealing in Ar atmosphere in a Carbolite furnace. Two sets of the as-deposited $Ge_2Sb_2Te_5$ films were annealed at temperatures of 200 °C and 350 °C. This was done to probe the cubic NaCl-type ($c - Ge_2Sb_2Te_5$) and hexagonal ($h - Ge_2Sb_2Te_5$) structures, respectively. The chosen temperatures are slightly above the reported crystallization temperatures of about 189 °C and 179 °C for the two structural phases; the reason being to obtain more stabilized crystalline phase(s). For GeTe, one set of the as-deposited films were annealed at 230 °C to probe structural transition. The presence of Raman-active modes confirms that the annealed films have an $\alpha -$ GeTe structural phase, as presented in chapter 4.

3.2 Structural Characterization

3.2.1 Rutherford Back-Scattering Spectrometry

The scattering of α-particles ($^4_2$He) as observed by Rutherford in 1906 is still a great achievement not only in nuclear and particle physics, but in condensed matter physics as well. Nowadays, this phenomenon has been implemented as a technique widely known as Rutherford Backscattering Spectrometry (RBS), thanks to the development of linear accelerators in the 1930s [44]. This is used to study the chemical constituents in unknown materials. RBS is a non-destructive, direct method for studying solid surfaces and film interfaces [9].

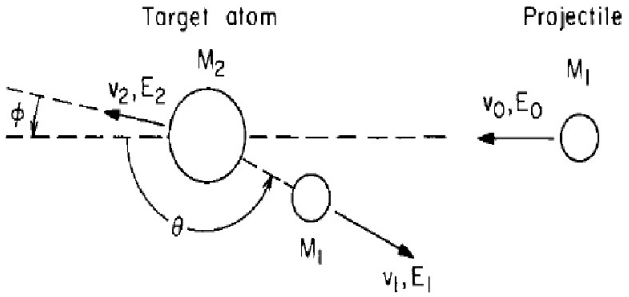

Figure 3.2: Diagram illustrating elastic collision between the target and projectile atoms. [9]

The concept of backscattering spectrometry relies on the elastic collision of two particles in the absence of nuclear reactions and resonances [9]. Consider a beam of projectile ions with mass M_1 bombarded onto a stationary solid target with mass M_2 as seen in Figure 3.2. Before collision, the incident beam has an energy E_0 in the order of MeV, and after collision, the incident beam and target have energies, E_1 and E_2, respectively. It can be shown from the principles of conservation of momentum and energy that the ratio of the energy of the projectile beam after collision E_1, to the incident beam energy, E_0 before the collision is given by

$$K = \frac{E_1}{E_0} = \left[\frac{\sqrt{M_2^2 - M_1^2 \sin^2\theta} + M_1 \cos\theta}{M_2 + M_1} \right]^2 , \tag{3.1}$$

where K is known as the kinematic factor and θ is the scattering angle. This ratio represents the energy transfer between the projectile ions and the target solid. The consequence of the above equation is that for a collision occurring at $\theta = 0°$ between projectile ions and the target solid of equal masses, yields $K = 0$ [45]. Therefore, in backscattering spectrometry, a scattering angle of 180° is usually deployed, since it results in the largest energy transfer [9], [46].

Thus Equation 3.1 for a backscattering configuration reduces to

$$K = \left[\frac{M_2 - M_1}{M_2 + M_1}\right]^2 \tag{3.2}$$

Equation 3.2 shows that K depends on the relative atomic masses of the projectile ions and the scatter only. The frequency at which the elastic collision results in ions being scattered at an angle of θ is given by the classical Rutherford scattering cross section. The concept is illustrated in Figure 3.3:

$$\frac{\mathrm{d}\sigma}{\mathrm{d}\Omega} = \left(\frac{Z_1 Z_2 e^2}{2E}\right)^2 \frac{\left[\sqrt{M_2^2 - M_1^2 \sin^2\theta} + M_2 \cos\theta\right]^2}{M_2 \sin^4\theta \sqrt{M_2^2 - M_1^2 \sin^2\theta}}, \tag{3.3}$$

where Z_1 and Z_2 are the atomic numbers of the projectile ions and the target solid, e is the electronic charge, and E is the energy of the projectile ions just before scattering. The scattering cross section does not change much with scattering angles close to 180°.

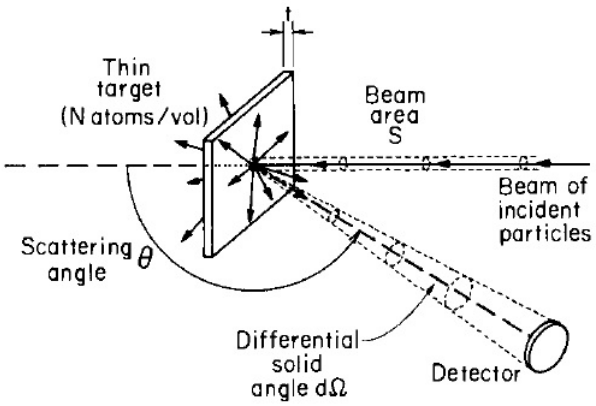

Figure 3.3: Scattering experiment illustrating the concept of Rutherford scattering cross section. [9]

Some of the obvious consequences of Equation 3.3 is that a higher yield of backscattered ions is obtained when:

- A Helium (or any of the $Z_1 = 3, 5$ ions) beam is used instead of protons [9] or electrons [46].
- Higher Z_2 target solids are analyzed since they are good scatterers and,
- A relatively low energy (< 10 MeV) of the projectile beam is used.

This probability depends on the scattering geometry employed. Two of the widely used geometries are, the IBM and Cornell geometries as shown in Figure 3.4 [10]. The IBM geometry is adopted in RBS. Here the incident beam, exit

(backscattered ions) beam and the surface normal are coplanar, such that $\alpha + \beta + \theta = 180°$. Here α is the incident angle, β is the exit angle, and θ is the scattering angle. In the Cornell geometry, the angles are related by: $\cos(\beta) = -\cos(\alpha)\cos(\theta)$ [10].

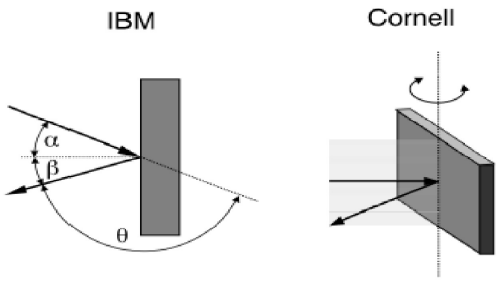

Figure 3.4: The IBM and Cornell geometries. [10]

Due to the unavailability of top-of-the-bench spectrometers, one disadvantage of this method is that it is only accessible at linear accelerator facilities. For this work, the scanning probe microscopy line of the tandem accelerator at iThemba Laboratory for Accelerator Based-Sciences (LABS) Gauteng, was used to carry-out RBS measurements. A typical setup for RBS experiments using a linear particle accelerator is shown in Figure 3.5. Thin films of $Ge_2Sb_2Te_5$ and GeTe were bombarded with 3.6 MeV energetic He^{2+} ions with a beam of current less than 1 nA and of size 100 μm $\times$ 100 μm. The samples were tilted at an angle of 5° to avoid ion channelling. Ion channelling occurs when the incident beam of ions are channelled or steered by a plane of atoms due to a series of correlated small angle collisions when they undergo forward scattering (transmission into the target solid). The consequences of this effect is that it reduces the yield of backscattered ions. However, it can be used to study lattice distortions, impurity distributions within the lattice, as well as the chemical composition and thickness of amorphous solids [9].

The backscattered ions were detected with a Si detector which is placed along the trajectory of these particles. One thing to note is that the projectile ions are not detected, since only one in 10^4 are backscattered, the rest are stopped within the target solid. A typical RBS spectrum is a plot of three parameters, namely the energy of the backscattered atoms or ions, the number of channels and the normalized backscattering yield (in counts), which is the energy per channel number. This plot, as shown in Figure 3.6, gives a distinct peak that occurs at a certain energy and channel number for a particular element (this is applicable to isotopes as well) as determined by its kinematic factor K. Thus in this way, one can identify the chemical constituents of the films. The analysis and simulation of the RBS spectrum can be performed using the simulation of nuclear reaction analysis (SIMNRA) or the XRump softwares [10]. The XRump, which is a freely available numerical simulation software, was used in this study [47].

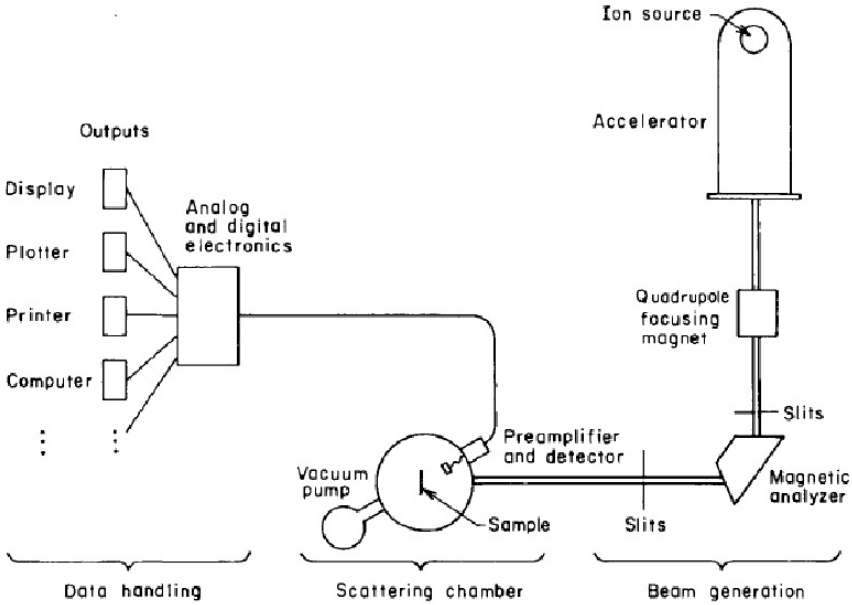

Figure 3.5: Schematic diagram of a typical RBS experiment carried out with a linear particle accelerator. [9]

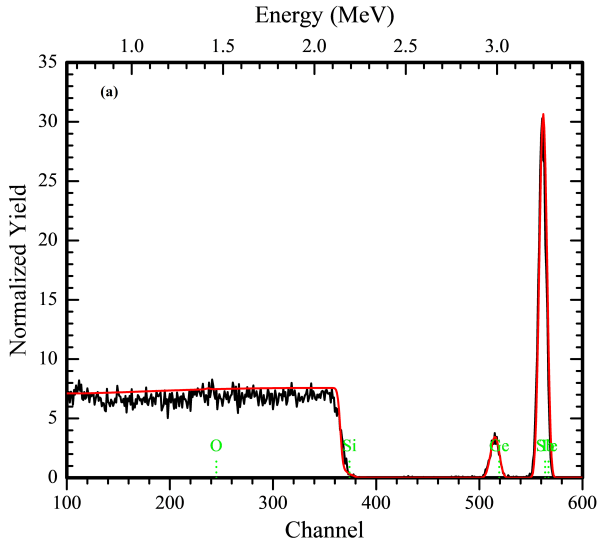

Figure 3.6: Typical RBS spectrum of as-deposited 87 nm $Ge_2Sb_2Te_5$

In general, the analysis is simple but it is a trial and error procedure where the best fit of the spectrum relies on numerical simulation of several parameters. For determination of the atomic density, n (in atoms/cm^3) of the solid target, a layered sample model is adopted in which the film thickness, t and the chemical composition (in atomic or weight percentage) can be varied. This code usually gives atomic density in units of atoms/cm^2, also known as the areal density, N. However, it also permits one to work in linear units such as angstroms and nanometers. In this case, these units can be converted into

units of atomic density, atoms/cm^3. However, the mass density, ρ, of the material must be known, and thus the atomic density is given by:

$$n = \frac{N}{t};\ n = \frac{\rho N_A}{M_r}, \tag{3.4}$$

where N_A is Avogadro's number and M_r is the molar mass of the material [9]. The film thicknesses were simulated in both units of nanometers and areal density for the sake of obtaining the atomic density. In conclusion, in addition to chemical composition and atomic density determination, RBS can be used for depth profiling and energy straggling, determining the target's stopping energies, and for studying lattice distortions and impurities [9].

3.2.2 Field Emission Scanning Electron Microscopy

In this section a brief overview of field emission scanning electron microscopy (FESEM) is given. More information can be found in the instruction manual [11]. The principle of operation is based on scanning the surface of the sample by a focused beam of electrons. These electrons are produced by a field-emission electron gun, hence the name FESEM. In conventional SEM, thermionic guns are often used. There are several interactions that can occur when the sample is bombarded with energetic electrons. These are the generation of Auger electrons, secondary and backscattered electrons, and emission of characteristic X-rays. The former interaction cannot be characterized by SEM and requires its own instrumental setup known as Auger spectroscopy (AS). The latter is used to obtain elemental maps that reveal information about the chemical composition of the sample. This technique is known as energy dispersive X-ray spectroscopy (EDS or EDX) [48].

Elemental analysis can be done in a FESEM by coupling the system with an EDS solid state detector. By scanning a chosen limited area on the sample's surface, an energy spectrum of the X-rays can be obtained and thus specific elements can be identified in atomic or weight percentages. A typical EDS spectrum is a plot of the intensity of the dispersed electrons versus characteristic X-rays energies [48]. EDS is a complementary technique to RBS for obtaining chemical compositional information quantitatively. However, there are certain disadvantages: a much smaller area confined to the surface is probed upon mapping and the detector has a poor sensitivity to low abundance elements (that is, $Z << 13$, where Z is the atomic number) and poor energy resolution [48]. This is the reason why RBS was chosen as the main technique for characterizing the chemical composition since it overcomes these challenges.

Figure 3.7 shows a typical FESEM setup, with major instrumental parts labelled [11]. During operation, the electrons emitted by the gun are accelerated with a voltage of 20 kV and directed by a set of focusing optics in the optical Gemini column (A) to the vacuum-pumped chamber (B) where

the samples are mounted. An area of $600 \times 600 \ \mu m^2$ was scanned. Then an in-lens scintillator detector mounted inside the Gemini column is used to detect the secondary electrons, whilst the backscattered electrons are collected by a backscatter detector (BSD) (D). The emitted characteristic X-rays are detected by an EDS detector (C). Another detector is available for carrying-out wavelength dispersive X-ray spectroscopy (WDX) (E) measurements but was not used in this work. The entire instrument is controlled by a SmartSEM software with the assistance of the two monitors (F) and personal computer (G) respectively. Images produced have a spatial resolution of 1.5 nm and magnification of 20000× up to 100000× was used for surface morphology details [11]. There was no need to coat the samples analyzed in this work with a conducting medium since they were deposited on a silicon substrate, which is semiconducting.

Figure 3.7: Zeiss Sigma FESEM setup. The labels were defined in the previous paragraph [11]

3.2.3 X-Ray Reflectivity and Grazing Incidence X-Ray Diffraction

The use of X-rays for qualitative and quantitative analysis of the structure of solids still proves to be the only convenient method to date. While traditional X-ray diffraction (XRD) is good for studying single crystals and crystalline powder samples, this method is not suitable for polycrystalline thin films and multi-layered materials. Some of the few techniques dedicated for these type of

materials are X-ray reflectivity (XRR) and grazing incidence X-ray diffraction (GIXRD) [49]. The latter probes the in-plane near-surface region of polycrystalline materials and provides information about the unit cell lattice parameters, crystal size, and structural phase identification [50]. The working principle is similar to XRD and will be provided later.

XRR is a tool for studying film thicknesses of up to $150 - 200$ nm, surface and interfacial roughness, and mass density of layered materials. An advantage on this technique is that it can be applied to amorphous materials as well. The working principle of XRR relies on measuring the specular reflection of an X-ray beam from the surface [51]. The reflectivity (or intensity) of the beam is given by Fresnel's equation:

$$R = \left| \frac{\theta - \sqrt{(\theta^2 - \theta_c^2) - 2i\beta}}{\theta + \sqrt{(\theta^2 - \theta_c^2) - 2i\beta}} \right|^2 , \tag{3.5}$$

where θ is the incident angle, θ_c and β are the critical angle and absorption term of the material, which will be explained shortly. The scattering geometry is such that the incident and reflection angles are equal, as governed by the famous Snell's Law of reflection. This is the typical Bragg-Brentano configuration employed in reflectometry experiments, where the scattering wave vector given by $K = k_r - k_i = 4\pi \sin\theta/\lambda$, is normal to the surface [49]. The index of refraction of the reflecting medium at x-ray wavelengths is given by

$$n = 1 - \delta - i\beta \tag{3.6}$$

with

$$\delta = \frac{2\pi\rho_{el}e^2}{m\omega^2} f' \tag{3.7}$$

and

$$\beta = \frac{2\pi\rho_{el}e^2}{m\omega^2} f'', \tag{3.8}$$

where e is the electron charge, ω is the frequency of the incident beam, f' and f'' are the real and imaginary parts of the anomalous or form factor f, of a chosen energy of the incident beam respectively. Equation 3.7 gives the scattering part of n and is related to the electron density ρ_{el} of the material [49], [51], [52]. Equation 3.8 gives the absorption term of the material and it is related to the absorption coefficient (or mass density, ρ) by [49]:

$$\mu = \frac{2\omega\beta}{c}, \tag{3.9}$$

where c is the phase velocity of light. Equation 3.6 shows that $n < 1$ since the imaginary part is less significant ($\beta \lll \delta \sim 10^{-6}$). For the X-ray beam propagating from air to a less dense medium, reflection occurs when the incident angle is very small [49], [51], [52]. This condition immediately implies total external reflection, where he incident angle must be less than the critical angle, θ_c:

$$\cos\theta_c = 1 - \delta \quad \text{or} \quad \theta_c = \sqrt{2\delta} \tag{3.10}$$

When the primary beam impinges on a smooth surface of a layered material at a fixed, low grazing incidence angle θ $(0.1^\circ - 3^\circ)$, it enables total external reflection from the surface and a larger penetration depth confined within the layer (and not the substrate) in investigation. This penetration depth is given by

$$z = \frac{-\lambda\sqrt{(\theta^2 - \theta_c^2) + \sqrt{(\theta^2 - \theta_c^2) + 4\beta^2}}}{4\sqrt{2}\pi\beta} \tag{3.11}$$

This equation shows that z can be controlled by changing the ratio of the grazing incidence angle to the critical angle [52]. The grazing incidence geometry allows in-plane diffraction according to Bragg's law:

$$2d\sin\theta = m\lambda \qquad\qquad m = 1, 2, 3\ldots, \tag{3.12}$$

where d is the Miller plane spacing or nearest neighbour atom distance, θ is the angle of diffraction, m is the order of diffraction and λ is the wavelength of the monochromatic x-ray beam. For a cubic unit cell, the lattice parameter a, is related to the d-spacing and Miller indices (hkl) by:

$$d = \frac{a}{\sqrt{h^2 + k^2 + l^2}} \tag{3.13}$$

In this way, the lattice parameter can be determined and hence the crystal structure of the material. For polycrystalline materials the crystallite size D can be determined using the Debye-Scherrer equation:

$$D = \frac{0.9\lambda}{\beta\cos\theta}, \tag{3.14}$$

where β is the broadening of the Bragg's peaks. The consequences of employing low grazing incidence angle is that, the Fresnel transmission coefficient T, becomes independent of the polarization of the electric field [52];

$$T = \left|\frac{2\theta}{\theta + \sqrt{(\theta^2 - \theta_c^2) + 2i\beta}}\right|^2 \tag{3.15}$$

Figure 3.8 shows the the schematic diagram of the instrumental set-up used for XRR and GIXRD experiments. The diagram follows the design of the Bruker AXS D8 Discover diffractometer [53], which was used to carry-out both XRR and GIXRD measurements in this investigation. The instrumental setup consists of five components: a copper X-ray tube connected to a high voltage generator, primary optics, sample stage, secondary optics and a detector. The 20 kHz X-ray generator is water cooled and vital for supplying the tube with an appropriate voltage and current in the ranges of $10-60$ kV and $5-80$ mA. The tube usually operates at 40 kV and 40 mA, and a rotary absorber handles the high flux of the incident divergent X-ray beam. Part of the primary optics is the Göbel mirror which converts this divergent beam into an intense collimated beam. For thicker samples and GIXRD measurements, a Ge monochromator

or analyzer is required to filter only $Cu - K\alpha_1$ radiation and thus producing a monochromatic beam with a wavelength of $\lambda = 1.5406$Å. These primary optics can be changed manually.

A vacuum pump system helps in adhering the sample onto a motorized x-y-z stage. In addition to the sample position and orientation axes, the diffractometer has four other axes whose angles are measured with a goniometer attached to a Eulerian cradle. These are, the sample rotation ω axis, which must always be aligned to the sample's surface, in-plane rotation ϕ axis, the tilting χ axis and the detector's scanning 2θ axis, respectively. These axes are crucial for a series of pre- and post-sample alignment measurements which are done using the Diffrac.suite software which controls the entire diffractometer as well. XRR profiles are collected in the $2\theta/\omega$ measurement mode. In GIXRD, the intensity is measured in 2θ mode, with ω being the fixed grazing angle (1°).

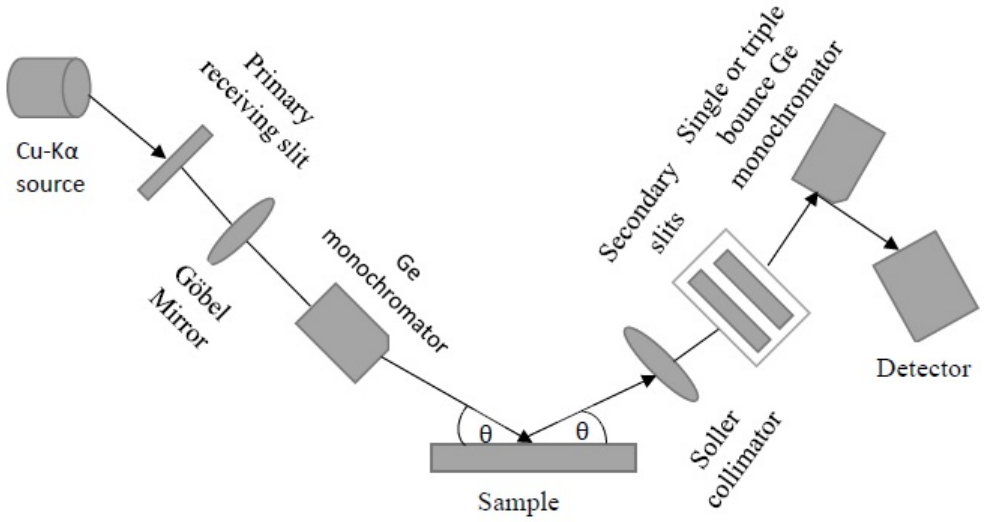

Figure 3.8: Schematic diagram for XRR and GIXRD instrumental setup.

The reflected beam from the sample is focused by a set of secondary optics which comprises of two motorized secondary slits (label E in Figure 3.8) (of 0.1 or 0.2 mm width), an equatorial soller collimator and a single or triple bounce Ge(220) monochromator. The two slits help to reduce diffuse scattering and thus providing a resolution of 0.1 nm. The diffracted beam is collimated into a parallel beam again before it reaches the detector by these secondary optics. A one-dimensional LYNXEYE detector with high scintillation counts (in counts per seconds, CPS) collects the diffracted beam. For GIXRD measurements, the secondary slits and detector slits can be a changed to 2 mm and 1 mm using the software.

A wide range of traditional XRD softwares are available (commercially and freely) for evaluating GIXRD patterns. XRR patterns are fitted using the

Diffrac *plus* Leptos software. A stacked layered sample model consisting of $GeO_2/Ge_2Sb_2Te_5/SiO_2/Si$ (shown as an inset in Figure 3.9), was used to get the simulation curve. In a typical XRR pattern (Figure 3.9) the periodicity of the interference fringes or oscillations are related to the thickness of the films under study, that is, the periodicity $= 2\pi/\text{thickness}$ [49]. The region around the total external reflectance angle or edge, is related to the film's density. The smoothness of the fringes and the steep decaying manner of the pattern, reveals information about roughness since the reflectivity diminishes with increasing roughness [54]. XRR was critical in evaluating the deposition rate of the films for $Ge_2Sb_2Te_5$ and GeTe targets. The deposition rate depends on the deposition conditions such as the working gas pressure, RF bias voltage and deposition power [39]. The deposition rates of the $Ge_2Sb_2Te_5$ and GeTe thin films were determined to be 27 nm/min and 32 nm/min, respectively. These were further used to deposit films of varying thickness.

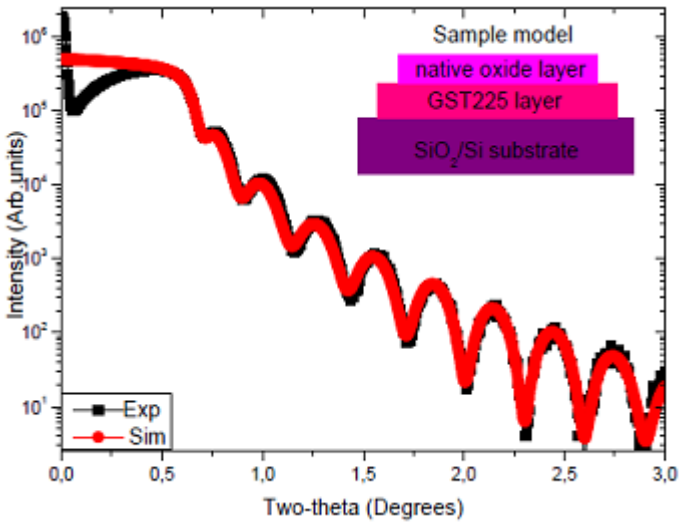

Figure 3.9: XRR pattern of the as-deposited $Ge_2Sb_2Te_5$ sample. The insert is the simulation sample model used for determining the deposition rate.

3.3 Vibrational Properties

3.3.1 Micro-Raman Spectroscopy

The inelastic scattering of light by optical phonon modes is known as Raman scattering. According to classical theory, these modes are Raman-active (can be detected) if and only if the oscillation of the optical modes causes a change in the polarizability of the molecule, otherwise the phonon mode is regarded as Raman-inactive [48]. Therefore, other techniques such as inelastic neutron scattering and Fourier transform infrared (FTIR) spectroscopy are needed to detect such modes. In contrast to a quantum mechanical description, the

Raman Effect can be described by electronic transitions between different vibrational energy levels in a molecule [48], [12]. It comprises of Stokes and anti-Stokes scattering as explained in the previous chapter. Some of the advantages of Raman spectroscopy are that it requires no sample preparation and that the spectrum can be acquired in a short time scale of at least 30 seconds. Owing to the instrument's high sensitivity to aqueous absorption bands, liquid and gaseous samples can also be measured in addition to solids [48].

The optical phonons can be detected by measuring the intensity of the scattered phonons as a function of Raman shift (frequency in wavenumbers or cm^{-1}), this is shown in Figure 3.10. The instrumentation comprises of an excitation laser source, a double or triple monochromator, illuminating optics and a signal processing system composed of a detector, an amplifier and output device [12]. In this study, micro-Raman spectroscopy was utilized and the schematic diagram is shown in Figure 3.11. This form of Raman spectroscopy has an optical microscope integrated with the spectrometer [12]. A triple Jobin Yvon T64000 spectrometer [55] with a choice of diffraction gratings with 600 or 1800 grooves/mm is available in the laboratory. The spectrometer is equipped with a Olympus BX40 confocal microscope with an x-y motorized stage. The microscope has multiple objective lenses for illuminating the sample and for producing magnified images during the point by point or laser scanning mode [55].

The detection system used is a charge coupled detector (CCD) with 256×1024 pixels, which can capture the Raman spectrum in a single acquisition. This is a silicon-based semiconductor detector with a higher sensitivity to the Stokes inelastically scattered light compared to photomultiplier detectors [48]. The CCD is usually housed in a tube filled with liquid nitrogen for cooling it. A typical Raman spectrum (Figure 3.10) is a plot of Stokes scattered light intensity versus Raman shift (frequency in wavenumbers, that is, cm^{-1}). The laser used in this technique was a coherent INNOVA model 308 Ar^{+} laser, which has a large spectral range, from ultra-violet to the near-infrared region [55]. All measurements were taken with $\lambda = 514.5$ nm and a laser power of 0.4 mW. A holographic edge filter is usually inserted in the optical pathway to block the fluorescence background, any plasma lines from the laser, and elastically scattered light which is more intense than the Stokes light [48].

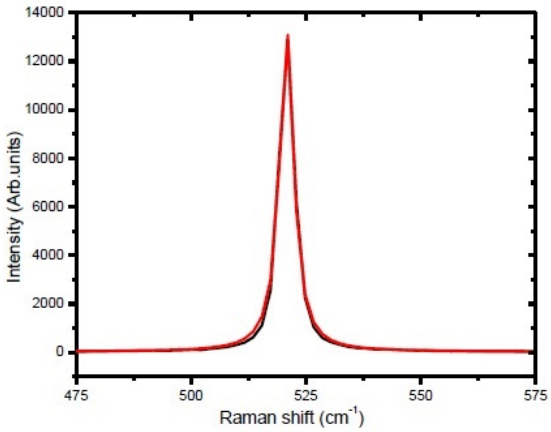

Figure 3.10: A typical Raman spectrum showing the G-mode centred at 520.8 cm^{-1} of the Silicon sample used for calibration. The spectrum was fitted with a Gaussian function.

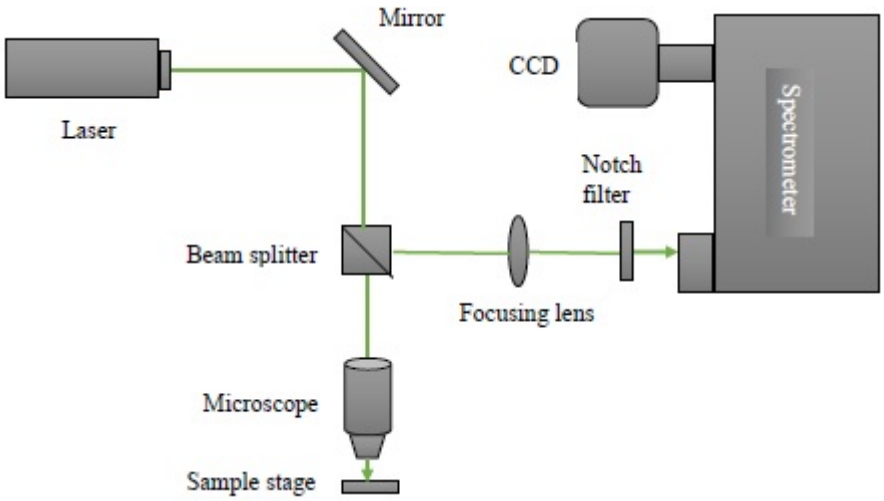

Figure 3.11: Schematic diagram of the Raman micro-spectroscopy setup. Adapted from Ref.[12]

3.3.2 Surface Brillouin Scattering

Surface Brillouin scattering is a non-destructive technique for measuring the properties of SAWs that are probed by the inelastic scattering of light near the surface of thin films and in bulk solid materials. This is the only method that can detect acoustic waves directly, in the $2 - 30$ GHz frequency region [32], [7]. Thus, measurement of such waves requires sensitive equipment with a high contrast and resolution. Therefore a Brillouin spectrometer consists of a laser, external focusing optics to guide the laser beam into the interferometer, and an interferometer to analyze the scattered light from the sample. The laser helps to optically probe the acoustic excitations, which are naturally present in solids

[7]. Therefore a high contrast multi-pass tandem Fabry-Perot interferometer of Sandercock type is required to resolve the Brillouin frequency shifts [13]. This is because the intensity of the inelastically scattered light in SBS is small compared to elastically scattered light, in contrast to Raman scattering [32]. A detector and multi-channel analyzer (MCA) or personal computer capture the spectral data.

The Laser

Spectroscopic techniques usually require light sources that are monochromatic. Lasers are typically used in fulfilling this requirement, due to their coherence. In this study, the Torus 532 laser from Laser Quantum was used to carry out SBS measurements [56]. This diode pumped solid state (DPSS) class IV laser is a continuous single longitudinal mode (SLM) laser with a wavelength of 532 nm, a beam diameter of 1.7mm $\pm$ 0.2 and a spectral bandwidth of 1MHz. It has a long coherence length ($>$ 100 m). The vertically polarized (horizontal polarization is also available) light laser constitutes a transverse electromagnetic TEM_{00} spatial mode and has a divergence of $>$ 0.4 mrad. It produces output powers in the range of $50 - 750$mW which makes it suitable for SBS measurements of relatively elastically soft materials, such as the alloys under study and for biological samples. The influence of the output power on the sample structural phase was studied to determine the appropriate measuring power that does not engender phase transformation during the life cycle of the experiment (see section 4.2).

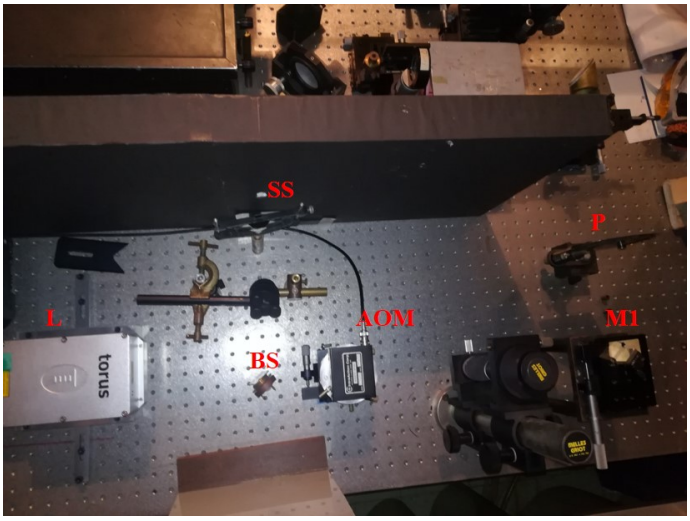

Figure 3.12: A photo showing the Quantum Torus laser (L) together with some of the external focusing optics, namely the beam splitter (BS), shutter system (SS), acousto-optic modulator (AOM), mirror one (M1) and a polarizer (P).

The Torus 532 has numerous advantages over the Argon ion laser which

was used in previous studies [26]:

- It prevents mode-hopping by continuously tracking its SLM beam position by using special electronics. Thus the use of an intra-cavity etalon is not required for this purpose since the laser is a SLM. The intra-cavity etalon is essential for selecting a SLM, while suppressing other frequencies in multi-wavelength lasers, and hence functions as an optical filter
- It takes less than 30 minutes to warm-up and operates at a wide temperature range of $15 - 35\,^{\circ}\mathrm{C}$.
- It uses a PSU cooler instead of flowing water.
- It produces ultra low noise by utilizing a travelling-wave cavity.
- Ease of operation using a TruLoQ function to enable emission and the power or current can be adjusted in percentages.

Figure 3.13 shows the calibration curve of the laser done to determine a suitable SBS measuring power for the two chalcogenide alloys in investigation. This is of paramount importance, since these materials are relatively soft and thus prevention of structural phase-changes or laser based ablation during data acquisition is necessary.

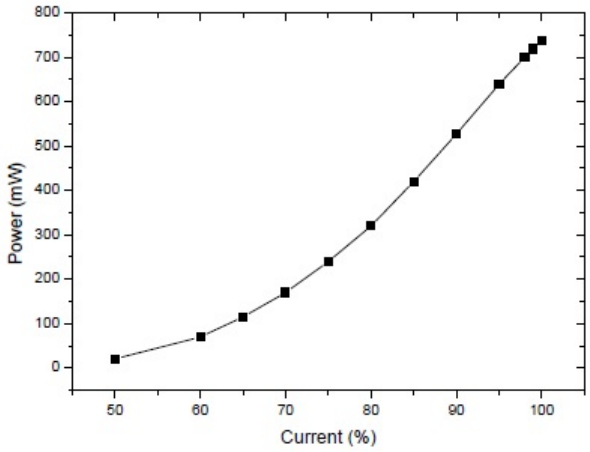

Figure 3.13: Power versus current calibration curve of the Torus 532 laser.

External Focusing Optics

The laser beam usually is controlled by a set of focusing optics mounted externally on the optical table and guided to the sample and then into the interferometer. Starting after the laser, a beam splitter (BS) is used to split the laser beam into two halves. One half is reserved as a reference light and is blocked from entering the detector by a shutter control system. This shutter

(SS) has an adjustable window period which is necessary for controlling the system signal during stabilization of the interferometer mirrors [7].

The other half passes through the acousto-optic modulator (AOM). This enables a continuous variation of the laser power on the sample and is shown in Figure 3.12. Then this beam passes through a polarizer (P) and is focused by an elliptically dielectric coated mirror (EM) with a 0.2 cm hole in the center onto the sample via a front doublet achromatic lens (L1) with a focal length of 12 cm. In the back-scattering configuration, the scattered light from the sample is guided "back" through this mirror in the same optical path as the incident light. It is then focused by a second analyzer lens (L2) with a focal length of 40 cm and directed into the interferometer (TFPI) through the pinhole (PH) by two walking mirrors (WM1 and WM2). With these mirrors, the scattered light can be steered into additional degrees of freedom during the interferometer alignment process. These optics and the sample stage (SS) are shown in Figure 3.14 below.

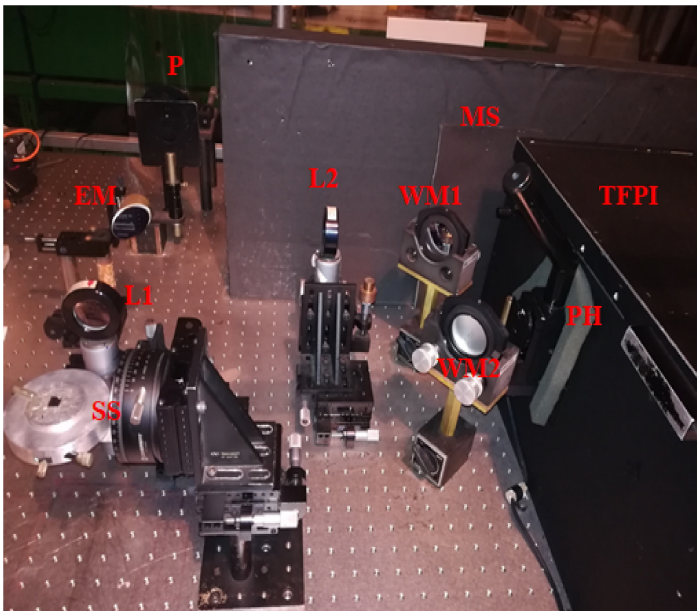

Figure 3.14: A photo showing the external focusing optics, namely the polarizer (P), elliptical mirror (EM), lens one (L1), lens two (L2), walking mirrors one and two (WM1 and WM2), and a sample stage (SS).

Multipass Tandem Fabry-Perot Interferometer

A Fabry-Perot interferometer (FPI) is typically used in spectroscopic techniques where a high resolution of MHz to GHz is required. This optical instrument works as a band-pass filter that transmits light of its resonant frequency [32]. It is constructed by mounting two flat plane mirrors an optical distance L_1 parallel to one another. By adjusting the resonant frequency and the optical spacing, a scan of the light intensity at various wavelengths can be obtained.

Hence in this way the FPI can be used as a spectrometer [32]. The transmitted wavelengths are given by

$$T = \frac{\tau_0}{1 + (\frac{4F^2}{\pi^2}) \sin^2(\frac{2\pi(L_1)}{\lambda})}, \tag{3.16}$$

where τ_0 is the possible maximum transmission as determined by the losses in the system, and F is known as the finesse [13], which will be encountered shortly. For one to observe peaks in the FPI scan spectrum, the transmitted light must interfere constructively:

$$2L_1 = m\lambda, \tag{3.17}$$

where m is a positive integer. The relation between the resolution $\delta\lambda$ of the FPI and F is given by

$$F = \frac{\Delta\lambda}{\delta\lambda}, \tag{3.18}$$

where $\Delta\lambda$ is known as the free spectral range (FSR); this is the separation of the neighbouring transmitted frequencies (peaks), and is given by $c/2L_1$ (where c is the phase velocity). In terms of the mirror reflectivity R, the above equation can be rewritten as

$$F = \frac{\pi\sqrt{R}}{1 - R} \tag{3.19}$$

However, for Brillouin spectrometry, both the Stokes and anti-Stokes shifted features have a smaller intensity compared to the elastic peak which has a larger intensity in the order of 10^4 [32]. This is because of the traditional design of a single FPI. Even combining two FPIs does not alleviate some of the problems encountered (refer to the user manual [13]) since the scan is non-linear. Therefore, mirror alignment and the stability of the interferometer are critical since any alteration is detrimental to the resolution, which is dependent on the mirror spacing. Therefore, a high FSR at fixed resolution, with a good contrast can be obtained using a multi-pass tandem interferometer [13]. This tandem setup is constructed by combining two FPIs on a compound scanning translational stage such that the second FPI has an optical spacing L_2 close to that of the first one, i.e.

$$L_2 = L_1 \cos\theta = 0.95L_1, \tag{3.20}$$

where θ is the angle between the two interferometers as seen in Figure 3.15. Synchronous scanning of the two FPIs, is achieved by a piezoelectric transducer acting as a deformable parallelogram (which is part of the translational stage) [34]. The purpose of the translational stage is to enable scanning of the mirror spacing, without altering the parallel alignment. This change in mirror spacing δL_1 and δL_2 is given by

$$\frac{\delta L_1}{\delta L_2} = \frac{L_1}{L_2} \tag{3.21}$$

Thus in this way, the FSR can be increased at a fixed resolution. The mirror spacing is measured by a capacitive displacement transducer. In this work, a

mirror spacing of 4 mm was used to provide a FSR of ±40 GHz. This was sufficient for observing all surface excitations in $Ge_2Sb_2Te_5$ and GeTe. An even higher FSR can still be obtained by simply changing the mirror spacing. A high contrast (in the order of $10^{11} - 10^{12}$) can be achieved by allowing the transmitted light (or backscattered light in SBS experiments) to pass multiple times in the interferometer before it reaches the detection system [32]. In this work, a JRS $3+3$ tandem FPI as developed by Sandercock was used to carry-out SBS measurements [13]. The multi-passing is possible by making use of corner-cube prisms inside the interferometer setup, which fold the light [6].

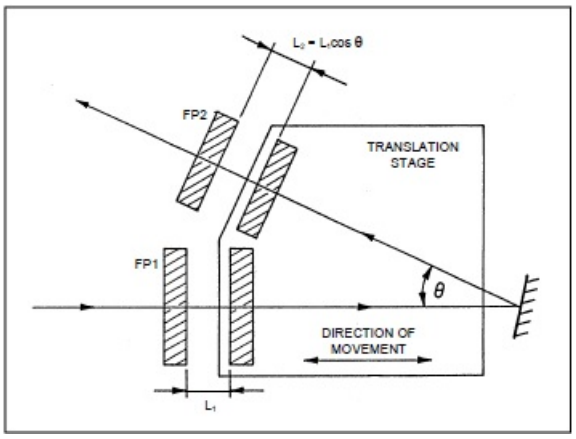

Figure 3.15: Schematic diagram of a TFPI showing the principle configuration of scanning two FPIs synchronously. [13]

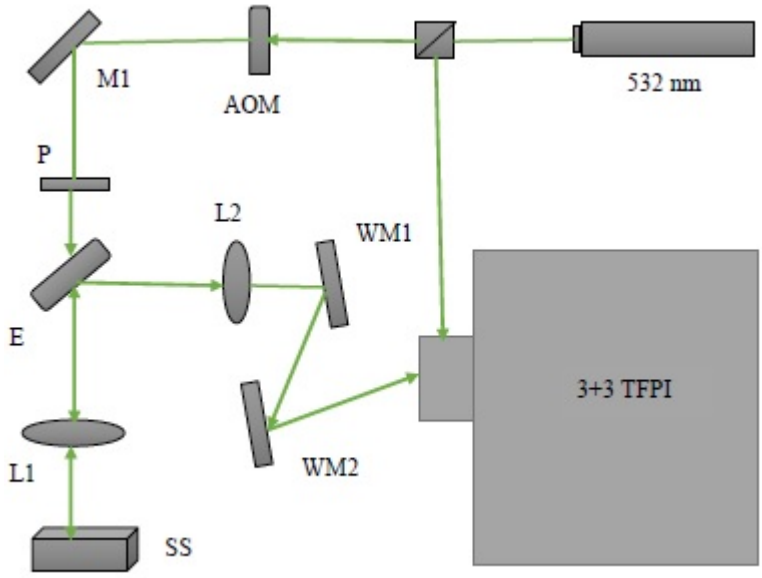

Figure 3.16: A schematic diagram of a complete set-up of a Brillouin spectrometer comprising of a laser, external focusing optics and a 3+3 pass tandem Fabry-Perot Interferometer. Adapted from Ref.[14]

It is of paramount importance for this set-up to be shielded against any vibrations propagating in the building or atmosphere. Otherwise any attempt to measure the frequency of the acoustic waves will be almost impossible, if not pointless. Thus a JRS Scientific dynamic isolation system with excellent directional and positional stability is used for this purpose. All the optics of the interferometer are shielded in a black Aluminium box which is mounted on this isolation system. This completely isolates the interferometer from the optical table [13].

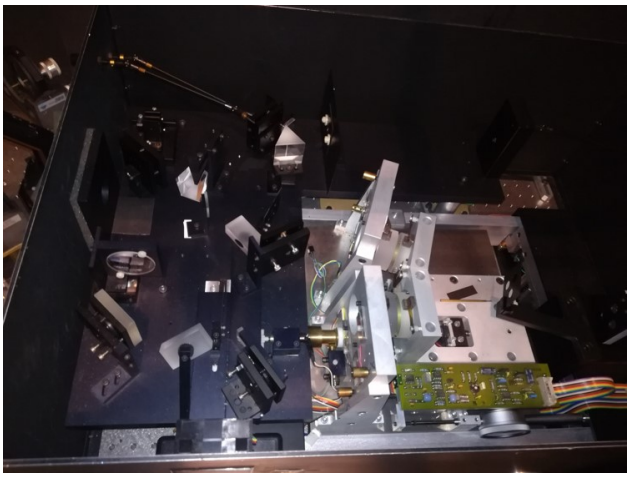

Figure 3.17: A top-view of the JRS $3+3$ pass tandem Fabry-Perot Interferometer; the system is usually shielded.

Figure 3.17 shows the top-view of the interferometer under no operation, that is, when there is no laser light passing through the internal optics. Day to day operation of the interferometer requires proper alignment so as to achieve mechanical stability before any measurement can be undertaken. This requires the optimization of the backscattered light in reflection mode (or align mode). During this operation, the intensity of the six reflected peaks (three from each FPI) is maximized by making use of an interferometer control unit. Then the peaks are merged (resulting in only three peaks) so as to allow for synchronous operation of the two FPIs. The interferometer is then switched to tandem mode operation (this is shown in Figure 3.16); here only the central peak's intensity is maximized. In general, the two furthest peaks should be suppressed in this mode However, due to instrumental artefacts, small ghost peaks still remain. Thereafter the interferometer can be stabilized by opening of the shutter system to allow the reference laser beam to pass through before data acquisition.

Spectral Collection

Figure 3.18 displays a combination of a personal computer (PC) multi-channel analyzer (MCA) connected to the AOM and the TFPI control units (ICU)

for full operation on the instrumentation and for spectral collection (together with a detector which is shielded). To ensure good spectral quality and integrity, a detector with a high signal-to-noise ratio is usually required. In this work a EG&G Optoelectronics Canada Silicon avalanche diode detector (model SPCM−200−PQ) is available in the laboratory to detect the backscattered light after it is analyzed by the interferometer. Because this device is sensitive to stray and elastically scattered light, it is usually shielded by the black box to avoid damage. By selecting a scan amplitude of 84.53 GHz, the 512 channels can be counted in duration of 0.5 s per channel. The overall spectral acquisition time (which was $6 - 24$ hours) depends on the experimental parameters, and the nature of the material in investigation.

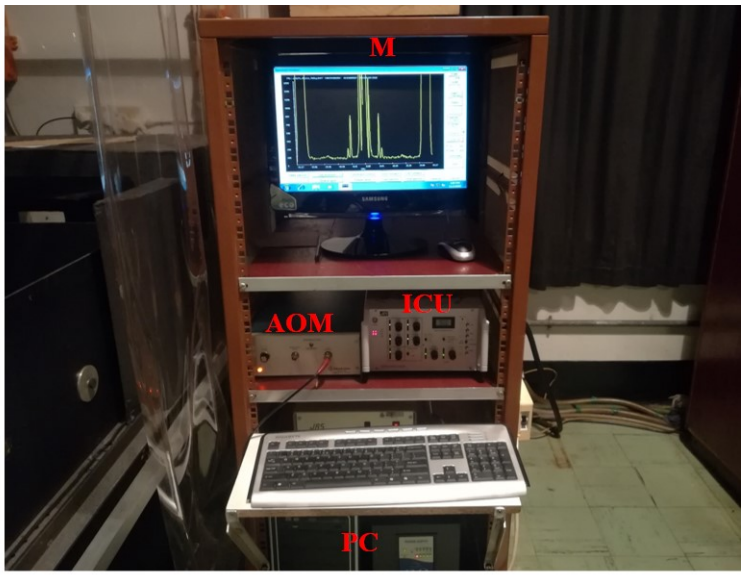

Figure 3.18: A photo showing the TFPI control unit (ICU), acousto-optic modulator (AOM) control unit, together with the monitor (M) and personal computer (PC) used to collect the spectrum. The detector is not shown here since it is always shielded from stray light.

A typical SBS spectrum is shown in Figure 3.19. This spectrum consists of negatively and positively shifted frequency peaks known as the Stokes and the anti-Stokes scattered peaks, respectively. These two regions are separated by a zero-shifted frequency peak known as the elastic peak. The two peaks occurring around frequency shifts of $\pm(35 - 42)$ GHz are the ghost peaks. Usually, the most intense peak occurring at lower frequencies represents the Rayleigh surface acoustic wave (RSAW). Higher frequency modes in $Ge_2Sb_2Te_5$ and GeTe were also excited and these are known as Sezawa waves (SW). These modes were observed when the film thickness and angle of incidence were varied in the range of $50 - 500$ nm and $40 - 70°$C. All measurements were done in a backscattering geometry.

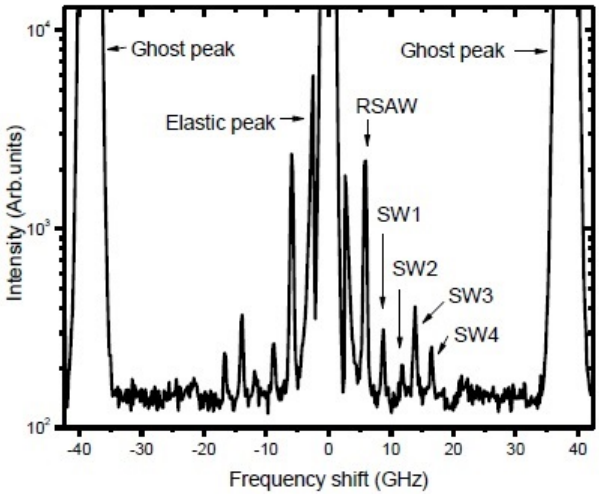

Figure 3.19: Typical SBS spectrum of a 150 nm $Ge_2Sb_2Te_5$ film annealed at 200°C measured at an incidence angle of 66°, showing various excitation modes.

Chapter 4

Structural Characterization of $Ge_2Sb_2Te_5$ and GeTe

This chapter presents the structural properties of $Ge_2Sb_2Te_5$ *and* GeTe *evaluated by various characterization tools. The first subsection aims at determining the chemical composition of the films grown by Radio Frequency Magnetron sputtering using Rutherford Backscattering spectrometry (RBS) and energy dispersive X-ray spectroscopy (EDS) coupled with field emission scanning electron microscopy (FESEM). The former was also utilized to determine the atomic density of the films. X-ray reflectivity (XRR) was used to extract the thickness and density of the films, whereas grazing incidence X-ray diffraction (GIXRD) was used to determine the lattice parameters of the various structural phases. These characterization techniques (except EDS) have been chosen because of their non-destructive nature. The optical phonon modes were studied using micro-Raman spectroscopy.*

4.1 Chemical Composition by Rutherford Backscattering Spectrometry

The control of the chemical composition is important especially in the growth of films from sputter targets made from volatile elemental constituents. Also, knowing the chemical composition of the films helps in establishing the level of purity or type of contaminants present in the films. Defects in films and devices are mainly introduced through contamination during the post-synthesis treatment of films and fabrication of devices and therefore affect their performance. One technique which is good at probing the chemical composition is Rutherford Backscattering spectrometry (RBS). Energy dispersive X-ray spectroscopy (EDS) coupled with field emission scanning electron microscopy (FESEM) was also used as a complementary method for this purpose as well.

4.1.1 $Ge_2Sb_2Te_5$

Three samples prepared with the same deposition parameters, were investigated. One, was as-deposited and the other two were annealed at 200 °C and 350 °C, respectively. As seen in Figure 4.1 (a-c), the chemical constituents of the films were found to be Germanium (Ge), Antimony (Sb) and Tellurium(Te). The Te and Ge peaks are superimposed since they have similar atomic masses and RBS could not resolve the two due to it poor mass resolution. The slight deviation from the stoichiometry in the chemical composition of the films is similar to those observed by Lyeo *et al.* (2006) of Ge : Sb : Te = 22.5 : 23.3 : 54.2, as determined using X-ray fluorescence spectroscopy (XRF) [57]. In general, a stoichiometric ratio of Ge : Sb : Te = 2 : 2 : 5 was obtainable from the sputter target used in this study.

It must be noted that the detected silicon (Si) signal is due to the wafer used as the substrate. Even though the substrate had a native silicon oxide (SiO_2) layer on-top, the oxygen peak is weak. This is because the RBS technique used in this study has a low resolution and hence a lower sensitivity for low atomic elements. Another reason is that the simulations reveal a very thin layer with a thickness of about 3 nm for this oxide and therefore, oxygen (O) may not be present on the film's surface. Moreover, this oxide layer is at the interface between the substrate and the $Ge_2Sb_2Te_5$ layer and since the samples were tilted at an angle of 5 ° to avoid channeling effects of the He^{2+} ions, this layer might have been hard to probe. However, it must be mentioned that this can be investigated further by performing depth profiling measurements with this technique.

In addition to the above mentioned three samples, two other samples were annealed at 430 °C and 480 °C. These temperatures are in the range wherein the hexagonal phase of $Ge_2Sb_2Te_5$ is most stable. As seen from Figure 4.1 (d) and (e), the chemical elements present in these two samples are the same as in the other three samples. The effect of annealing the samples at various temperatures is evident from the film thicknesses. This is shown in Table 4.1. There is a thickness change of 10.1 % between the first three samples and of 12.2 % between the last two samples, respectively. Generally, this is indicative of a loss of mass with increase in the annealing temperature. This will be investigated further by X-ray reflectivity in the next section.

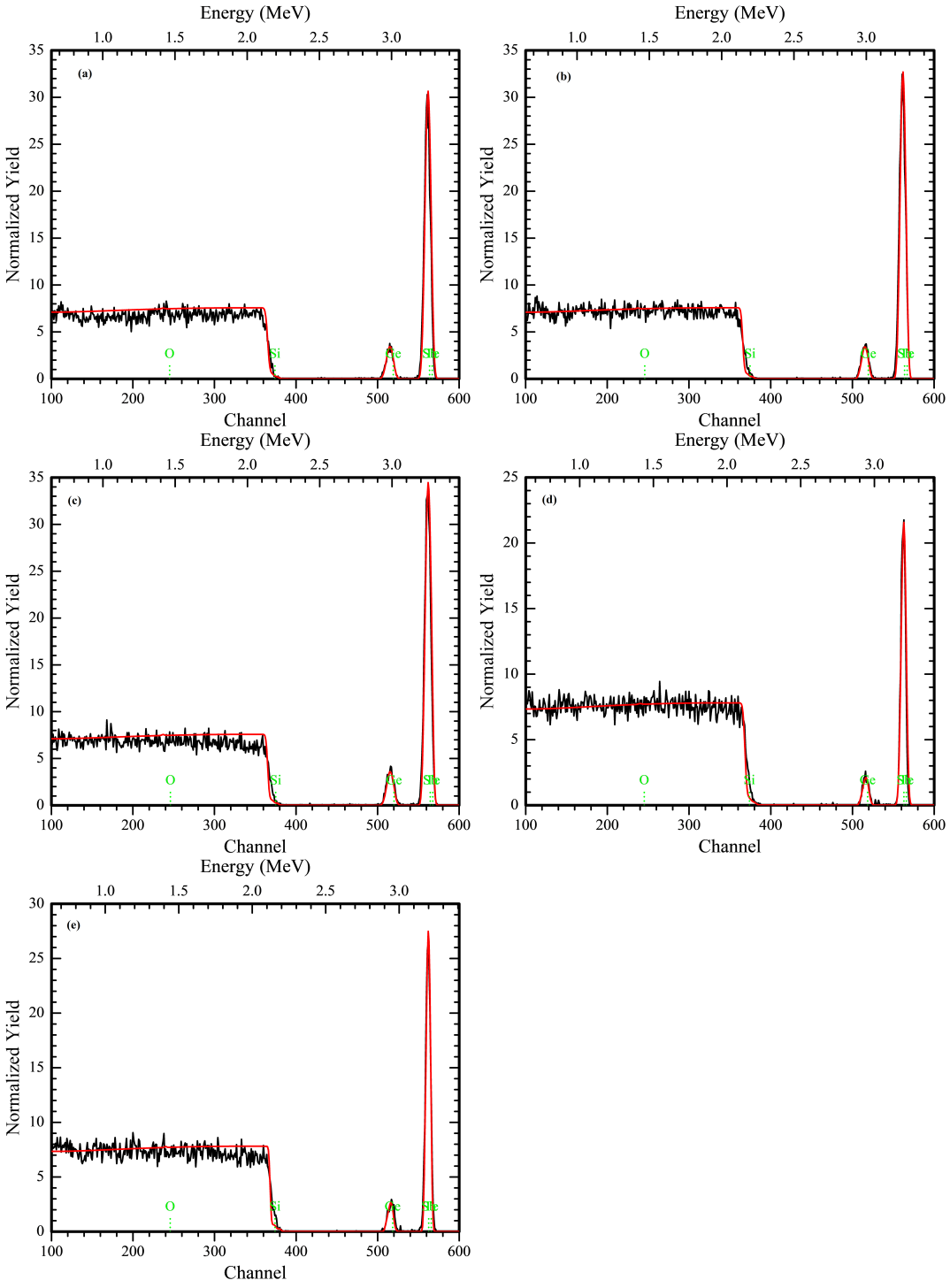

Figure 4.1: RBS spectra of $Ge_2Sb_2Te_5$, (a) as-deposited sample and films annealed at temperatures of (b) 200 °C, (c) 350 °C, (d) 430 °C and (e) 480 °C. The black and red lines correspond to the measured data and simulated data as determined using XRump, respectively.

The atomic density, n, of the as-deposited sample was found to be 3.0 $\times$ 10^{22}atoms. cm^{-3}. This in agreement to within 1.4% with 3.09$\times 10^{22}$atoms. cm^{-3}

Table 4.1: The stoichiometry, thickness, areal and atomic densities, of Ge : Sb : Te films annealed at different temperatures.

T_A (°C)	Ge : Sb : Te (atomic %)	Thickness, t (nm)	Areal density N ($\times 10^{15}$ atoms cm^{-2})	Atomic density, n ($\times 10^{22}$ atoms cm^{-3})
T_{Room}	25.0 : 21.0 : 54.0	87.0	265.0	3.0
200	23.8 : 22.0 : 54.2	79.0	262.0	3.3
350	23.4 : 22.0 : 54.6	87.0	294.0	3.4
430	23.4 : 22.0 : 54.6	43.0	146.0	3.4
480	23.6 : 22.0 : 54.4	49.0	166.0	3.4

as determined from the same technique by Lyeo *et al.* (2006) [57]. Akola and Jones (2007) also reported a similar value of 3.082 $\times$ 10^{22} atoms. cm^{-3} as determined from theoretical calculations [58]. Their value for the cubic phase, of 3.307 $\times$ 10^{22} atoms. cm^{-3}, is also similar to our value of 3.3 $\times$ 10^{22} atoms. cm^{-3} for the sample annealed at 200 °C. This is an increase of 8.9 % following the amorphous to cubic (NaCl-like) phase transition. In contrast to the cubic to hexagonal phase transformation, a slight increase in n of 1.9 % was observed, and this is for the sample annealed at 350 °C, with $n = 3.4 \times 10^{22}$ atoms cm^{-3}. This value is in good agreement with 3.40 $\times$ 10^{22} atoms. cm^{-3} reported by Tsafack *et al.* (2011) [59]. In general, an increase in the atomic density was observed as the annealing temperature was increased; this is clearly associated with the change in the structural configuration of the atoms.

4.1.2 GeTe

Two identical sets of GeTe samples were investigated in this chapter, both with thickness in the range of $10 - 500$ nm. One set comprised of as-deposited films, $a -$ GeTe, and the second one comprised of films annealed at 230°C to induce a structural change to the crystalline rhombohedral phase, $c -$ GeTe. Here four samples of as-deposited GeTe were analyzed using RBS to determine the atomic density as well as the chemical composition. Figure 4.2 shows the elemental constituents of each sample. Again, the backscatter edge of Si is from the substrate, while O is from the native SiO_2 layer. Lastly, the Ge and Te signals are from the sputter target were detected. It can be noted that for the two thinner samples, Thallium (Tl), was detected at channel number 591.507. This could be due to the channeling effects of the α particles with the constituents of the standard sample used for calibration. This standard sample is composed of Gold, Cobalt, Nickel, Carbon and Oxygen. To prevent this from happening further, the samples were tilted at an angle of 5 °, hence Tl is not seen in the RBS spectra of the thicker samples, that is, Figure 4.2 (c) and (d).

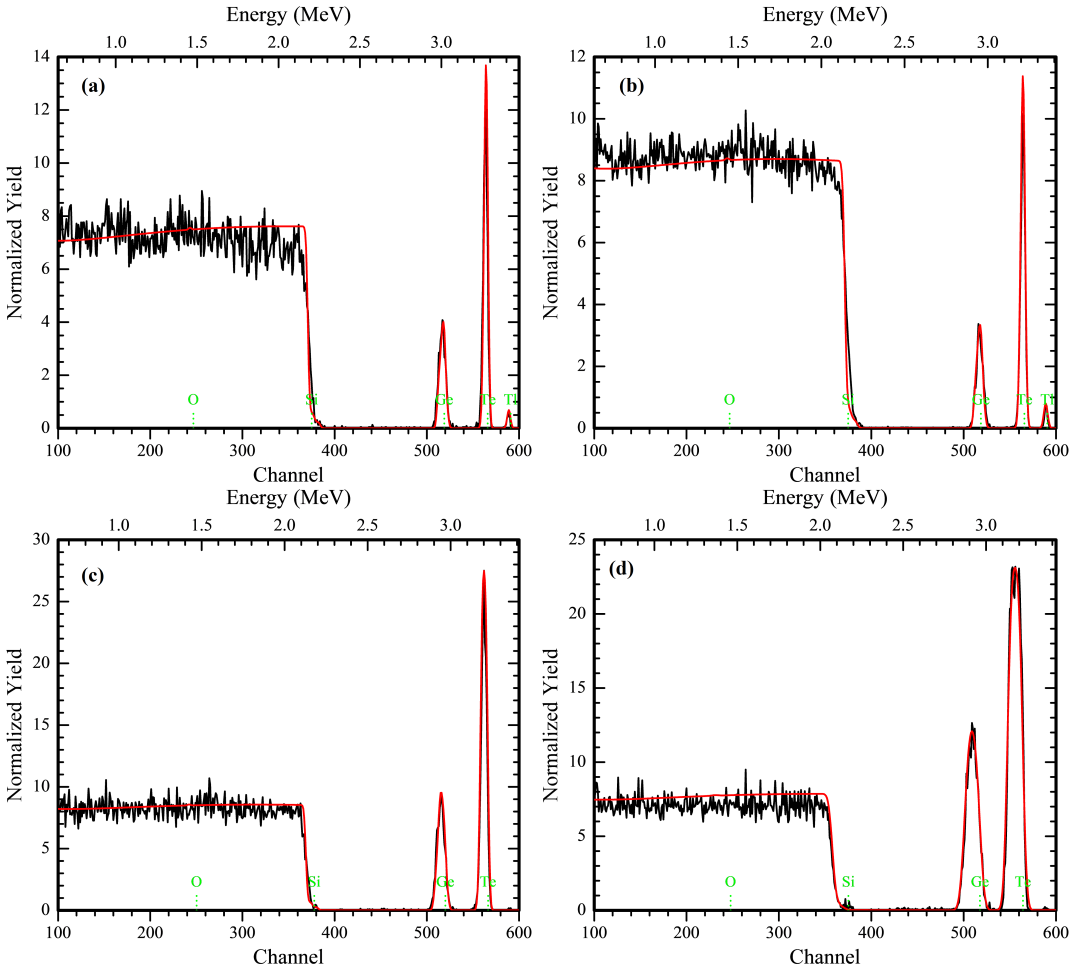

Figure 4.2: RBS spectra showing the chemical constituents of the as-deposited GeTe films with thickness of (a)25.9 nm, (b) 30.7 nm, (c)83.5 nm and (d) 168 nm respectively. The black and red lines show the measured and simulated data, respectively.

The chemical composition of the as-deposited films in atomic % is centered around a ratio of Ge : Te = 52.3 : 46.5 as seen in Table 4.2. Compared to the films annealed at 230 °C (as seen from Table 4.3) there is a variation in the chemical composition. This difference could be due to a change in the working pressure during deposition of the films on different days. Also, GeTe has a low chemical and structural stability due to its high sublimation rate [60]. This could explain the high thickness variation between the as-deposited and annealed films, which were sputtered at the same deposition rate. This is evidence of mass loss which occurs upon annealing. Both of the as-deposited and the annealed films are composed of Ge and Te as seen from Figures 4.2 and 4.3, respectively. The Tl signal observed in the 25.9 nm thick as-deposited film can be taken as an artefact. Generally, both the amorphous and crystalline films are Ge-rich, that is, the content of the Ge is greater than that of Te. A summary of the fitting parameters for the as-deposited films is given in table 4.2.

Chemical composition (atomic %)	Thickness, t (nm)	Areal density, N ($\times 10^{15}$ atoms cm^{-2})	Atomic density, n ($\times 10^{22}$ atoms cm^{-3})
Ge:Te:Tl 52.3:46.5:1.2	25.9	94.0	3.6
Ge:Te:Tl 53.4:45.8:0.8	30.7	135.0	4.4
Ge:Te 52.3:46.5	83.5	280.0	3.4
Ge:Te 52.3:46.5	168	595.0	3.4

Table 4.2: Thickness, areal and atomic densities of the as-deposited GeTe films with various chemical composition as determined from the RUMP Code.

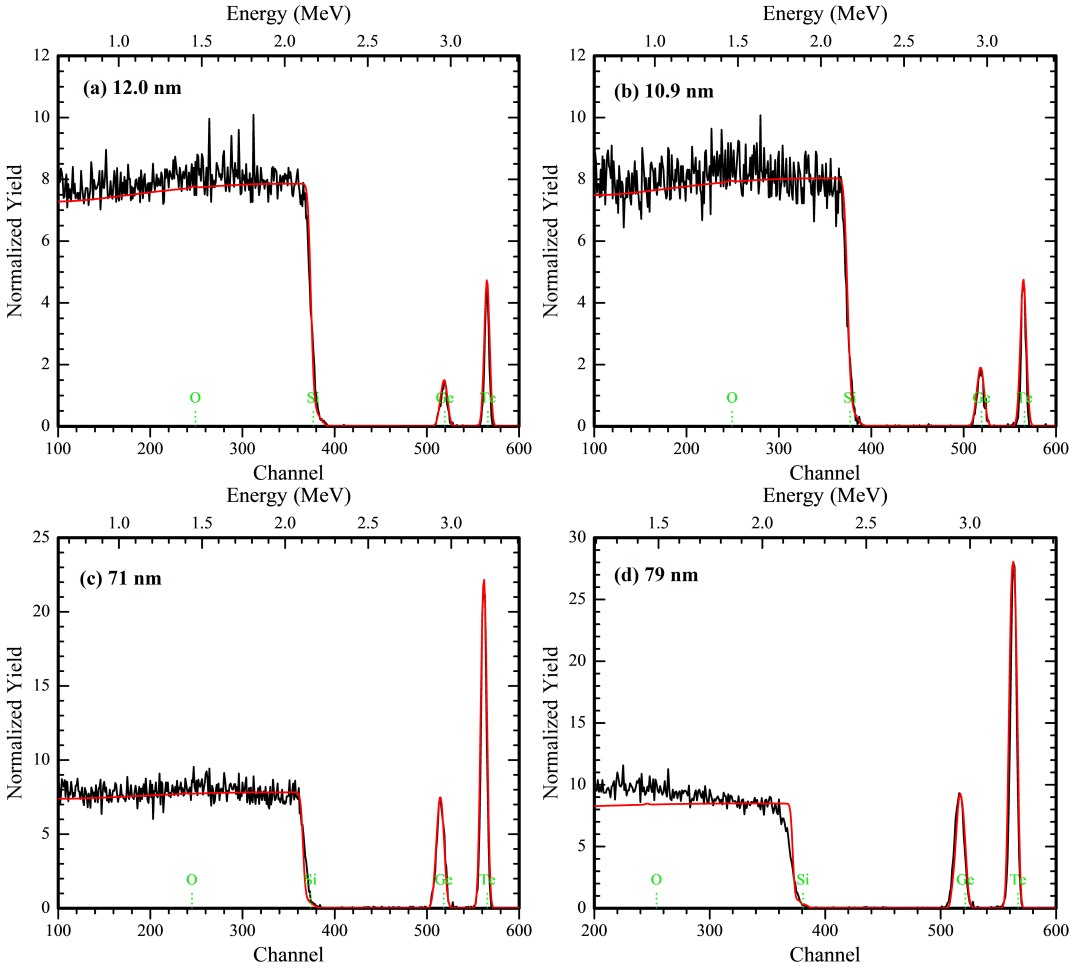

Figure 4.3: RBS spectra showing the chemical elements of the GeTe films annealed at 230 °C with thickness of (a) 12.0 nm, (b) 10.9 nm, (c) 71.0 nm and (d) 79.0 nm respectively. The black and red lines show the measured and simulated data, respectively.

The average atomic densities of $a-$GeTe and $c-$GeTe are, 3.7×10^{22} atoms. cm^{-3}

and 4.0×10^{22} atoms. cm^{-3}, respectively. These values are out of the range compared to one reported by Akola and Jones (2007, 2008) of 2.827×10^{22} atoms. cm^{-3} and 3.351×10^{22} atoms. cm^{-3} as determined from molecular dynamics simulations [58], [61]. The discrepancy could be due to the difference in the stoichiometry (which implies different structural properties [62]); Ge : Te = 15 : 85 and Ge : Te = 50 : 50 for $a-$GeTe and $c-$GeTe, respectively. Another discrepancy is because the authors determined the atomic density of $c-$GeTe using the mass density of the amorphous phase of 5.61 g cm^{-3}. Therefore for this study, the difference in the stoichiometry of the films can be attributed to this inconsistency as seen from Table 4.3.

Chemical composition (atomic %)	Thickness, t (nm)	Areal density, N ($\times 10^{15}$ atoms cm^{-2})	Atomic density, n ($\times 10^{22}$ atoms cm^{-3})
Ge:Te 56.9:43.1	10.9	56.0	5.1
Ge:Te 52.3:47.7	12.0	46.0	3.8
Ge:Te 52.5:47.5	71.0	260	3.7
Ge:Te 51.1:48.9	79.0	275	3.5

Table 4.3: Thickness, areal and atomic density of the GeTe films annealed at 230 °C with various chemical composition as determined from XRump.

4.2 Energy Dispersive X-ray Spectroscopy and Field-Emission Scanning Electron Microscopy

Another technique utilized for quantification of the chemical composition of the films, is EDS. It was chosen as a complementary technique to RBS. In this case, the chemical composition is given from characteristic X-rays emitted as a result of electronic transitions between certain atomic orbital shells of a particular element, in accordance to the selection rules of the transition [48]. Figure 4.4 shows the EDS spectrum of the 87.0 nm $a-Ge_2Sb_2Te_5$ sample. The spectrum was taken at two spots on the FESEM image (not shown here), thus resulting in a slightly different composition in atomic.% of Ge : Sb : Te = 16.1 : 16.8 : 36.9 and Ge : Sb : Te = 18.0 : 18.2 : 41.0, without the contribution of the substrate. The detected oxygen levels were 6.7 atomic.%. This shows that for low atomic number elements, this technique is better compared to RBS. For a 38.0 nm thick sample annealed at 200°C, ratios of Ge : Sb : Te = 2.0 : 1.7 : 4.6 and Ge : Sb : Te = 1.8 : 1.6 : 4.1 were obtained. The corresponding EDS spectrum is given in Figure 4.5. The low levels of the elements detected for this sample compared to the amorphous one, can be attributed to the thickness difference.

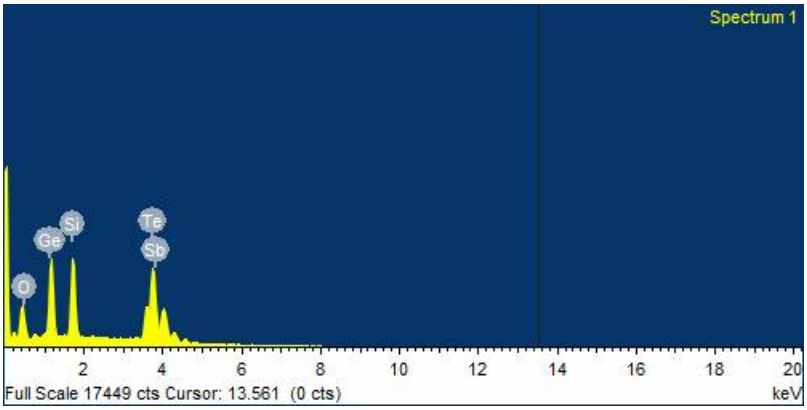

Figure 4.4: EDS spectrum of a 87.0 nm thick a $-$ $Ge_2Sb_2Te_5$ sample. Magnification of 500$\times$ and an emission gun voltage of 10.0 kV were utilized.

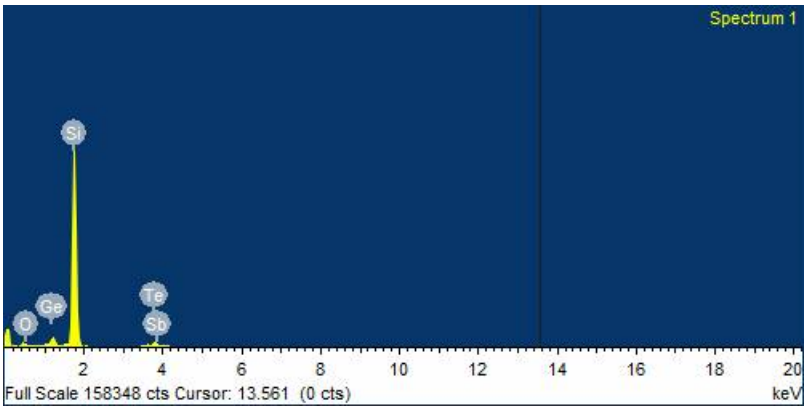

Figure 4.5: EDS spectrum of a 38.0 nm $Ge_2Sb_2Te_5$ film annealed at 200 °C. The image used for elemental composition mapping was taken at 500$\times$ magnification and with an emission gun voltage of 10.0 kV.

For a 30.7nm thick $a-$GeTe sample, an average composition of Ge : Te = 2.4 : 2.5 atomic.%, was obtained for measurements made at two different spots on the film's surface also, without the contribution of the substrate. The corresponding spectrum is shown in Figure 4.6. Compared to the annealed film ($c-$GeTe) of the same thickness, an average composition (in atomic %) of Ge : Te = 0.6 : 0.6 was obtained, and the spectrum is given in Figure 4.7. In general, the ratios obtained by EDS are lesser than those obtained from RBS studies for both of GeTe and $Ge_2Sb_2Te_5$ films. This is because EDS does not probe the chemical composition of the entire scanned area 600 $\times$ 600 μm^2 but that of a chosen spot on the film. In RBS, the He^{2+} beam covers a much larger scan area of 1000 $\times$ 1000 μm^2 and therefore, it is suitable for this purpose. The O signal detected could be from the SiO_2 (on the Si substrate) and or GeO_2 that might have formed on the surface of GeTe films. One of the requirements for SEM characterization is that the sample must be conductive; insulating samples are usually coated with carbon (C) or a metal. Therefore, the C detected in some of the films, could be due to contamination from the

microscope's chamber since all the films analyzed in this study were not pre-coated with C or a metal.

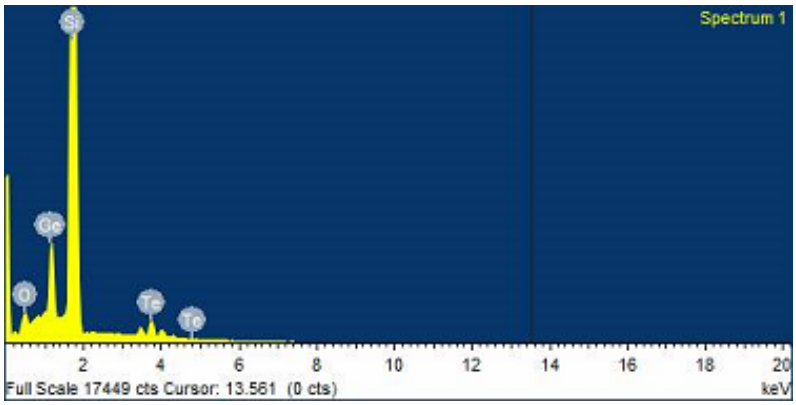

Figure 4.6: EDS spectrum and of $a-$GeTe film with a thickness of 30.7 nm. An EHT of 10 kV was used.

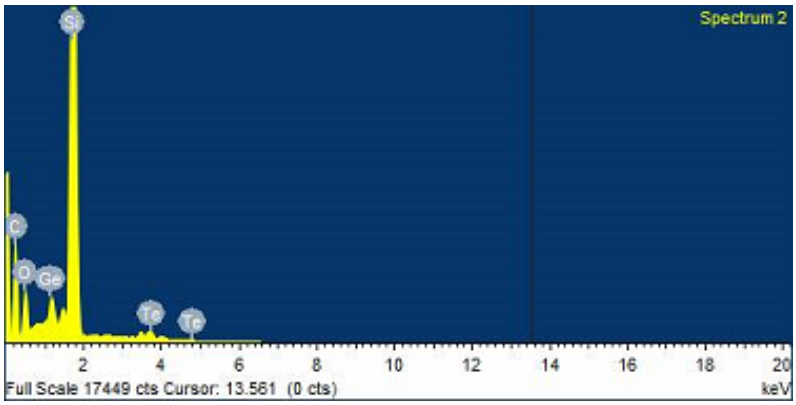

Figure 4.7: EDS spectrum of a 30.7 nm thick $c-$GeTe film annealed at 230°. The image was taken with an EHT of 10 kV.

FESEM measurements were made in order to investigate the surface morphology of the films. However, due to contamination and oxidation on the surface of the films, the morphology could not be studied. This was the case for both $Ge_2Sb_2Te_5$ and GeTe films. Therefore, cross-sectional images were taken to check uniformity in the thickness of the films. As it can be seen in Figure 4.8, the annealed $Ge_2Sb_2Te_5$ film shows that the film has a variation of about 3 % in the thickness. This was also observed for all the annealed films of GeTe with different thicknesses. A number of factors such as the deposition and annealing parameters could be the reason behind this however, this must be investigated further for more clarity.

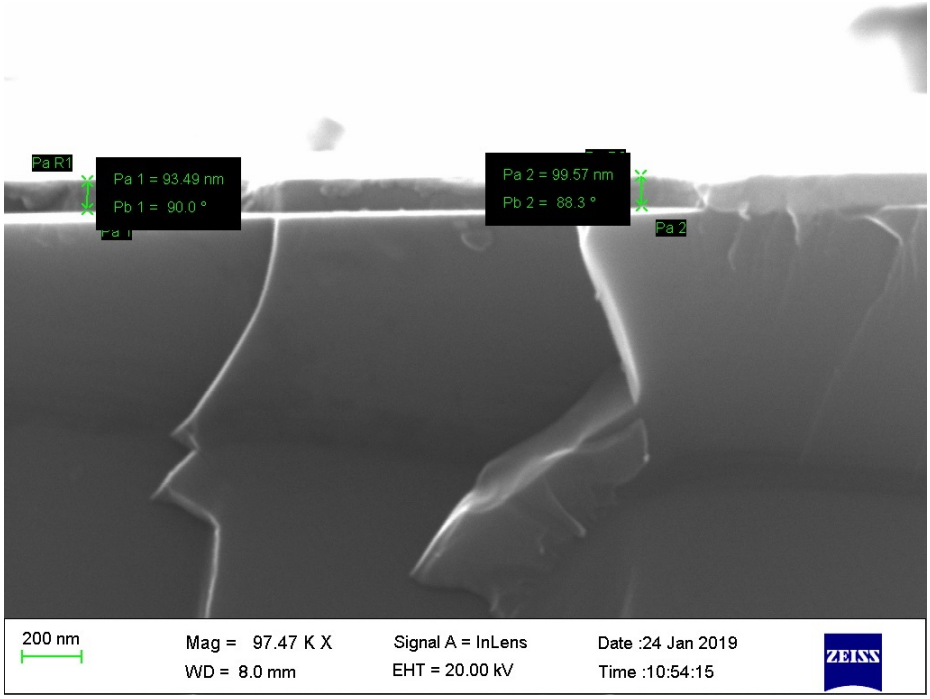

Figure 4.8: FESEM cross-sectional image of a $Ge_2Sb_2Te_5$ sample annealed at 200°C. The image shows that the film's thickness is not uniform.

4.3 Mass Density and Thickness Determination by X-Ray Reflectivity

Figure 4.9 shows the measured XRR patterns of $a-Ge_2Sb_2Te_5$, $c-Ge_2Sb_2Te_5$, and $h-Ge_2Sb_2Te_5$, respectively. The difference between the three structural phases is shown in the inset or zoomed-in region. This part of the graph shows the extent of the 2θ angle depicting the total external reflection, up to the critical angle, θ_c, which is related to the density, ρ, of the films. Below θ_c, the incoming X-rays are reflected, and at incident angles equal to θ_c, the beam propagate along the surface of the film. It is only when the incident angle is greater than θ_c, that the X-rays start to penetrate the film by refraction [63]. Since θ_c precedes the first fringe or oscillation, then it is evident that θ_c in $a-Ge_2Sb_2Te_5$, $c-Ge_2Sb_2Te_5$ and $h-Ge_2Sb_2Te_5$ occurs at 0.748°, 0.751° and 0.762°, respectively. Hence this reveals that the hexagonal phase has a higher density, followed by the cubic phase, and the amorphous phase (details of the values are discussed below). The figure also shows that the oscillations in the XRR pattern of the cubic phase is rapidly decreasing in an exponential manner. This is indicative of surface roughness induced by possible oxidation (that is, by the presence of the GeO_2 layer).

Figure 4.10 shows the corresponding simulated XRR patterns fitted to the measured data for the three phases. From the simulations, mass densities of

5.60, 5.92 and 5.95 g/cm^3 were obtained for $a-Ge_2Sb_2Te_5$, $c-Ge_2Sb_2Te_5$, and $h-Ge_2Sb_2Te_5$, respectively. There is an increase of about 5.7 % in the density between the amorphous and the crystalline phases. The density increase has been attributed to the annihilation of structural defects and long homopolar bonds (0.310 nm) in $a-Ge_2Sb_2Te_5$. The amorphous phase is mainly composed of these homopolar bonds, Ge-Ge, Ge-Sb, Sb-Sb, and a few Te-Te bonds, and has voids accounting for 11.8 % of the total volume [64]. In contrast to $c-Ge_2Sb_2Te_5$, the structure is dominated by shorter heteropolar bonds of Ge-Te (0.284 nm) and Sb-Te (0.2.93 nm) and only 10 % vacancies [64]. Therefore, the structural transition from the amorphous to cubic phase, is accompanied by local order changes from sp^3/p bonds, to p-type bonding around Ge atom. The slight increase in density following cubic to hexagonal phase transition, is associated with the diffusion of Te along the [111] direction, leading to removal of vacancies in the the cubic structure. These results are in agreement with those found by Njoroge *et al.* (2002)even though higher densities of 5.87, 6.27 and 6.39 g/cm^3 were reported for amorphous, cubic and hexagonal phases, respectively [65]. In general, the deposition technique and conditions, as well as film thickness play a role in the film properties [63].

A slight decrease in the thickness of $c-Ge_2Sb_2Te_5$ was observed. This loss of mass was also attributed to the formation of vacancies. The product of the density and thickness gives insight whether evaporation might have occurred or not during the annealing process [2, 65]. A constant value gives confirmation that no evaporation occurred, which in this case is of the order of 2×10^{-5} g/cm^2. Subsequently, as mentioned before, at temperatures around the cubic-hexagonal transition, Ge has a tendency of oxidizing [63]. Hence the slight increase in the hexagonal film thickness can be a result of the GeO_2 layer. This is also supported by the XRR simulations as seen in Table 4.4, which gives a summary of the fitting parameters. The thickness of this oxide layer ranges from $2.7-2.9$ nm and hence the roughness of the $Ge_2Sb_2Te_5$ layers was minimal, $0.4-2.1$ nm. However, it must be noted that the annealing process was done in Ar atmosphere and oxidation would not have occurred in this case.

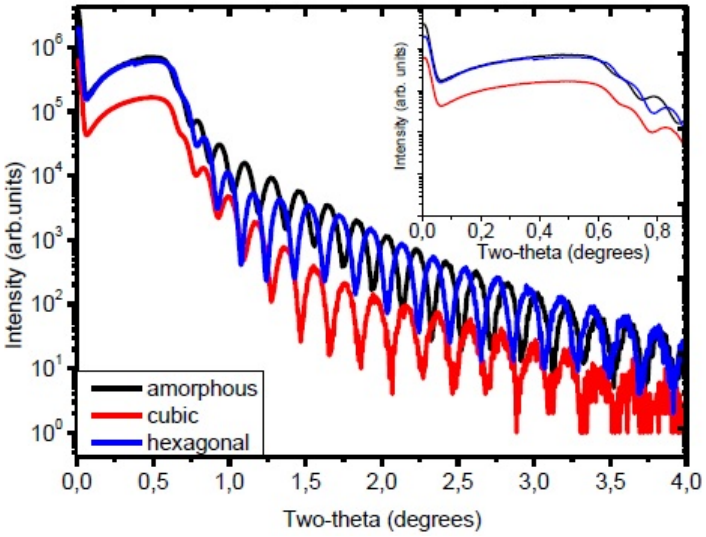

Figure 4.9: The measured XRR pattern of the three phases, the insert graph showing the edge total internal reflectance angle. Higher film density is signified by a higher angles.

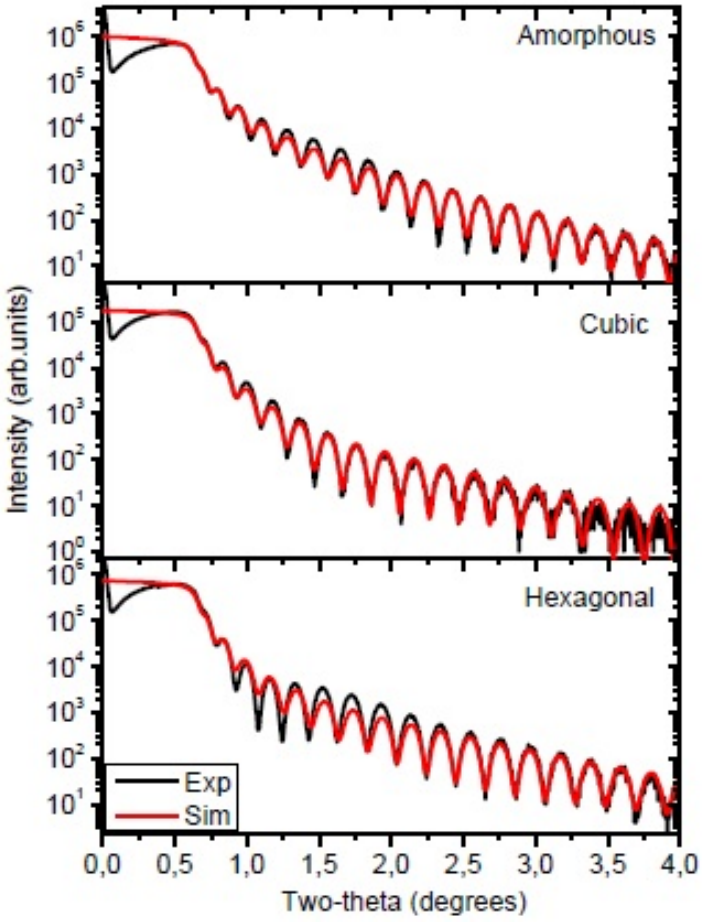

Figure 4.10: XRR pattern of amorphous, cubic and hexagonal $Ge_2Sb_2Te_5$. The red and black curves show the simulated and measured data respectively.

Sample	Density, ρ (g/cm^3)	Thickness, t (nm)
$a-Ge_2Sb_2Te_5$	5.60	43.3
	5.41; 5.87; 5.88 [2], [65], [58]	
$c-Ge_2Sb_2Te_5$	5.92	38.0
	5.76; 6.27; 6.35 [2], [65], [58]	
$h-Ge_2Sb_2Te_5$	5.95	38.4
	6.39 [65]	

Table 4.4: Comparison of the XRR density and thickness measurements done by this study and those reported in literature for the three phases of $Ge_2Sb_2Te_5$.

Figure 4.11 shows the XRR scans of GeTe films sputtered with the same deposition time of 2 minutes. It is evident from the period of the oscillations that the thickness of the crystalline film is less than that of the amorphous film. The as-deposited film has a thickness of 31.5 nm. The film annealed at 230°C shows a huge thickness decrease to 16.0 nm upon crystallization. Taking into account that there are no voids in the structure of $c-$GeTe [64], Welnic and Wuttig (2008) [19] ascribed this to surface crystallization as observed from their atomic force microscopy (AFM) studies. The product, ρt gives almost a constant value of around 1×10^{-5} g/cm^2 for both phases; indicating that the thickness and density change is not due to evaporation [2]. Another reason is that the fit for the crystalline film underestimates the thickness and this explains the disparity. Therefore, the expected thickness decrease of about 8.6 % as reported in most studies was not observed in this work [66].

The critical angle of the $c-$GeTe film is higher (0.871°) than that of $a-$GeTe (0.670°), indicating a larger density in the annealed film. Hence there is a large density increase from 5.49 g/cm^3 for $a-$GeTe film, to 6.91 g/cm^3 for $c-$GeTe. This transition is associated with removal of Ge-Ge and Te-Te homopolar bonds in $a-$GeTe [64]. These bonds have been observed to increase with increasing deposition rate [67]. Thus increase in annealing temperature enhances the formation of Ge-Te bonds which are favored in $c-$GeTe [63]. The density of the amorphous phase is comparable with the one reported by Zhou *et al.* (2015) of 5.46 g/cm^3 for a 31.49 nm thick sample [66] even though a slightly higher value of around 5.60 g/cm^3 was reported in Refs. [58], [68]. The density of the crystalline phase is higher than values found in literature of around 6.06 g/cm^3 [66], [68]. The contributing reasons are the same as those discussed in the previous section of RBS results.

Nevertheless, there seems to be a density dependence on the crystallization temperature of GeTe, as reported by Zhou *et al.* (2015). For instance, a film annealed at 210 °C has a density of 5.93 g/cm^3 compared to 6.07 g/cm^3 for a film annealed at 300°C. Therefore, this shows that the chosen crystallization temperature T_{cryst} (with previously reported values of either 180°C to 300°C [2], [63]) affects the density change. This is also influenced by the possible

oxidation of the surface which in turn influences the nucleation crystallization mechanism [2]. Oxidation and lower T_{cryst} result in lower density values [2], [66]. Even though oxidation affects the material properties, it is a good way (that is by doping with oxygen as seen in Ref.[33]) of suppressing volumetric density changes and this is desirable for scaling PRAM devices and stabilizing the amorphous phase.

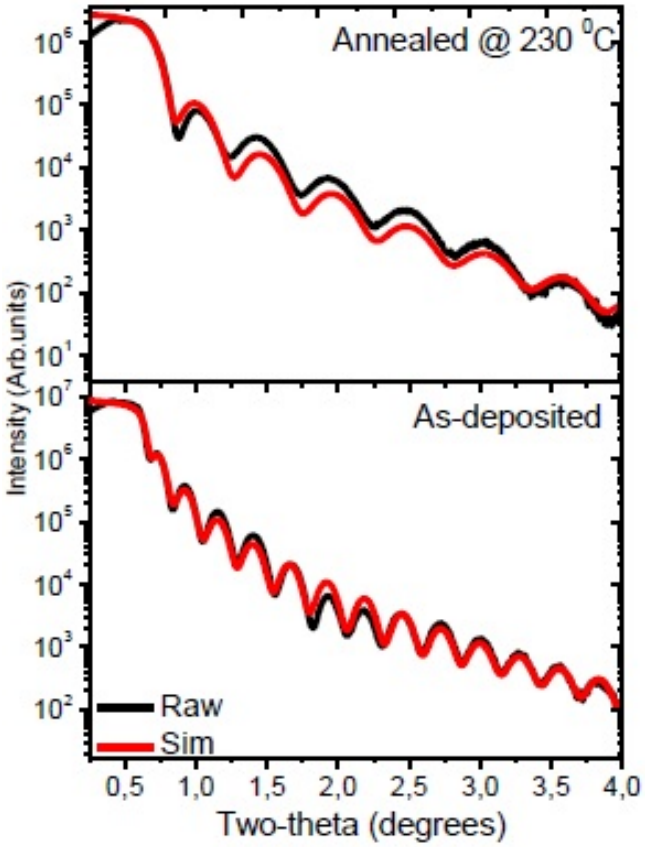

Figure 4.11: XRR measurements of an as-deposited GeTe film, and a crystalline film annealed at 230°C. The films were deposited for 2 min.

4.4 Grazing-Incidence X-ray Diffraction

The two crystalline phases, $c-Ge_2Sb_2Te_5$ and $h-Ge_2Sb_2Te_5$ were obtained by annealing the films at temperatures of 200 °C and 350 °C in an Ar atmosphere for one hour. To assert or verify this, grazing incidence X-ray diffraction (GIXRD) patterns were collected. In general, the number of peaks observable by this technique depends on the grazing incidence angle used. In this study, a fixed grazing incidence angle of 1° was employed. In principle, the peak width is related to disorder present in the material. Hence the two broad peaks seen in the pattern of $a-Ge_2Sb_2Te_5$ (Figure 4.12), are characteristic of the amorphous nature of the as-deposited films. The small peak around 56° may

be an instrumental artefact. It can be seen in the two patterns of the annealed samples that this peak shifts to higher angles and it also diminishes in size as the annealing temperature is increased, as shown in Figure 4.12.

It has been shown by Siegert *et al.* (2014) that increasing the annealing temperature results in a reduction of point defects in the structure of $c-Ge_2Sb_2Te_5$ [69]. Hence this supports our observation. More distinct and narrow peaks start to appear as the annealing temperature is increased. This signifies the crystalline nature of these annealed films. For the sample annealed at a temperature of 200 °C, these peaks are characteristic of a distorted NaCl type of crystal structure, that is, $c-Ge_2Sb_2Te_5$. For the sample annealed at 350 °C, the XRD pattern is characteristic of the hexagonal crystal structure. Peak indexing was done for $c-Ge_2Sb_2Te_5$ and $h-Ge_2Sb_2Te_5$ using powder diffraction data ($04-011-9024$ ICDD 2012 and $04-006-9784$ ICDD 2012) cited in Ref.[70]. One can notice that the XRD patterns of the annealed films consist of broad peaks. It was suspected that this could have been caused by incomplete or suppressed crystallization and possibly, smaller particle sizes. As it can be seen in the upper pattern (of $h-Ge_2Sb_2Te_5$), the first peak is only starting to separate into two but the small peak is not distinct. These two peaks could be the fcc (111) and fcc (200), or hcp (005) and hcp (103), as observed in Ref.[71].

Lee *et al.* (2013) found no hcp or hexagonal peaks in the XRD pattern of a thinner (30 nm) film annealed above 200 °C compared to a thicker (150 nm) film [71]. Thus the authors concluded that the crystallization temperature of the two crystalline phases depends on the annealing time and film thickness. In short, it was realized that the $h-Ge_2Sb_2Te_5$ pattern (in Figure 4.12)is similar to that of the cubic phase as found in Refs.[65], [70]. Moreover, Rietveld refinement could not be performed due to the broad nature of the measured peaks and accurate determination of the lattice parameters, a and c for the two phases could not be performed. Peak broadening could be a sign of disorder in the structures, and stress build-up in the films [2, 65]. Akola and Jones (2012) also cited that in $c-Ge_2Sb_2Te_5$, thermal fluctuations are the cause of this [64]. Nevertheless, previous studies have shown that a is centred around 0.600 nm for $c-Ge_2Sb_2Te_5$ [58, 72, 73]. Njoroge *et al.* (2002) observed that when the annealing temperature of this phase is increased to 260 °C, this results in a decrease in a. For $h-Ge_2Sb_2Te_5$ the a and c lattice parameters were around 0.422 nm and 1.72 nm, respectively [65].

Figure 4.13 shows the GIXRD pattern of two GeTe films deposited for the same time of 2 min. The as-deposited film shows an amorphous structure, since the pattern does not have any pronounced Bragg peaks. Its pattern is dominated by two broad peaks in the range $21°-33°$, and $51°-58°$. For the annealed film, the pattern is dominated by two peaks around 38° and 49°. These are the Bragg peaks due to diffraction from the (202) and (220) planes, revealing that the annealed film has a rhombohedral or distorted NaCl structure (JCPDS No. $47-1079$, [66]). A closer look at the pattern shows that

two other peaks were developing between $25° - 30°$ (021 and 202) and a third one around 60° (042). Thus one can say the film has not fully crystallized due to broadening which causes the peaks to be asymmetrical. Zhou *et al.* (2015) reported five rhombohedral peaks for a film annealed at 300° [66] with the pattern being similar to Figure 4.13. Galca *et al.* (2018) attributed the suppressed crystallization to the formation of Ge or Te oxides on the surface of the GeTe film [63].

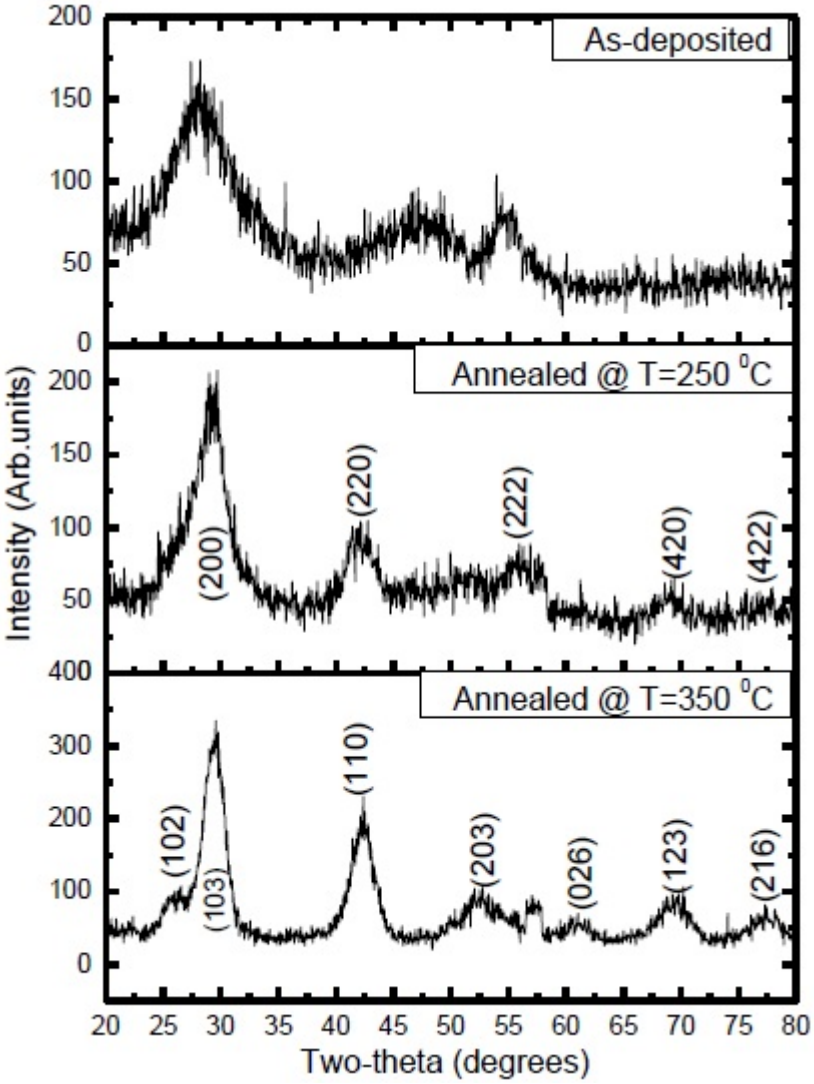

Figure 4.12: GIXRD patterns of $a - Ge_2Sb_2Te_5$, $c - Ge_2Sb_2Te_5$ and $h - Ge_2Sb_2Te_5$ respectively. The measurements were taken at a fixed grazing incidence angle of 1°.

In this study, it was suspected that the annealing time of 1.5 hours for $c -$ GeTe was insufficient to induce complete crystallization. Nevertheless, recent reports have shown that indeed the rhombohedral phase has a lattice parameter of $0.426 - 0.433$ nm with a corresponding diffraction angle of $58.14° - 58.36°$ [74], [75]. As cited in Kagdada *et al.* (2018), the lattice parameter values

in the range of $0.5919 - 0.5986$ nm correspond to the rocksalt cubic phase of GeTe, which is said to be obtainable by annealing for very long periods of time ($300-500$ hours). Again, similarly to the $Ge_2Sb_2Te_5$ alloy, peak indexing could not be performed in this study due to the broadening of the peaks. Incomplete crystallization could be due to combination of factors such as the annealing temperature, time and rate, and deposition parameters chosen in this study.

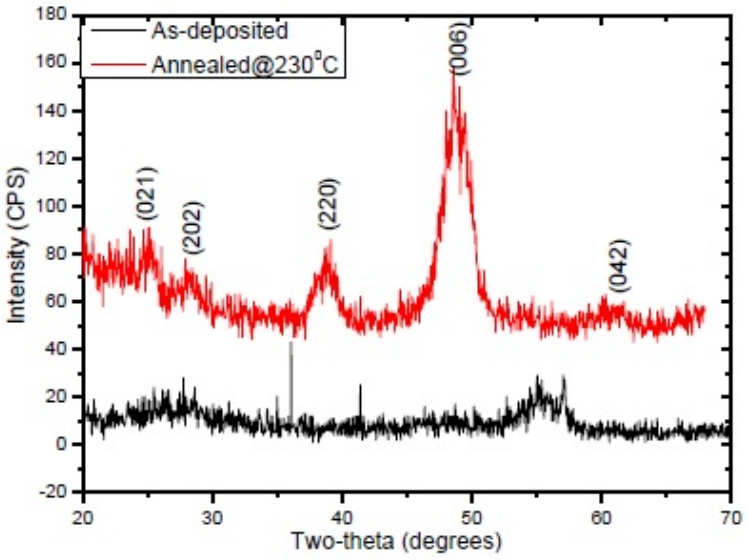

Figure 4.13: GIXRD pattens of the GeTe film deposited for 2 min for the amorphous film and crystalline film annealed at 230 °C. The measurement was taken with a grazing incident angle of 1°.

4.5 Raman Analysis of Optical Phonon Modes

Micro-Raman spectroscopy is a powerful tool for probing vibrational properties of materials; specifically the optical phonon modes. The GeTe alloy is known to exhibit two crystalline phases, namely the low temperature ferroelectric α-GeTe phase, and high temperature paraelectric β-GeTe phase. The latter phase can be described as a rock-salt cubic structure with a space group of $Fm3m$. According to the irreducible group representation theory, the distortion of this highly symmetric cubic structure along the [111] direction leads to a stabilized low symmetry rhombohedral structure (α-GeTe). This structure has a space group of $R3m$ and exists at ambient conditions or at temperatures below the critical temperature, T_c, of 720 K [42], [43].

According to Jeong *et al.* (2017), the face centred cubic structure or β-GeTe phase, has no Raman-active modes [76]. Thus the C_{3V} point group is used to represent the phonon modes at the zone centre of the $R3m$ GeTe [43]. This results in one non-degenerate longitudinal optic (LO) A_1^{LO} mode, and one doubly degenerate E mode. These modes can be measured in the Raman

inelastic scattering configuration of Z(XX)Z-bar, according to selection rules. Figure 4.14 shows the measured Raman spectra of the as-deposited GeTe films and those annealed at 230°C, respectively. The Raman shift of the modes were obtained by performing a peak deconvolution using a Gaussian function.

For the as-deposited films, the two spectra look similar. The minor observable difference is that, with increasing film thickness, there is phonon softening, that is, the frequency of the optical modes decreases. The peak occurring between $100-130\,\mathrm{cm}^{-1}$ is associated with the A_1^{LO}. This peak has been reported to occur at $122\,\mathrm{cm}^{-1}$ and/or $130-140\,\mathrm{cm}^{-1}$ [42, 43]. This mode occurs in both of the as-deposited and the annealed films irrespective of the films thicknesses. Wdowik *et al.* (2014) found that this mode is severely affected by the annealing temperature and hence mode softening was observed upon increasing the annealing temperature [43]. This is seen when comparing the thinner films. The E^{TO} mode occurring at a lower Raman shift of $86\,\mathrm{cm}^{-1}$, was only observed in the 10.9 nm annealed film. This band is due to Ge-Te vibrations [77]. It is noticeable that this peak is halved, and this is due to the filter used to suppress fluorescence. Hence this is the reason for its absence in other films, and it is also the reason why all spectra were measured from $80\,\mathrm{cm}^{-1}$.

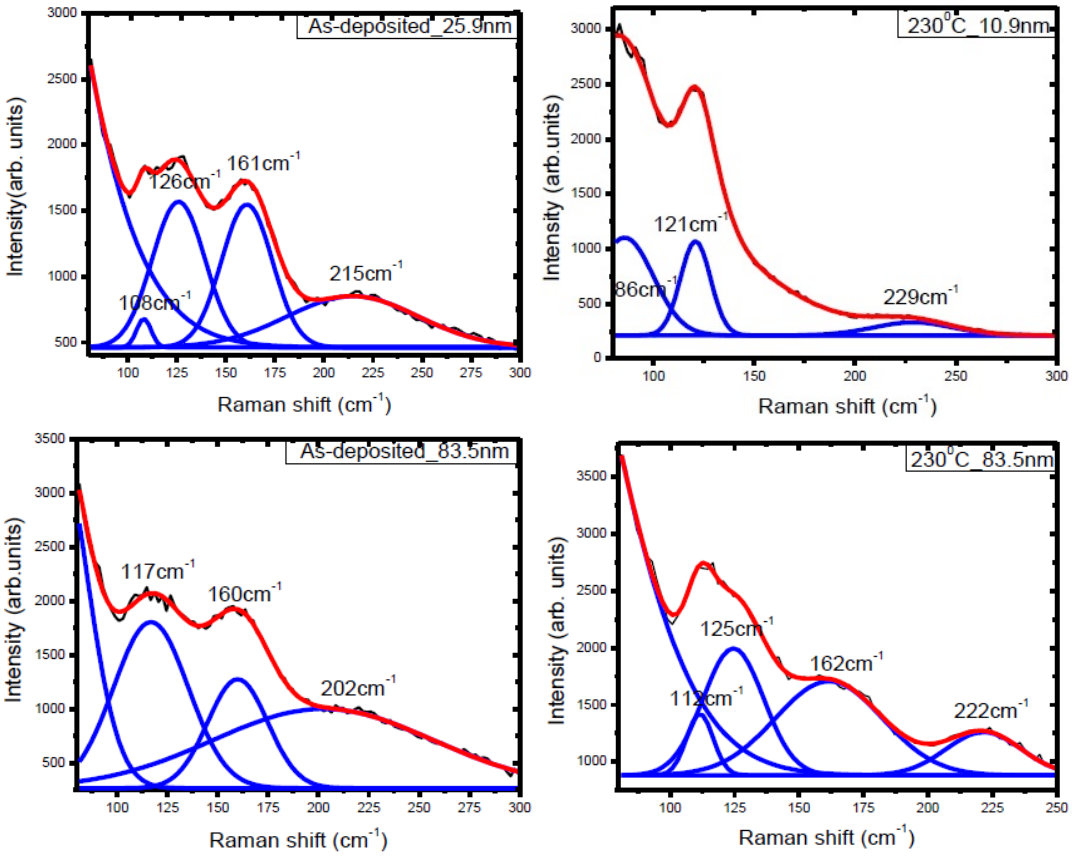

Figure 4.14: Raman spectra of as-deposited GeTe and films annealed at 230 °C.

There are two other bands occurring around $160\,\mathrm{cm}^{-1}$ and $202-229\,\mathrm{cm}^{-1}$. The band at $160\,\mathrm{cm}^{-1}$ is due to vibrations of the $Ge-Te$ bonds [67] and it is present in all films except for the thinner annealed film. Despite this, indeed the spectrum of this film is similar to the one reported in Ref.[78] with only two peaks around $83\,\mathrm{cm}^{-1}$ and $125\,\mathrm{cm}^{-1}$, respectively. This is quite surprising since the $c-$GeTe film was expected to be dominated by these bonds. However, the $86\,\mathrm{cm}^{-1}$ band in the spectrum of the 10.9 nm $c-$GeTe is also due to Ge-Te vibrations. The latter peak ($202-229\,\mathrm{cm}^{-1}$) is broader in the as-deposited films compared to the annealed films. This is indicative of the disordered nature of $a-$GeTe, hence it has been assigned to the Te-Te homopolar bonds which are present only in $a-$GeTe [67]. Its suppression upon annealing could immediately imply elimination of these bonds in the $c-$GeTe. Khoo *et al.* (2016) stated that these peaks evolve with increasing deposition rates and this increases the barrier for nucleation in the crystallization process [67]. One can conclude that in this study, the annealed films have not fully crystallized due to the presence of the $222\,\mathrm{cm}^{-1}$ in the 83.5 nm annealed film. This is supported by the similarity of the spectrum of the 83.5 nm annealed film spectrum with those of the as-deposited films and the GIXRD data.

The interpretation of the Raman spectrum of $Ge_2Sb_2Te_5$ can be understood by comparison with the spectra of the binary alloys, GeTe and Sb_2Te_3. In general, the Raman peaks of the two mentioned binary alloys are more pronounced and intense compared to most of the $(GeTe)_m-(Sb_2Te_3)_n$ (where m,n are integers) ternary alloys, which have broader peaks [79]. Also, the geometry of the structure plays a critical role in analyzing the vibrational properties of most of the Ge-Sb-Te alloys. Figure 4.15 shows the Raman spectrum of the as-deposited $Ge_2Sb_2Te_5$ film in comparison with the spectra of the films annealed at various temperatures. The Raman spectrum of $a-Ge_2Sb_2Te_5$ is dominated by two broad peaks at $127\,\mathrm{cm}^{-1}$ and $155\,\mathrm{cm}^{-1}$. The latter peak is the most widely reported in literature, with its maximum centered around $147-153\,\mathrm{cm}^{-1}$ [70], [79], [80], [81]. This band is associated with the Sb-Te bond vibration in $SbTe_3$ pyramids or edge-sharing $GeTe_4$ tetrahedral vibrational modes [79], [70], [80]. Kozyukhin *et al.* (2013) and Vinod *et al.* (2015) have assigned this band to the A_{1g}^2 mode of Sb_2Te_3 [81], [70]. The broad peak at $127\,\mathrm{cm}^{-1}$ has been reported to appear at $125\,\mathrm{cm}^{-1}$ and $130\,\mathrm{cm}^{-1}$, and is related to A_1 modes of corner-sharing $GeTe_4$ or $GeTe_{4-n}Ge_n$ (where $n=1,2$) tetrahedra [79], [81].

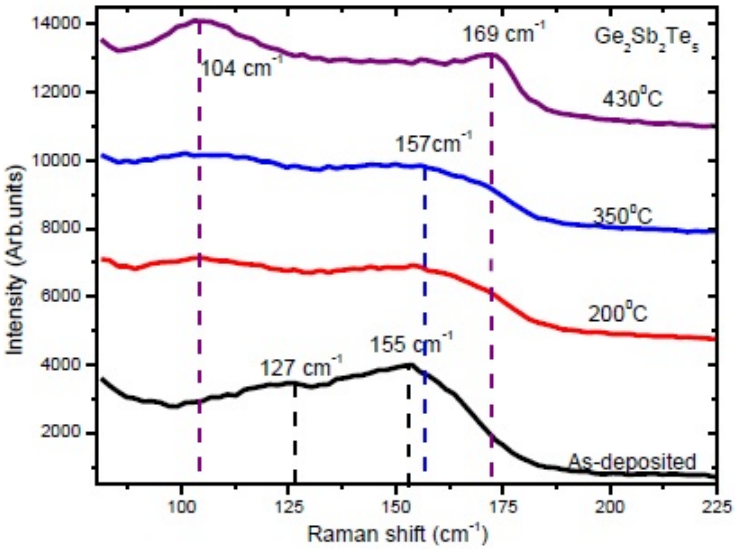

Figure 4.15: Raman spectra of $Ge_2Sb_2Te_5$ films annealed at different temperatures in comparison with the as-deposited sample.

The Raman spectra of the films annealed at 200 °C and 350 °C look similar to the spectrum of the as-deposited film. The minor difference is that the first peak has shifted to a lower Raman shift of 104 cm^{-1}, whilst the second peak has moved to a higher Raman shift of 157 cm^{-1} in the annealed films. This is consistent with the influence of the annealing temperature and this trend is similar to that of Bo *et al.* (2004) [82]. In $c - Ge_2Sb_2Te_5$, the two peaks have been reported at 110cm^{-1} and 160cm^{-1}, respectively [82], although Kozyukhin *et al.* (2013) reported values similar to those of the amorphous phase [81]. The 104 cm^{-1} peak is due to the Ge-Te heteropolar bond in $GeTe_4$ tetrahedra and Sb-Te in pyramidal $SbTe_3$. The band at 157cm^{-1} is due to Sb-Sb vibrations in $(Te_2)Sb - Sb(Te_2)$, $(TeSb)Sb - Sb(Te_2)$ and $(Sb_2)Sb - Sb(SbTe_2)$ units [82], [70], [81]. Therefore, one can say that the optical phonon modes of the cubic $Ge_2Sb_2Te_5$ are similar to those of the amorphous phase. A major change is observed for the film annealed at 430 °C. The peak at 104 cm^{-1} is now pronounced and this could be due to a change in the bond angle as the structure transitions from the cubic to hexagonal phase. The origin of the peak at 169 cm^{-1} is unknown (in terms of vibration modes or bond types) but it is said to be associated with the hexagonal structure for films annealed at 430 °C and it has been reported to appear at 170 cm^{-1} [70], [80].

Chapter 5

Elastic Properties and Lattice Thermal Conductivity by Surface Brillouin Scattering

This chapter presents the elastic properties and the lattice thermal conductivities of $Ge_2Sb_2Te_5$ *and* GeTe *by surface Brillouin scattering (SBS). This technique is crucial for fulfilling the main aim of this study, which is to correlate the elastic and thermal properties of* $Ge_2Sb_2Te_5$ *and* GeTe. *The first section starts with the direct measurement of surface acoustic wave frequencies, followed by the determination of the elastic constants of the two alloys. The two independent elastic constants are then used to calculate other engineering moduli and the velocities of the longitudinal and transverse acoustic modes. Lastly, Cahill's Model is used to calculate the minimum lattice thermal conductivities of the structural phases of the two alloys.*

5.1 Surface Acoustic Modes

5.1.1 $Ge_2Sb_2Te_5$ Thin Films

It was shown from the GIXRD measurements that indeed thermal annealing does induce a phase transition. Here, this is confirmed by studying the influence of laser heating on the RSAW. This was achieved by investigating how the frequency shift of the RSAW changes with varying laser power. A 50 nm as-deposited sample was measured at a fixed incident angle of 70°. The absorbed power was in the range of $32 - 309$ mW and it was determined from the difference between the incident and attenuated beam powers. This difference was more than 56 %; thus showing a moderate power loss. The amount of laser power needed to induce the amorphous to cubic phase transition was

only 32 mW. A change of 0.416 GHz in the RSAW between the two phases was observed. The film remains in the cubic phase for laser powers in the range of $51 - 198$ mW. In this range, the frequency shift of the RSAW remains as 9.672 GHz, hence showing no structural or phase change. A laser power of 246 mW is sufficient to attain another transition to the hexagonal phase as seen in Figure 5.1.

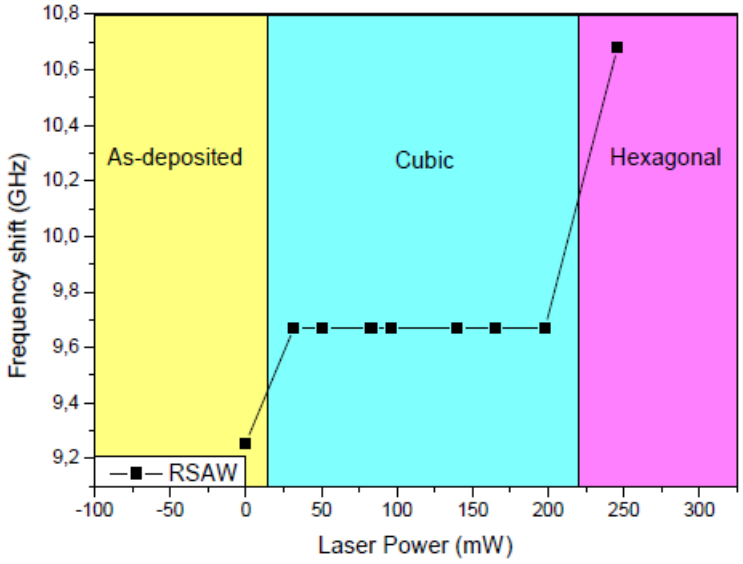

Figure 5.1: The graph shows a change in the frequency shift of the RSAW with varying laser power; this was done to induce the amorphous-cubic, and cubic-hexagonal transitions.

Generally, the number of surface acoustic modes that have been measured are dependent on the film thickness and the incident angle. For instance, only two surface acoustic modes have been measured for the 50 nm films. These are the RSAW and the first Sezawa wave (SW1). As the film thickness is increased from 100 to 500 nm, in addition to the RSAW and (SW1), more Sezawa modes (SW2, SW3,...) start to propagate on the surface. This immediately reveals that the surface ripple mechanism dominates the scattering of SAWs in $Ge_2Sb_2Te_5$, and hence the films are opaque. This can be seen in Figure 5.2 where the as-deposited films with various thicknesses have been measured at 70°. Also Figure 5.3 shows how the incidence angle affects the number of modes. Herein, upon increasing the incident angle from $40 - 70°$ more modes start to develop. This applies to all three phases of $Ge_2Sb_2Te_5$.

Another factor that seems to affect the number of modes propagating in the film is the crystalline phase or order. For a particular angle of incidence, fewer peaks or fewer acoustic modes (specifically, Sezawa waves) were detected as more crystal-order of the $Ge_2Sb_2Te_5$ films was probed. This was apparent in the hexagonal phase compared to the cubic and amorphous phases, as can be seen in Figure 5.4. This applies to all the film thicknesses that were showed.

It must be mentioned that the accumulation time of the SBS spectrum does sometimes affect the number of modes. For opaque and low scattering materials, one will normally observe fewer acoustic modes if the acquisition time is short. Thus all of the spectra in this study were measured for a period of $12 - 24$ hours. Next, we discuss how the incident angle and the crystalline order affect the frequency shift of the modes.

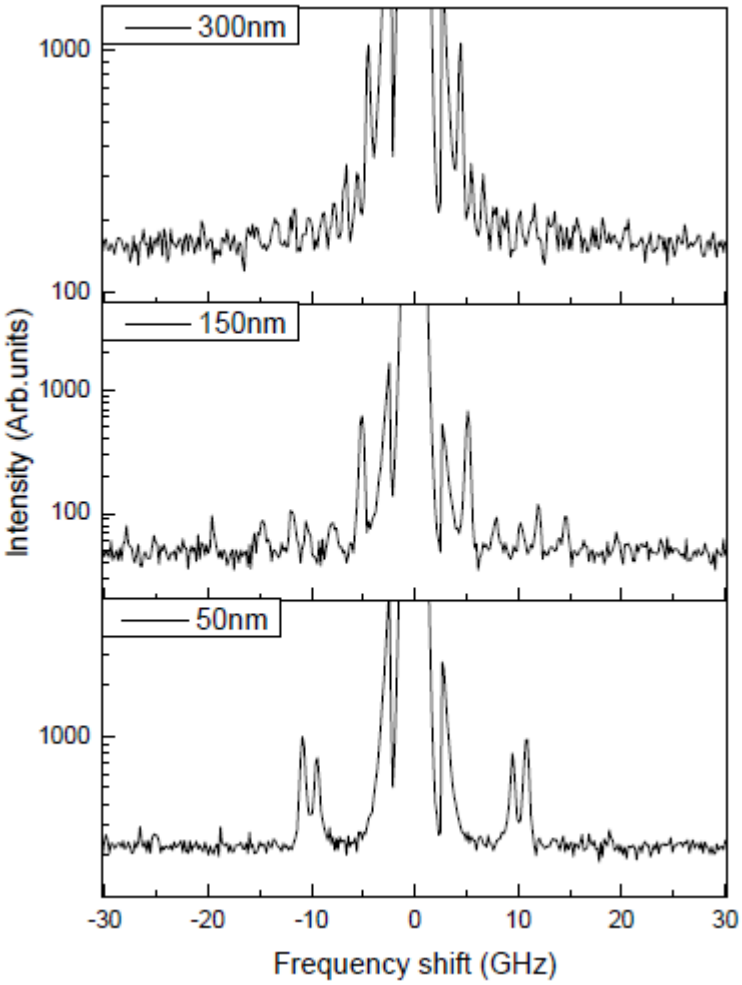

Figure 5.2: The SBS spectra displayed indicate how increasing the film thickness probes the development of more frequency modes. The measurements were done on amorphous samples at an incident angle of 70° for various film thicknesses of 50, 150 and 300 nm.

For a chosen film thickness, an increase in the incident angle results in a frequency shift of the modes to higher values. The RSAW was chosen to illustrate this as seen in Figure 5.3. Moreover, it should be noted that the Sezawa modes also move to higher frequency shifts as the incident angle is increased. The RSAW peak shifts more to higher frequencies as the incident angle is increased. This applies to all three phases of $Ge_2Sb_2Te_5$. To demonstrate the influence of the crystalline phase, the film thickness and the angle

of incidence were fixed at 150 nm and 60°. Figure 5.4 is representative of how the frequency shift varies with crystalline order; the highlighted peak is the RSAW. The frequency increases from 5.095 to 5.633 GHz for $a-Ge_2Sb_2Te_5$ and $c-Ge_2Sb_2Te_5$, then to 6.068 GHz for $h-Ge_2Sb_2Te_5$. The change in frequency shift is smaller between $c-Ge_2Sb_2Te_5$ and $h-Ge_2Sb_2Te_5$, thus showing a slight increase in phonon scattering in the resonantly bonded phases. This increase in the frequency shift of the RSAW represents acoustic hardening of the alloy after structural transitions. This shall be confirmed in the next section.

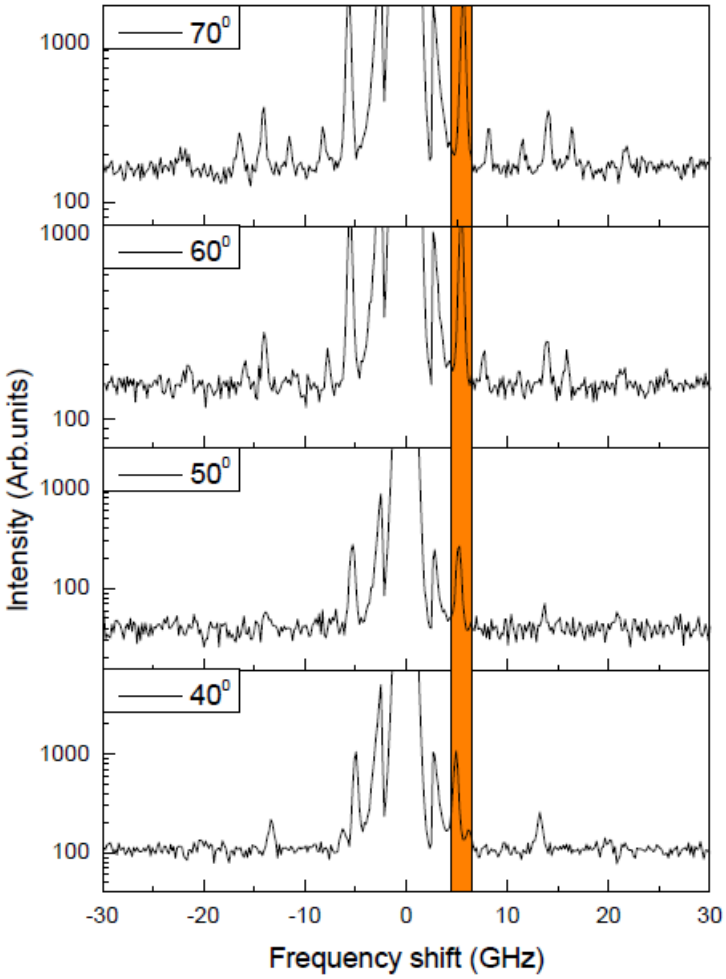

Figure 5.3: The SBS spectra illustrates the variation of the acoustic modes with the incident angle, (the RSAW is highlighted in the orange box). The SBS spectra were measured on 100 nm amorphous films at incident angles of $40-70°$. The sharp dips before the RSAW peak(s) are instrumental artefacts.

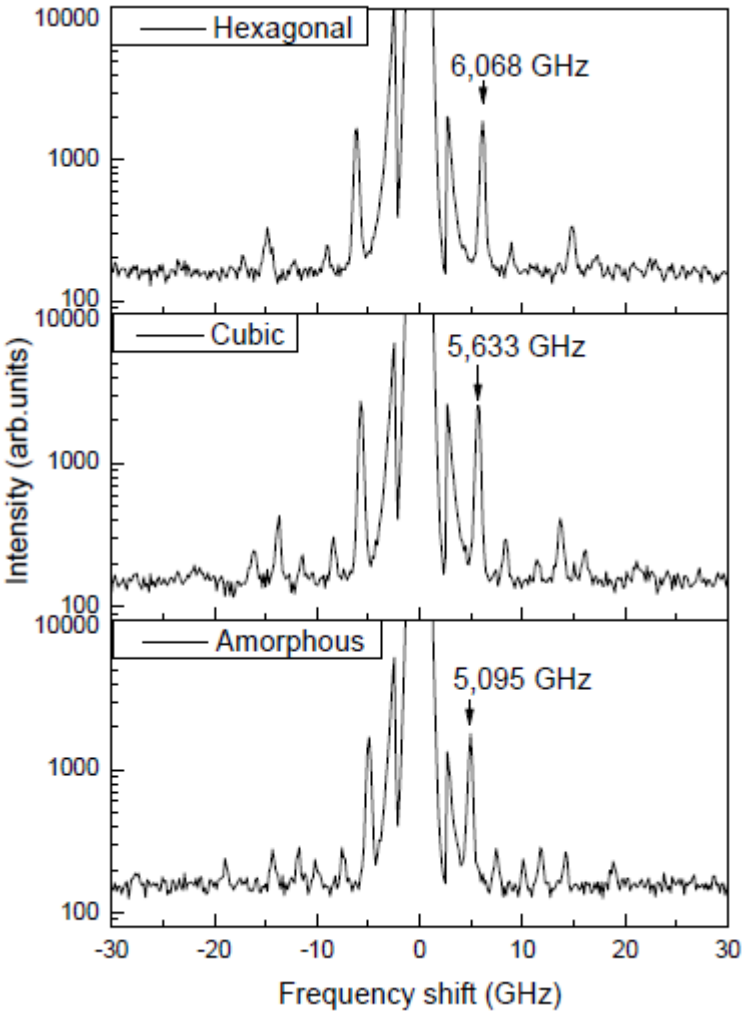

Figure 5.4: The variation of the RSAW frequency shift with structural changes. The number of modes measured are dependent on the crystalline phase of the films. The SBS spectra were measured on 150 nm films at a fixed incident angle of 60°.

5.1.2 GeTe Thin Films

The analysis of SBS measurements shows that the surface ripple mechanism dominates the inelastic scattering of the surface acoustic waves in amorphous GeTe as well as the annealed films. Figure 5.5 shows the SBS spectra of the as-deposited GeTe films measured at $\theta = 70°$ with $0.6992 \leq k_{||}d \leq 6.659$ and corresponding thicknesses in the range of $100\,\text{nm} \leq d \leq 500\,\text{nm}$. The SBS spectra are dominated by the Rayleigh surface acoustic wave (RSAW) and several Sezawa waves (SWs), which show a strong dependence on the film thickness. This variation in film thickness results in the RSAW shifting to lower frequencies. This is indicative of acoustic softening and it was observed for all thickness studied except for the 150 nm-thick sample. This could be due

to a shorter acquisition time of 8 hours, with the rest of the samples measured for 12 hours. Additionally, an increase in frequency shift was observed as the incident angle was increased.

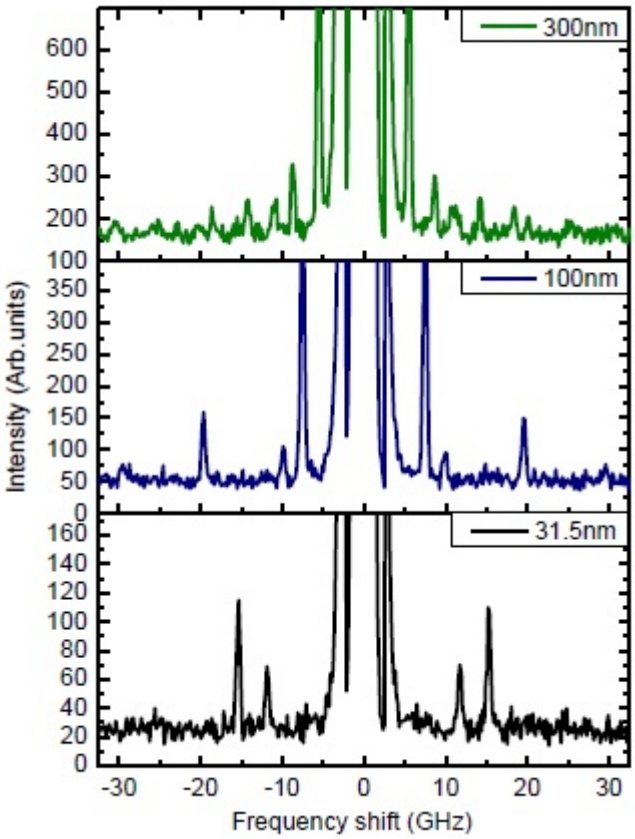

Figure 5.5: SBS spectra of as-deposited GeTe films measured at 70° with $0.6991 \leq k_{||}d \leq 6.659$.

Figure 5.6 shows the effect of varying the incident angle on the frequency shift and the number of detected modes. This is for the films annealed at 230°C. There was no observable trend in the change in frequency shift with thickness variation. This causes some of the experimental data points in the phonon velocity dispersion curve to be scattered. However, this was compensated by changing the incident angle for each film thickness. Thus the frequency shift increases as the incident angle is increased, which implies acoustic stiffening. As observed with the as-deposited samples, this also causes more acoustic modes to propagate on the surface of the films. It must be mentioned that there are various errors that could arise during SBS measurements. One of it is the instrumental error due to the chosen mirror spacing of 4 mm. Its associated error is 2×10^{-6} m and leads to error in the frequency shift of around 0.05 % [6]. Also, since the observed peaks (as well as the ghost peaks) are not always shifted by the same frequency on the Stokes and anti-Stokes sides, their separation results in an overall error of $0.2 - 0.3$ % [6]. Other instrumental errors are low signal to noise ratios which can hide the low intensity

Sezawa modes in the background. However, this uncertainty can be surpassed by repeating the optimization of the elastic peak in both reflection and transmission mode of the TFPI, and by performing a theoretical simulation of the SBS spectrum and comparing it to the measured one [32].

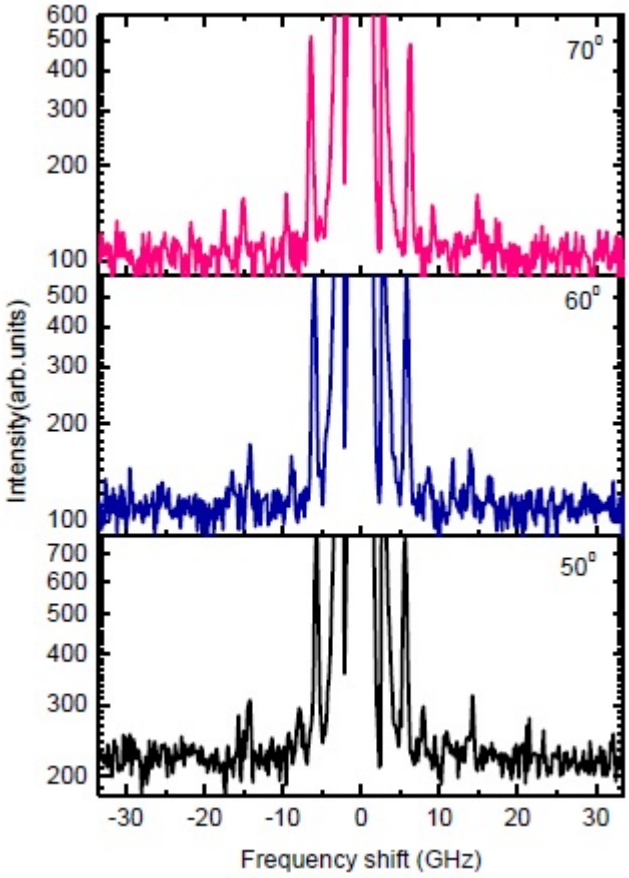

Figure 5.6: SBS spectra of a 200 nm-thick GeTe film annealed at 230°C. This figure illustrates the effect of a variation of the incident angle on the frequency shift and the number of observed modes.

5.2 Isotropic Elastic Properties

5.2.1 $Ge_2Sb_2Te_5$ Thin Films

Surface acoustic excitations allow the determination of the elastic constants of materials. These are fundamentally important in determining engineering moduli such as the Bulk, Shear and Young Moduli and the Poisson ratio. One way of determining the elastic constants is from the phonon-velocity dispersion curve. Herein, the phase velocities of the surface acoustic waves are calculated using the frequency shift or peak position in the SBS curves. This is possible when not only the film thickness is varied, but θ as well. Then the velocities

are plotted against the product of the wave vector, $k_{||}$, parallel to the surface of the material and the film thickness d, that is, $k_{||}d$. Different values of $k_{||}$ were obtained by changing θ in a backscattering geometry as well as d. The elastic constants were extracted from the velocity dispersion curve using the elastodynamic Green's function method, and the least square fitting procedure given by

$$\chi^2 = \sum_{i=1}^{n} \frac{(v_i^{meas} - v_i^{cal})^2}{\sigma_i^2}, \tag{5.1}$$

where v_i^{cal} are the velocities calculated from the surface elastodynamic Green's function method, v_i^{meas} are the velocities measured from SBS measurements (that is, from the velocity dispersion curve), and σ_i are the standard deviations pertaining to the measured data [7]. The surface elastodynamic Green's function method yields only two isotropic or effective elastic constants, C_{11} and C_{44}. The fitting also requires a knowledge of the mass-density of the films, which was determined independently by XRR.

Figure 5.7 shows the phonon velocity dispersion curves of $a - Ge_2Sb_2Te_5$. A number of SBS measurements (not shown in the previous subsection) that were carried out for films with thickness of $50 - 500$ nm and incident angles in the range $40 - 70°$ are needed to acquire this plot. The quality of the fit is dependent on the numerical simulation of the elastic constant values, as well as the density of the material. The density used of 5.60 g/cm^3 was obtained from XRR measurements of the as-deposited sample. As a reminder, for a cubic isotropic material, there are only two independent elastic constants to be determined, C_{11} and C_{44}. The third elastic constant, C_{12}, can be obtained from the Cauchy relation, $C_{12} = C_{11} - 2C_{44}$. The errors in the elastic constants follow from those of the peak positions which were discussed previously. However, the uncertainty of other parameters such as the incident angle, laser wavelength and others, must be known [83]. Also, the resulting errors in the elastic moduli were determined for a transparent medium, and thus in this case the errors in the optical properties such as the index of refraction must be taken into account as well. Therefore the estimated errors in the elastic constants and engineering moduli are in the range $0.3 - 1.5\%$ and around 4.6% for the Poisson ratio [83].

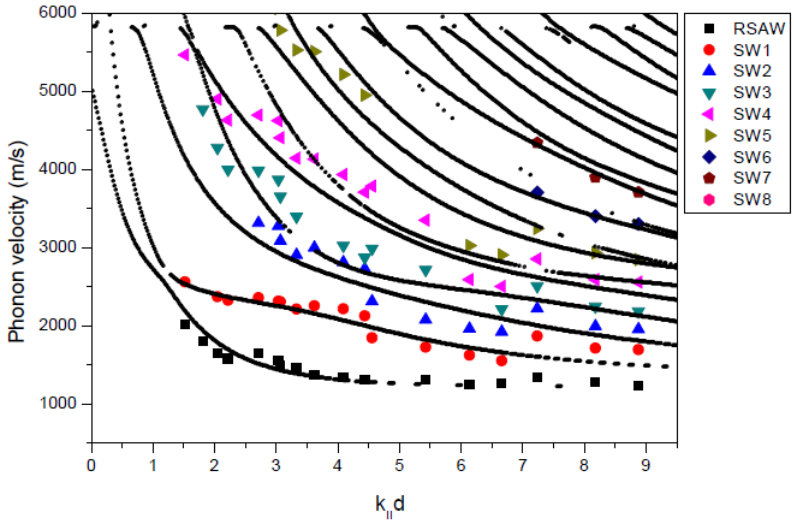

Figure 5.7: Phonon dispersion curves of $a-Ge_2Sb_2Te_5$ for $1.5 \leq k_{||}d \leq 9.0$. The black lines represent the Green's Function fitting method. The variation in the data points is due to inhomogeneity in the films.

The elastic constants of $C_{11} = 37.9$ GPa and $C_{44} = 10.2$ GPa for $a-Ge_2Sb_2Te_5$ were obtained. The shear modulus (G) is equal to the elastic constant C_{44}. Using the Cauchy relation, the calculated value of C_{12} was found to be 17.5 GPa. Other engineering moduli were also obtained from the two independent elastic constants, C_{11} and C_{44}. These are the Young's modulus ($E = 34.4$ GPa), the bulk modulus ($K = 24.3$ GPa), and the Poisson ratio ($\nu = 0.316$). The obtained value for Young's modulus is in agreement within 1.47% with the value of 33.7 GPa [84] compared to the recently reported value of 37.76 ± 3.93 GPa as determined from nanoindentation method [85]. A comparison of other moduli cannot be made due to limited literature data.

Figure 5.8 shows the phonon-velocity dispersion curves of the $c-Ge_2Sb_2Te_5$. For this crystalline phase, C_{11} and C_{44} was 37.0 GPa and 12.0 GPa, respectively. Cecchini *et al.* (2016) reported values of 41.0 and 58.0 GPa for C_{11}, 8.00 and 12.0 GPa for C_{44} from XRD residual stress and density functional theory (DFT) [86]. The C_{44} obtained in this study is in agreement with the DFT value. For the C_{11} value, there is a difference of 9.8 % between this work and the one determined from XRD methods. The calculated C_{12} value of 13.0 GPa was found. The shear modulus $G = C_{44}$, differs significantly from the reported values of 7.00 and 8.00 GPa [86]. However, one should note that in general, the direct local density approximation (LDA) method tends to underestimate material's properties; in this case, C_{12}. Hence one should take precaution in comparing experimental and theoretical results.

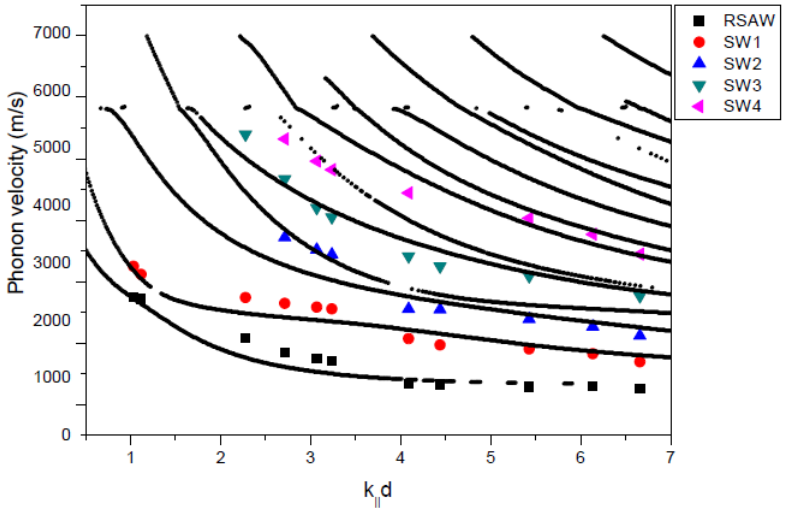

Figure 5.8: Phonon dispersion curves of $c - Ge_2Sb_2Te_5$ for $1.0 \leq k_{||}d \leq 7.0$.

Other elastic properties that have been determined for $c - Ge_2Sb_2Te_5$ from the above equations are $E = 41.8$ GPa, $K = 21.0$ GPa and $\nu = 0.260$. The Young's modulus value falls within the range of $31 - 56$ GPa as determined from the DFT-LDA scheme [86]. There is a good correlation between the values of the bulk modulus determined from this study and by Cecchini *et al.* (2016), of 20 GPa. Other values of the bulk modulus that have been reported as determined using XRD range from $39 - 41$ GPa, whereas K by DFT-LDA range from $25 - 55.9$ GPa. Last but not least, the Poisson ratio of 0.260 is similar to 0.255 for $GeSb_2Te_4$ [87], which is closely related to $Ge_2Sb_2Te_5$. It has been argued that since these materials belong to the same homologous series, $(GeTe)_m(Sb_2Te_3)_n$, they should have similar properties. However, the elastic properties reported in [87] do not support the above statement.

Figure 5.9 shows the dispersion curves of $h - Ge_Sb_2Te_5$ with $k_{||}d$ in the range of $0.8 - 11.5$. Simulation with the Green's function method resulted in $C_{11} = 47.0$ GPa and $C_{44} = 16.5$ GPa. Thus one can see that there is a progressive stiffening for the phase transition from the amorphous to cubic phases, and then to the hexagonal phase. This is also supported by the higher values of $G = C_{44} = 16.5$ and $E = 58.3$ GPa, in contrast to the amorphous and cubic phases. However, one can notice that the only case where this is not true is for the C_{12} value of 14.0 GPa. Even though this value is higher than the cubic phase value of 13.0 GPa, as seen in Table 5.1, the value for the amorphous phase suggests that the amorphous phase is stiffer than the cubic and hexagonal phases. Nevertheless, the elastic properties of $c - Ge_Sb_2Te_5$ and $h - Ge_Sb_2Te_5$, are similar to the corresponding crystalline phases of $GeSb_2Te_4$ [87].

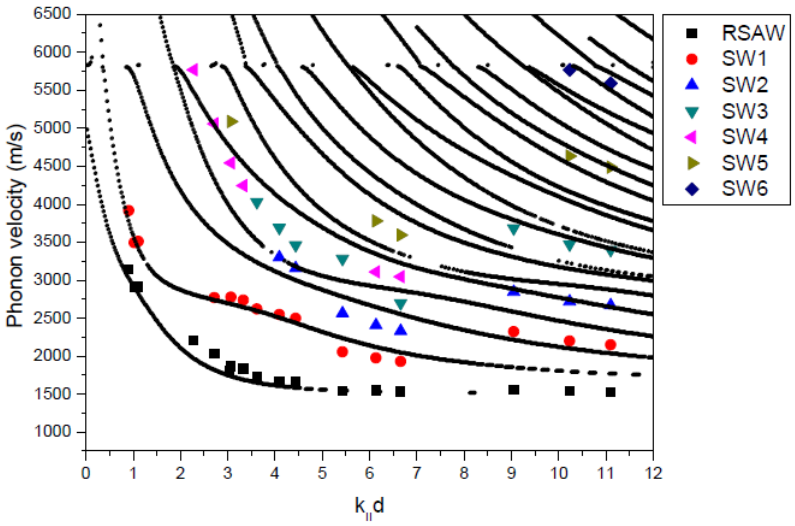

Figure 5.9: Phonon dispersion curves of $h-Ge_2Sb_2Te_5$ for $0.8 \leq k_{||}d \leq 11.5$.

The elastic properties of $GeSb_2Te_4$ shows a linear relation upon phase transitions to the crystalline phases [87]. However, this behaviour is not surprising since Blachowicz *et al.* (2007) pointed out that the phonon modes of the amorphous phase (in $GeSb_2Te_4$ and $Ge_2Sb_2Te_5$) as observed from Raman scattering tend to have higher frequencies compared to the crystalline phase(s) [78, 87]. Nevertheless, it should be noted that only the acoustic phonons as observed by SBS, have a direct influence on the elastic properties, unlike the optical phonons probed by Raman scattering [34]. Thus the lattice thermal conductivity section will provide more insight since this parameter is closely related to the elastic waves (phonons).

Elastic Properties	$Ge_2Sb_2Te_5$ Phase		
	Amorphous	Cubic	Hexagonal
C_{11} (GPa)	37.9	37.0	47.0
		41.0, 58.0 [86]	
C_{12} (GPa)	17.5	13.0	14.0
$C_{44} = G$ (GPa)	10.2	12.0	16.5
		8.00, 12.0 [86]	
E (GPa)	34.4	41.8	58.4
	33.7 [84]	31.0-56.0 [86]	
K (GPa)	24.3	21.0	25.0
ν	0.316	0.260	0.230

Table 5.1: Comparison of the elastic properties obtained in this study and those reported in literature for the three phases of $Ge_2Sb_2Te_5$.

5.2.2 GeTe

Figure 5.10 shows the influence of $k_{||}d$ on the velocity of the surface waves propagating in amorphous GeTe films. Fitting of these curves gave C_{11} = 43.7 GPa and C_{44} = 15.6 GPa, respectively. Again, these are sufficient to determine other elastic moduli or engineering constants as shown in Table 5.2. For instance, C_{44} is equivalent to the shear modulus, G. This value is in agreement with 18 GPa as reported by Ref.[88] for the $R3m$ phase. The Bulk (K) and Young (E) Moduli are 22.9 GPa and 55.5 GPa, respectively. The Cauchy relation gives $C_{12} = C_{11} - 2C_{44}$ = 12.5 GPa. The Poisson ratio of ν = 0.222 was found. The discussion for the amorphous phase is limited due to the insufficient experimental and theoretical literature data.

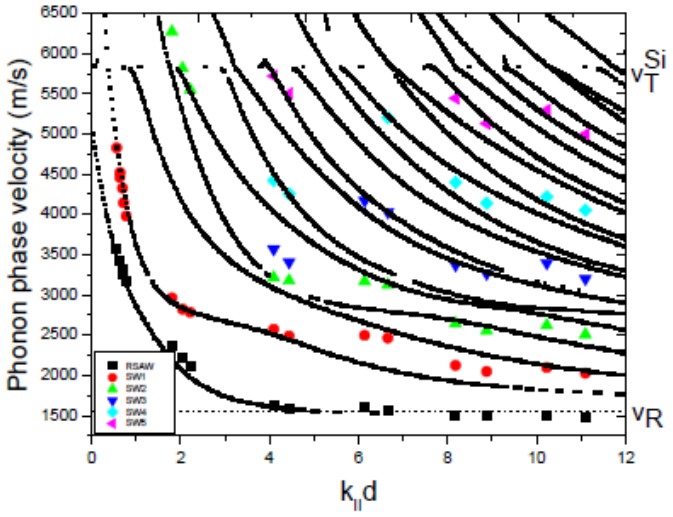

Figure 5.10: Phonon velocity dispersion curves of as-deposited GeTe films for $2.220 \leq k_{||}d \leq 11.10$. The points represent the measured data and the line curves shows the fitting respectively.

Figure 5.11 shows the phonon velocity dispersion curves of the films annealed at 230°C. In comparison to the as-deposited films, fitting revealed evidence of elastic stiffening upon annealing and this was supported the C_{11} value of 49.7 GPa for crystalline phase $c-$GeTe. This was supported further by higher values of C_{12}(22.5 GPa) and of the bulk modulus (K = 31.6 GPa) in comparison with $a-$GeTe. However, the values of the shear ($G = C_{44}$ = 13.6 GPa) and Young (E = 45.9 GPa) moduli, give a different scenario since they are smaller than those of the amorphous phase. This low value of E shows that the rhombohedral crystalline phase is less resistive to compression and this is also supported by the Poisson ratio of 0.312, which is less than 0.5, indicating compressibility [74]. This makes sense since one way of obtaining the high temperature rocksalt cubic phase, $\beta-$GeTe, the rhombohedral phase with a shear distortion along the [111] must be reversed [89]. Hence this explains the lower value of C_{44} for $c-$GeTe than for $a-$GeTe.

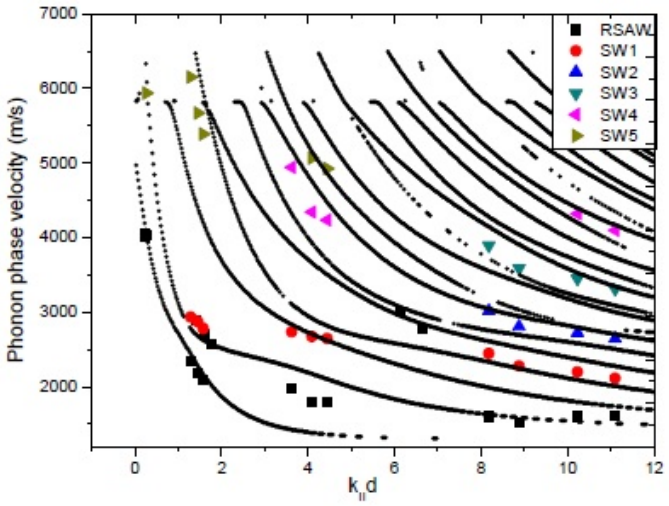

Figure 5.11: Phonon velocity dispersion curves of GeTe films annealed at 230°C.

The reported values of C_{11} (92.0 − 115.7 GPa) and C_{44} (32.09 − 44.02 GPa) are out of the range of the values found in this study of 49.7 GPa and 13.6 GPa, respectively [74], [30], [42]. It must be noted that most theoretical studies reported a shear modulus value which is different from C_{44}. The C_{12} value of 22.5 GPa is comparable with 16.3 GPa, 16.56 GPa, and 19.36 GPa as reported by most studies [74], [30], [42]. Also, the reported bulk modulus values of 36.31 GPa and 44.3 GPa are in agreement with our value of 31.6 GPa [74], [30]. Lastly, Kagdada *et al.* (2018) reported $\nu = 0.19$ and $E = 67.14$ GPa which are not within the range of our values (see Table 5.2) [74].

Elastic property	$a-$GeTe	$c-$GeTe
C_{11} (GPa)	43.7	49.7 92.0-116 [74], [30], [42]
C_{12} (GPa)	12.5	22.5 16.3-19.4 [74], [30], [42]
$C_{44} = G$ (GPa)	15.6	13.6 18.0 [88] 32.1-44.0 [74], [30], [42]
E (GPa)	55.5	45.9 67.1 [74]
K (GPa)	22.9	31.6 36.3 [74], 44.3 [30]
ν	0.222	0.312 0.19 [74]

Table 5.2: Table showing elastic properties obtained in this study and those reported in literature for $a-$GeTe and $c-$GeTe films.

5.3 Determination of the Longitudinal and Transverse Velocities

The velocities of the surface acoustic waves that have been observed in the SBS spectra are crucial for achieving the main aim of this work. Since the films were deposited on a SiO_2/Si substrate, it is vital to know how fast the acoustic modes propagate on the film's surface relative to the substrate. The silicon oxide layer is very thin as it has been seen from the RBS results; therefore particular attention is given to Si(100) as the substrate. The transverse and longitudinal velocities are given by Equation 2.24 in section 2.3. The mass densities determined from section 4.3 become handy in this regard.

The longitudinal velocities of 2557, 2498 and 2955 m/s for $a - Ge_2Sb_2Te_5$, $c - Ge_2Sb_2Te_5$ and $h - Ge_2Sb_2Te_5$ were obtained. It is not surprising that the longitudinal velocity of the amorphous phase is greater than that of the cubic phase. This is because the elastic constant C_{11} showed a similar trend and this may be due to the lower concentration of atoms (atomic density) in the cubic phase as found from RBS experiments. Because of this reason, our value for the cubic phase is significantly lower than 3190m/s as reported in [57]. This large difference exits in the hexagonal phase as well, with values of 3300 and 3360 m/s that were reported before by [57] and [59]. For the amorphous phase, this value determined in this study correlates well with the one measured using picosecond time domain thermoreflectance (TDTR) of 2250 m/s [57].

Transverse velocities of 1325, 1421 and 1648 m/s were found for $a - Ge_2Sb_2Te_5$, $c - Ge_2Sb_2Te_5$ and $h - Ge_2Sb_2Te_5$, respectively. Unlike the longitudinal acoustic modes, it can be seen that the propagation of transverse acoustic modes increases gradually in the three phases. Tsafack *et al.* (2011) reported two velocities for the transverse acoustic branch in the hexagonal phase from density functional perturbation theory (DFPT) calculations [59]. These are the slow and fast transverse velocities of $v_{t1} = 1740$ and $v_{t2} = 2240$ m/s, respectively. There is a good correlation (within 5.3%) between v_{t1} and our value. However, Lyeo *et al.* (2006) assumed that v_T is approximately 60% of v_L, which results in values that are roughly 20% greater than our values for the two crystalline phases. This large difference is due to the fact that the assumption was made based on the behaviour of another material ($CdGeAs_2$), which has different crystal structures from $Ge_2Sb_2Te_5$. Only the amorphous phase value of 1350 m/s is in agreement (within 1.9%) with the one determined in this study of 1325 m/s.

Since the RSAW is the most dominant wave measurable in the SBS spectrum, it makes sense to determine its velocity, v_R. Firstly, the ratio of the Rayleigh velocity to the transverse velocity was determined using Equation 2.20 in section 2.3. The Poisson ratio of 0.316, 0.260 and 0.230 for amorphous, cubic and hexagonal phases of $Ge_2Sb_2Te_5$ give v_R/v_T of 0.930, 0.922 and 0.917 for the three phases in the order given. These values are in an acceptable

range of $[0.874 - 0.955]$ for $\nu < 0.5$ [7]. Therefore, v_R values of 1232 m/s, 1310 m/s and 1511 m/s were calculated for $a-Ge_2Sb_2Te_5$, $c-Ge_2Sb_2Te_5$ and $h-Ge_2Sb_2Te_5$, respectively. These values are indicated in the velocity dispersion curves for each structural phase, and occurs at large $k_{||}d$. For $k_{||}d \longrightarrow 0$, these v_R values of the films approach that of the Si (100) substrate, that is, 4800 m/s. Using the v_R values obtained, it can concluded that this system of $Ge_2Sb_2Te_5$/Si, is representative of a slow-on-fast system due to Si having stiffer elastic properties compared to all phases of $Ge_2Sb_2Te_5$.

The longitudinal velocity as calculated from C_{11} is 2793 m/s and 2682 m/s for $a-$GeTe and $c-$GeTe, respectively. For the transverse velocities of 1669 m/s and 1403 m/s for $a-$GeTe and $c-$GeTe were obtained, respectively. For both velocities, (v_L and v_T), the acoustic phonons propagate much faster in the amorphous films than in the crystalline films. This trend immediately reveals that we expect the lattice thermal conductivity of $c-$GeTe to be smaller than that of $a-$GeTe, as it shall be seen in the next section. Additionally, it was expected that the v_L value for $c-$GeTe to be greater than that of $a-$GeTe due to the higher value of C_{11} in the crystalline phase. However, this is not the case and the plausible explanation is due to the higher density value of 6.91 g/cm^3 compared to 5.49 g/cm^3 for $a-$GeTe. But caution should be taken when interpreting this, as a similar density trend was observed for $Ge_2Sb_2Te_5$. Therefore, there must be an underlying mechanism of phonon propagation in GeTe that is different from $Ge_2Sb_2Te_5$. This will be explained further in the next section.

Bauer Pereira *et al.* (2013) reported an average sound velocity of 1900 m/s as determined form the Debye approximation of the density of phonon states (DPS) [60]. This is comparable with v_T of $a-$GeTe. Again, using the Poisson ratio of 0.222 and 0.312 for $a-$GeTe and $c-$GeTe, the corresponding ratios v_R/v_t of 0.915 and 0.929 were obtained accordingly. Thus the Rayleigh velocity of the films is 1527 m/s, and 1303 m/s for $a-$GeTe and $c-$GeTe, respectively. Again, similarly to $Ge_2Sb_2Te_5$, the two scenarios of $a-$GeTe adhered onto Si and $c-$GeTe supported by Si, represent the case of a slow-on-fast system. Table 5.3 gives a summary of the longitudinal, transverse and Rayleigh velocities determined in this study and those reported in literature for all of the structural phases of $Ge_2Sb_2Te_5$ and GeTe. Next, the correlation between these velocities and the lattice thermal conductivity is presented by means of the Cahill formulation [38] of the Debye model [37].

	v_L (m/s)	v_T (m/s)	v_R (m/s)
$a-Ge_2Sb_2Te_5$	2557	1325	1232
	2250 [57]	1350 [57]	
$c-Ge_2Sb_2Te_5$	2498	1421	1310
	3190 [57]		
$h-Ge_2Sb_2Te_5$	2955	1648	1511
	3300 [57]	1740 [59]	
	3360 [59]	2240 [59]	
$a-GeTe$	2793	1669	1527
$c-GeTe$	2682	1403	1303
		1900 [60]	

Table 5.3: Comparison of the longitudinal, transverse and Rayleigh velocities obtained in this study and those reported in literature for all of the structural phases for $Ge_2Sb_2Te_5$ and GeTe.

5.4 Minimum Lattice Thermal Conductivity

It is known that acoustic phonons store thermal energy [15]. Therefore, the two cannot be separated. Thus the purpose of this section is to correlate the elastic and thermal properties of the two alloys. This has been achieved using the model of minimum thermal conductivity of amorphous materials and disordered crystals [38]. This model assumes that the acoustic phonons contribute largely to the lattice thermal conductivity via their velocities. We obtained κ_{min} of 0.283, 0.287 and 0.361 $Wm^{-1}K^{-1}$ for the amorphous, cubic and hexagonal phases of $Ge_2Sb_2Te_5$, respectively.

For $a-Ge_2Sb_2Te_5$, κ_{min} is comparable with the one reported by Lyeo *et al.* (2006) and Lee *et al.* (2013) of 0.27 $Wm^{-1}K^{-1}$ determined from the same model [57], [71]. For this phase, the model seems to overestimate the measured conductivities of 0.190, 0.240 and 0.250 $Wm^{-1}K^{-1}$, from picosecond time domain thermoreflectance (TDTR) method [57, 71, 90]. There is a slight increase in κ_{min} of 0.287$Wm^{-1}K^{-1}$ for $c-Ge_2Sb_2Te_5$ compared to $a-Ge_2Sb_2Te_5$. This value is in agreement within 2.5% with the measured value 0.280 $Wm^{-1}K^{-1}$ reported in Ref. [90], compared to a value of 0.40 $Wm^{-1}K^{-1}$ [71], which was determined from the same model as this study. Other measured values of 0.450 $Wm^{-1}K^{-1}$ [71] and 0.570 $Wm^{-1}K^{-1}$ [57] do not compare well with the values determined from Cahill's model. In general, the low lattice thermal conductivity in $c-Ge_2Sb_2Te_5$ is attributed to distortions and structural vacancies [57]. This deviation from the reported values has also been observed in $h-Ge_2Sb_2Te_5$.

A value of 0.361 $Wm^{-1}K^{-1}$ for $h-Ge_2Sb_2Te_5$ was obtained in this study and it is comparable with the reported values of 0.420 and 0.430 $Wm^{-1}K^{-1}$ as determined from the same model [71], [59]. These values are smaller than the measured conductivities of 0.460, 1.32 and 1.58 $Wm^{-1}K^{-1}$ for this hexagonal phase [59, 71, 90]. This large increase in the measured lattice thermal conductivity has been associated with the good electrical transport properties of this phase [57]. It must be noted that crystallization leads to semi-metallic behaviour in the two crystalline phases of $Ge_2Sb_2Te_5$. Thus this implies that the electronic contribution to κ, can not be ruled out. Hence it has been shown using the Wiedermann-Franz Law ($\kappa_e = (L_0T)/\rho$, where L_0 is the Lorenz number and ρ is the electrical resistivity) [69], that the electronic contribution to the thermal conductivity (κ_e) is significantly higher in $h-Ge_2Sb_2Te_5$ ($0.870-1.10\,Wm^{-1}K^{-1}$), compared to $0.015-0.07\,Wm^{-1}K^{-1}$ in $c-Ge_2Sb_2Te_5$ [57, 71]. Since the amorphous phase is non-conductive, Lee *et al.* (2013) has shown that $\kappa_e = 0$ for this phase. Also, shorter phonon mean free paths lead to strong phonon scattering, hence relatively higher lattice thermal conductivities in $h-Ge_2Sb_2Te_5$ than the two other phases [69].

It has been shown recently through DFPT calculations [75] that it is possible to determine the lattice thermal conductivity for the two structural stacking models in $h-Ge_2Sb_2Te_5$, namely the Kooi and Petrov structures. Here the κ value has been averaged for a polycrystalline sample with the two structures having a stacking of either Ge/Sb, Ge or Sb vacancies. The values are 0.280 and 0.420 $Wm^{-1}K^{-1}$ for the two structure types with a stacking of Ge/Sb plus Sb vacancies. These values are lower than those simulated for the Ge/Sb plus Ge vacancies stacking of 0.430 and 0.580 $Wm^{-1}K^{-1}$, respectively. The first set of κ values are consistent our value of 0.361 $Wm^{-1}K^{-1}$, since the calculations were done at 300 K. However, it is important to note that elasticity is related to the Debye temperature. The fact that the elastic constants were measured directly by SBS, is a good way of predicting the lower limit of the phonon contribution to the thermal conductivity.

The calculated values of κ_{min} for $a-$GeTe and $c-$GeTe, were found to be 0.381 $Wm^{-1}K^{-1}$ and 0.359 $Wm^{-1}K^{-1}$, respectively. This is a decrease of 5.8% upon crystallization. As mentioned in the previous section, these results are in accordance with the prediction made before using the trend in v_L and v_T, respectively. Both values of κ_{min} for the two phases are in agreement with the theoretical lower limit of 0.300 $Wm^{-1}K^{-1}$ [91]. The Cahill's model predicts a lower bound of 0.180 $Wm^{-1}K^{-1}$ for $a-$GeTe with a composition of Ge : Te = 20 : 80 (cited in Ref.[92]). Nevertheless, it seems as if κ_{min} of $a-$GeTe is centered around $\tilde{0}.2\,Wm^{-1}K^{-1}$ as evidenced from previous studies, that is, $0.190\,Wm^{-1}K^{-1}$ [93], $0.222\pm0.002\,Wm^{-1}K^{-1}$ [69], and $0.230\,Wm^{-1}K^{-1}$ [92]. Lastly, it has been shown from molecular dynamics simulations that, non-propagating phonons in $a-$GeTe, with shorter l_{mfp} (in the order of $0.1-1$ nm), are responsible for this low κ_{lat} (cited in Ref.[92]).

For $c-$GeTe, a comparison with literature data shows that there is a huge

variation in the lattice thermal conductivity, κ_{lat}; with values from 1.30$Wm^{-1}K^{-1}$ [60], 1.98$Wm^{-1}K^{-1}$ [69], 2.60$Wm^{-1}K^{-1}$ [89], 3.08$Wm^{-1}K^{-1}$ [92], 3.10$Wm^{-1}K^{-1}$ [93], to as high as 5.90 $Wm^{-1}K^{-1}$ [94] having been reported. Despite the difference, these values show that indeed there is a significant increase in κ_{lat} upon crystallization, unlike in this study where the opposite was found. Siegert *et al.* (2014) related this large increase to cation sublattice ordering rather than structural vacancies [69]. Our results of low κ_{lat} can be explained by the observations in Ref.[60]. These authors found that $c-$GeTe has a low κ_{lat} of 1.30 $Wm^{-1}K^{-1}$ despite having a higher average sound velocity in compared to other $IV-VI$ thermoelectric materials. This is said to be caused by a combination of Ge and Te vibrations in the transverse acoustic band as observed from the density of phonon states. Other factors that might be contributing to this are a larger anharmonicity and larger number of atoms per unit cell [60].

Another interesting observation is that κ_e contributes more to the total thermal conductivity than κ_{lat}. Reported values of κ_e ranging from 0.730$Wm^{-1}K^{-1}$ [92] and 1.30 $Wm^{-1}K^{-1}$ [60], to as high as 5.70 $Wm^{-1}K^{-1}$ [89], have been calculated from the total κ. In $a-$GeTe the electronic contribution of $\kappa_e = 10^{-}6$ $Wm^{-1}K^{-1}$ is less significant in comparison to $c-$GeTe. Perumal *et al.* (2016), has ascribed this large κ_e contribution to high p-type carrier concentration in $c-$GeTe [89]. Hence one can deduce that the electronic transport properties of $c-$GeTe are as important as its phonon and lattice dynamics in explaining the thermal properties, as these give rise to unique thermoelectric performance [60], [89]. Table 5.4 gives a summary of the minimum lattice thermal conductivity obtained in this work and those reported in literature, for all the structural phases of $Ge_2Sb_2Te_5$ and GeTe.

	κ_{min} ($Wm^{-1}K^{-1}$)	Reference
a − $Ge_2Sb_2Te_5$	0.283	This work
	0.190; 0.270	[57], [71]
	0.240; 0.250	[90], [71]
c − $Ge_2Sb_2Te_5$	0.287	This work
	0.280	[90]
	0.400; 0.450	[71]
	0.570	[57]
h − $Ge_2Sb_2Te_5$	0.361	This work
	0.420; 0.430	[71], [59]
	1.32; 1.58	[90], [71]
a − GeTe	0.381	This work
	0.180; 0.190	Cited in Ref. [92], [93]
	0.222; 0.230	[69], [92]
c − GeTe	0.359	This work
	0.300	[91]
	1.30; 1.98	[60], [69]
	2.60-3.10	[89], [92], [93]

Table 5.4: Table showing the values of the minimum lattice thermal conductivity obtained in this work and those reported in literature, for all the structural phases of $Ge_2Sb_2Te_5$ and GeTe.

Chapter 6

Concluding Remarks and Recommendations

In this study, films of $Ge_2Sb_2Te_5$ and GeTe were deposited by RF magnetron sputtering at room temperature. All as-deposited films have an amorphous structure. The deposition rate of GeTe was found to be higher than that of $Ge_2Sb_2Te_5$, even though similar deposition conditions were used. Crystallization was induced by thermal annealing at different temperatures for the two structural phases of $Ge_2Sb_2Te_5$ and one crystalline phase for GeTe, respectively. Although Bragg peaks are clearly visible in the GIXRD patterns, Rietveld refinement could not be performed and manual calculation of the lattice parameters would be questionable in this regard. Failure to do so is due to peak broadening which could be indicative of the presence of small grains in the films. The morphology of the films could not be observed by FESEM due to the contaminant particles seen on the surface of the films. Stress in the films is attributed to the shift in the Bragg peaks due to strain. Therefore residual stress mapping must be done to study this further.

These two factors lead to peak shifting, which was evident for GeTe annealed films and thus Miller peak indexing would not be credible as well. Thus our chosen temperatures, as well as the total annealing time, could have led to incomplete crystallization. Since crystallization via thermal annealing entails slow cooling of the films to room temperature, thus another factor that might have contributed is the cooling rate. This could not be controlled in this study due to the design of the Carbolite furnace available in our laboratory. Therefore, one recommendation would be to extend the study by Khoo *et al.* 2016 [67] and investigate the effect of annealing time and the variation of annealing temperature on the crystallization process. This can be done both *ex-situ* and *in-situ* by capping the chalcogenide film with a protective layer, such as silicon nitride or a metal. This is important since the crystallization process is a limiting step during programming of the PRAM cell and is crucial for data storage [22].

It was demonstrated through RBS and EDS measurements that the chemical constituents of the $Ge_2Sb_2Te_5$ films for all structural phases are the same as those of the sputtering target. The same is true for crystalline GeTe films, except for as-deposited films. This is because of the presence of Thallium contamination, which its origin remains unclear. The particle-induced X-ray emission (PIXE) detector coupled in the scanning probe microscopy line of the linear accelerator, was not functional during RBS measurements of GeTe, thus additional chemical information could not be obtained. Since the principle of PIXE is similar to that of EDS, EDS measurements were performed to evaluate the chemical composition further, but no Tl was detected. Thus, this can be investigated further using X-ray photo-emission spectroscopy (XPS), and by performing depth profiling studies using RBS. It was also found that the stoichiometry of the films varied slightly upon crystallization and that it differs from those of the targets. This is simply one of the characteristics of sputtered films and it is in-line with what other authors have found previously [57, 65]. From RBS results, the determined atomic densities in all structural phases of $Ge_2Sb_2Te_5$ are in agreement with the reported ones cited in chapter 4. The non-stoichiometric nature of GeTe could be the reason for the discrepancy in the calculated atomic densities in both the as-deposited and annealed films.

XRR measurements were performed for thickness and mass density determination. Both parameters are crucial for simulating the elastic constants of the two alloys. An increasing mass density trend upon crystallization in both $Ge_2Sb_2Te_5$ and GeTe films was observed. This trend is similar to literature observations as discussed in chapter 4. The only downside is the magnitudes of our values, which seem to be underestimated for all structural phases of $Ge_2Sb_2Te_5$ and for $a-$GeTe, and overestimated for $c-$GeTe. This is due to the non-convergence of the fitting to the measured data and it is clearly evident for GeTe films. Due to the limited thickness range that can be probed by XRR, the thickness of films with longer deposition times were determined by FESEM cross-sectional imaging. The inhomogeneity in the films arises from thickness variations due to the thermal history. Additionally, the increase in the rms roughness due to possible oxidation attributed to the high affinity of Ge to O, may lead to significant variations in film thickness. This can however be confirmed from topography mapping by AFM.

Even though the crystalline structures of the annealed films could not be asserted with GIXRD, the fact that Raman active-modes were detected in GeTe annealed films, proves that $c-$GeTe is indeed rhombohedral and not FCC. The Raman spectra of $a-$GeTe are dominated by three vibrational modes, namely the A_1^{LO}, and high frequency Ge-Te and Te-Te vibrations. Upon crystallization, phonon softening in the former mode was observed, whilst phonon hardening was evident in the two latter vibrations. The reduction of the Te-Te band in $c-$GeTe is indicative of elimination of these homopolar bonds, which is good for enhancing the formation of strong and shorter Ge-Te bonds. For $a-Ge_2Sb_2Te_5$, a broad band composed of two peaks at $127\,cm^{-1}$ and $155\,cm^{-1}$, respectively, was imminent. The low Raman shift peak arises from

the A_1 mode of corner-sharing $GeTe_4$ or other related units, as discussed in section 4.5. The high Raman shift peak is due to the A_{1g}^2 mode of the Sb-Te bond vibrations in Sb_2Te_3 or $SbTe_3$ pyramids. Hence the Raman spectrum of $a-Ge_2Sb_2Te_5$ is similar to the corresponding amorphous phases of its binary GeTe and Sb_2Te_3 alloys.

Upon a structural transition to $c-Ge_2Sb_2Te_5$, the broad band starts to separate into two distinct peaks. This is clearly visible upon phase transformation to $h-Ge_2Sb_2Te_5$. Hence for this phase, phonon softening in the first peak was observed due to a lower frequency shift of 104 cm^{-1}. This peak is due to Ge-Te in $GeTe_4$ tetrahedra and Sb-Te in pyramidal $SbTe_3$, respectively. The opposite was observed for the second peak which was shifted to 169 cm^{-1}. This peak is said to be present in the hexagonal phase only. Thus the successful peak identification shows that Raman is a powerful tool for probing optical phonon modes in materials, and these modes immediately reveal information about the chemical bonding of the different structural phases. A low measuring laser power was chosen so not to cause any laser-induced structural transformation during data acquisition. Lastly, we can extend this work by performing *in situ* Raman studies, by measuring the spectra of the as-deposited films as a function of pressure and temperature to investigate the details of phase transitions. Additionally, surface enhanced Raman spectroscopy could assist in improving the intensity of the peaks.

Surface Brillouin scattering spectra of both $Ge_2Sb_2Te_5$ and GeTe films in amorphous and crystalline phases are dominated by the intense Rayleigh surface acoustic waves and several Sezawa waves indicative of the surface ripple scattering mechanism. The propagation of the latter acoustic waves depends on the angle of incidence and film thickness. Upon variation of the two parameters, the RSAW and SWs move to higher frequencies for all structural phases of $Ge_2Sb_2Te_5$. For $a-$GeTe films, acoustic mode softening was observed upon variation of the films thickness. For $c-$GeTe, there is no observable trend upon thickness variation and this is due to inhomogeneity in the films. A change in frequency shift was only observed upon variation of the incident angle. These measurements provided a means for deriving phonon velocity dispersion curves from which the isotropic elastic constants were extracted. This is the most important reason why this method was chosen, to directly determine the elastic properties of the materials in investigation.

The obtained shear modulus values, $G = C_{44}$, suggest progressive elastic stiffening between the three phases of $Ge_2Sb_2Te_5$. This is also supported by the engineering constants calculated from the two independent elastic constants, C_{11} and C_{44}. The only discrepancy present is with the C_{11} and C_{12} values for the amorphous to cubic phase transition. These values imply that $a-Ge_2Sb_2Te_5$ is stiffer than $c-Ge_2Sb_2Te_5$. However, the resultant longitudinal velocity values suggest otherwise. This is because this velocity depends not only on C_{11}, but on the density of the film as well. Hence this could be the reason why the longitudinal velocity (and hence the calculated lattice thermal

conductivity) is higher in the cubic phase than the amorphous phase. As discussed in chapter 4, $c-Ge_2Sb_2Te_5$ consists of heteropolar bonds, which have shorter bond lengths and hence are stronger bonds compared to the homopolar bonds found in $a-Ge_2Sb_2Te_5$. Lastly, comparison of the transverse velocity of the substrate with that of the film, leads to a conclusion that the $Ge_2Sb_2Te_5$/Si is representative of the slow-on-fast substrate configuration. This observation has been found in all structural phases of $Ge_2Sb_2Te_5$.

A similar trend as observed for $Ge_2Sb_2Te_5$ was also seen for the $a-$GeTe to $c-$GeTe phase transition. In this case, the only discrepancy is with the shear and Young Moduli, as well as the Poisson ratio. These parameters suggest that $c-$GeTe is less stiffer than $a-$GeTe. The direct effect of the shear modulus on the transverse velocity is a slow propagation of the acoustic modes in the crystalline phase. This was also the case for C_{11} and the longitudinal velocity. This was unexpected provided that C_{11} was greater in $c-$GeTe than in $a-$GeTe. The above trend is quite peculiar and has revealed a different correlation between the elastic properties and the lattice thermal conductivity of GeTe compared to $Ge_2Sb_2Te_5$. Therefore, the density of the two structural phases are of paramount importance and must not be neglected when analyzing the propagation of the acoustic waves. Nevertheless, the GeTe/Si system is also a good example of the slow-on-fast system for both structural phases.

Since the acoustic velocities are directly proportional to the minimum lattice thermal conductivity according to Cahill's model, the correlation for $Ge_2Sb_2Te_5$ films takes a similar form. Acoustic stiffening upon crystallization leads to fast propagation of surface acoustic waves, resulting in strong phonon scattering and hence an increase in the lattice thermal conductivity. For GeTe, it was found that acoustic softening occurs upon phase transition, and this leads to slow propagation of surface acoustic waves in $c-$GeTe. Thermal fluctuations that occur as the temperature is increased could influence a strong coupling between the optical and acoustic phonons, as well as electron due to the high charge carrier concentration, leading to reduced lattice thermal conductivity. In summary, Cahill's Model is a good way of estimating the lower bound of the lattice thermal conductivity, even though it underestimates this parameter for all phases.

In general, both $Ge_2Sb_2Te_5$ and GeTe exhibit low thermal conductivities in all structural phases. The low thermal conductivity of $a-Ge_2Sb_2Te_5$ encourages good thermal management of PRAM devices during programming. The higher lattice thermal conductivity of $a-$GeTe could be the reason for its instability and hence the drift behaviour observed in PRAM applications. This is bad for data retention and the cyclability of the device. Thus new ways of reducing the lattice thermal conductivity must be employed. The future prospects of PRAM are promising and new applications as well as integration of this novel technology in other existing technologies, are under development [20], [2]. In light of the results of low thermal conductivity as found in this study (which are in agreement with most studies in literature), we intend to

explore the thermoelectric properties of these alloys for thermal management in PRAM devices. It is clear that the elastic properties do have a direct influence on the lattice thermal conductivity. Therefore, DFT calculations of elastic and thermal properties will be performed on chalcogenide superlattice structures, which are candidates for interfacial phase change memory.

Conferences

- M. Baloi, D. Wamwangi, B. Mathe, R.M. Erasmus, M. Madhuku, D.G. Billing, C. Persch and M. Wuttig. Correlation between the elastic and lattice thermal conductivity of GeTe and $Ge_2Sb_2Te_5$ by surface Brillouin scattering. IVC-21, Malmö, Sweden. $1-5$ July 2019. Poster presentation

- M. Baloi, D. Wamwangi, B. Mathe, R.M. Erasmus, M. Madhuku, D.G. Billing, C. Persch and M. Wuttig. Correlation between the elastic and lattice thermal conductivity of GeTe and $Ge_2Sb_2Te_5$ by surface Brillouin scattering. DST/NRF Centre of Excellence in Strong Materials (COE-SM) Student presentation workshop, University of the Witwatersrand, Johannesburg. 21 May 2019. Poster presentation

- M. Baloi, D. Wamwangi, B. Mathe, R.M. Erasmus, M. Madhuku, D.G. Billing, C. Persch and M. Wuttig. Vibrational and thermal properties of GeTe and $Ge_2Sb_2Te_5$ by surface Brillouin scattering. 11^{th} African Laser centre (ALC) student workshop, Wallenberg Research centre, Stellenbosch. 21 November - 02 December 2018. Oral presentation

- M. Baloi, D. Wamwangi, B. Mathe, R.M. Erasmus, M. Madhuku, D.G. Billing, C. Persch and M. Wuttig. Correlation between the elastic and thermal properties of GeTe and $Ge_2Sb_2Te_5$ by surface Brillouin scattering. Johnson Matthey Technology Centre (JMTC) meeting / Academic day, Council of Scientific and Industrial Research (CSIR), Pretoria. 18 November 2018. Oral presentation

- M. Baloi, D. Wamwangi, B. Mathe, R.M. Erasmus, M. Madhuku, D.G. Billing, C. Persch and M. Wuttig. Correlation between the elastic and lattice thermal conductivity of GeTe and $Ge_2Sb_2Te_5$ by surface Brillouin scattering. 9^{th} Cross-faculty postgraduate symposium, University of the Witwatersrand, Johannesburg. $29-30$ October 2018, Flash/Poster presentation

- M. Baloi, D. Wamwangi, B. Mathe, R.M. Erasmus, M. Madhuku, D.G. Billing, C. Persch and M. Wuttig. Elastic and lattice thermal conductivity of $Ge_2Sb_2Te_5$ by surface Brillouin scattering.63^{th} Annual South African Institute of Physics (SAIP) Conference, University of the Free State, Bloemfontein. $25-29$ June 2018. Poster presentation

- M. Baloi, D. Wamwangi, B. Mathe, R.M. Erasmus, M. Madhuku, D.G. Billing, C. Persch and M. Wuttig. Elastic and lattice thermal conductivity of $Ge_2Sb_2Te_5$ by surface Brillouin scattering. DST/NRF Centre of Excellence in Strong Materials (COE-SM) Student presentation workshop, University of the Witwatersrand, Johannesburg. 4 April 2018. Poster presentation

- M. Baloi, D. Wamwangi, B. Mathe, R.M. Erasmus, M. Madhuku, D.G. Billing, C. Persch and M. Wuttig. Correlation between the elastic and

lattice thermal conductivity of GeTe and $Ge_2Sb_2Te_5$ by surface Brillouin scattering. 10^{th} African Laser centre (ALC) student workshop, Wallenberg Research Centre, Stellenbosch. 30 November - 02 December 2017. Oral presentation

Publications

- Co-authored: D. Wamwangi, B. Mathe, M. Baloi, D.G. Billing, C. Persch and M. Wuttig. Elastic properties of chalcogenide based phase change memories by surface Brillouin scattering. Proceedings of the SAIP2017, 2017. ISBN $978 - 0 - 620 - 82077 - 6$.

- In-preparation: M. Baloi, D. Wamwangi, B. Mathe, R.M. Erasmus, M. Madhuku, D.G. Billing, C. Persch and M. Wuttig. Correlation between the elastic and lattice thermal conductivity of amorphous GeTe and $Ge_2Sb_2Te_5$ by surface Brillouin scattering.

- In-preparation: M. Baloi, D. Wamwangi, B. Mathe, R.M. Erasmus, M. Madhuku, D.G. Billing, C. Persch and M. Wuttig. Correlation between the elastic and lattice thermal conductivity of annealed $Ge_2Sb_2Te_5$ films by surface Brillouin scattering.

References

[1] M.J. Miller. Storage class memory: The coming revolution. *URL: https://forwardthinking.pcmag.com/hard-drives/346999-storage-class-memory-the-coming-revolution*, August 2016.

[2] P. Noé, C. Vallée, F. Hippert, F. Fillot, and J-Y. Raty. Phase-change materials for non-volatile memory devices: from technological challenges to materials science issues. *Semiconductor Science and Technology*, 33(1): 013002, 2018.

[3] M. Wuttig and N. Yamada. Phase-change materials for rewriteable data storage. *Nature materials*, 6(11):824, 2007.

[4] D.J. Wouters, R. Waser, and M. Wuttig. Phase-change and redox-based resistive switching memories. *Proceedings of the IEEE*, 103(8):1274–1288, 2015.

[5] H-S. P. Wong, S. Raoux, S. Kim, J. Liang, J.P. Reifenberg, B. Rajendran, M. Asheghi, and K.E. Goodson. Phase change memory. *Proceedings of the IEEE*, 98(12):2201–2227, 2010.

[6] X. Zhang. *Surafce Brillouin scattering studies of bulk materials and thin layers*. PhD thesis, University of the Witwatersrand, 1999.

[7] A.G. Every and J.D. Commins. Surface brillouin scattering. In N. Ida, editor, *Handbook of Advanced Non-Destructive Evaluation*, pages 581–651. Springe International Publishing, 2018.

[8] T.M. Tritt. *Thermal conductivity: theory, properties, and applications*. Springer Science & Business Media, 2005.

[9] W-K. Chu. *Backscattering spectrometry*. Academic Press INC, 1978.

[10] M. Mayer. Rutherford backscattering spectrometry (rbs). In *Workshop on Nuclear Data of Science and Technology: Materials Analysis*, 2003.

[11] Carl Zeiss NTS Limited. Sigma field emission electron microscope instruction manual. *URL http://www.iitk.ac.in/meesa/SEM/SEM-manual.pdf*, 2011.

[12] I. De Wolf. Micro-raman spectroscopy to study local mechanical stress in silicon integrated circuits. *Semiconductor Science Technology*, 11:139–154, 1996.

[13] J.R. Sandercock. High contrast tandem fabry-pérot interferometer tfp-2 hc: Operator manual. *URL: www. tablestable. com/uploads/ckeditor/TFP-1/manual-TFP-1.pdf*, 1701(1.4), 1993.

[14] F. Palombo, C.P. Winlove, R.S. Edginton, E. Green, N. Stone, S. Caponi, M. Madami, and D. Fioretto. Biomechanics of fibrous proteins of the extracellular matrix studied by brillouin scattering. *Journal of The Royal Society Interface*, 11(101):20140739, 2014.

[15] N.W. Ashcroft and N.D. Mermin. *Solid state physics*. Brooks/Cole, Cengage Learning, Belmont, USA, 1976.

[16] C.H. Lam. Storage class memory. In *Solid-State and Integrated Circuit Technology (ICSICT), 2010 10th IEEE International Conference on*, pages 1080–1083. IEEE, 2010.

[17] A. Athmanathan, M. Stanisavljevic, N. Papandreou, H. Pozidis, and E. Eleftheriou. Multilevel-cell phase-change memory: A viable technology. *IEEE Journal on Emerging and Selected Topics in Circuits and Systems*, 6(1):87–100, 2016.

[18] T. Siegrist, P. Merkelbach, and M. Wuttig. Phase change materials: challenges on the path to a universal storage device. *Annu. Rev. Condens. Matter Phys.*, 3(1):215–237, 2012.

[19] W. Wełnic and M. Wuttig. Reversible switching in phase-change materials. *materials today*, 11(6):20–27, 2008.

[20] S. Raoux, F. Xiong, M. Wuttig, and E. Pop. Phase change materials and phase change memory. *MRS bulletin*, 39(8):703–710, 2014.

[21] S.R. Ovshinsky. Reversible electrical switching phenomena in disordered structures. *Physical Review Letters*, 21(20):1450, 1968.

[22] S. Raoux, W. Wełnic, and D. Ielmini. Phase change materials and their application to nonvolatile memories. *Chemical reviews*, 110(1):240–267, 2009.

[23] L. Shi. In S. Raoux and M. Wuttig, editors, *Phase change materials: science and application*, pages 1–428. Springer Science & Business Media, New york, USA, 2009.

[24] T. Matsunaga, N. Yamada, R. Kojima, S. Shamoto, M. Sato, H. Tanida, T. Uruga, S. Kohara, M. Takata, P. Zalden, et al. Phase-change materials: vibrational softening upon crystallization and its impact on thermal properties. *Advanced Functional Materials*, 21(12):2232–2239, 2011.

[25] M.H. Sadd. *Elasticity: theory, applications and numerics*. Academic Press, 2005.

[26] C. Sumanya. *Surafce Brillouin scattering in opaque thin films and bulk materials*. PhD thesis, University of the Witwatersrand, 2012.

[27] I. Mothochi. *Brillouin Light Scattering of Ion-Implanted and Annealed Diamond Surfaces*. PhD thesis, University of the Witwatersrand, 2015.

[28] T. Kundu. Mechanics of elastic waves and ultrasonic nondestructive evaluation. In T. Kundu, editor, *Ultrasonic nondestructive evaluation: engineering and biological material characterization*, pages 3–141. CRC press, 2003.

[29] Y. Itin and F.W. Hehl. The constitutive tensor of linear elasticity: its decompositions, cauchy relations, null lagrangians, and wave propagation. *Journal of Mathematical Physics*, 54(4):042903, 2013.

[30] S. Palaz, H. Koc, A.M. Mamedov, and E. Ozbay. Topological insulators: Electronic band structure and spectroscopy. In *IOP Conf. Series: Materials Science and Technology*, volume 175, page 012004. IOP Publishing, 2017.

[31] A.G. Every. Measurement of the near-surface elastic properties of solids and thin supported films. *Measurement Science and Technology*, 13(5): R21, 2002.

[32] M.G. Beghi, A. G. Every, and P.V. Zinin. Surface brillouin scattering measurement of saw velocities for determining near-surface elastic properties. In T. Kundu, editor, *Ultrasonic nondestructive evaluation: engineering and biological material characterization*, pages 581–651. CRC press, 2003.

[33] X. Zhang, J.D. Comins, A.G. Every, P.R. Stoddart, W. Pang, and T.E. Derry. Surface brillouin scattering study of the surface excitations in amorphous silicon layers produced by ion bombardment. *Physical Review B*, 58(20):13677, 1998.

[34] T. Błachowicz. Brillouin spectroscopy in crystal lattices. *Acoustic and Spin Waves*, pages 102–109, 2003.

[35] C. Kittel et al. *Introduction to solid state physics*, volume 8. Wiley New York, 1976.

[36] K.S. Siegert. *Thermal properties of phase change materials from lattice dynamics to thermoelectricity*. PhD thesis, RWTH Aachen University, 2015.

[37] J. Callaway. Model for lattice thermal conductivity at low temperatures. *Physical Review*, 113(4):1046, 1959.

[38] D.G. Cahill, S.K. Watson, and R.O. Pohl. Lower limit to the thermal conductivity of disordered crystals. *Physical Review B*, 46(10):6131, 1992.

[39] M. Ohring. *Materials science of thin films*. Elsevier, 2001.

[40] K. Seshan. *Handbook of thin film deposition: Processes and technologies*. William Andrew, 2002.

[41] S. Swann. Magnetron sputtering. *Physics in technology*, 19(2):67, 1988.

[42] R. Shaltaf, E. Durgun, J-Y. Raty, Ph. Ghosez, and X. Gonze. Dynamical, dielectric and elastic properties of gete with first-principles density functional theory. *Physical Review B*, 78:205203, 2008.

[43] U.D. Wdowik, K. Parlinski, S. Rols, and T. Chatterji. Soft-phonon mediated structural phase transition in gete. *Physical Review B*, 89:224306, 2014.

[44] W.K. Chu and J.R. Liu. Rutherford backscattering spectrometry: reminiscences and progresses. *Materials chemistry and physics*, 46(2-3):183–188, 1996.

[45] T.L. Alford, L.C. Feldman, and J.W. Mayer. Atomic collisions and backscattering spectrometry. *Fundamentals of Nanoscale Film Analysis*, pages 12–33, 2007.

[46] M.R. Went and M. Vos. Rutherford backscattering using electrons as projectiles: underlying principles and possible applications. *Nuclear Instruments and Methods in Physics Research Section B: Beam Interactions with Materials and Atoms*, 266(6):998–1011, 2008.

[47] M.O. Thompson. Genplot and rump documentation. *URL: http://www. genplot. com/doc/index. htm.[46] JF Ziegler, computer code TRIM, URL http://www. research. ibm. com/ionbeams*, 1996.

[48] Y. Leng. *Materials characterization: introduction to microscopic and spectroscopic methods*. John Wiley & Sons, 2009.

[49] E. Chason and T.M. Mayer. Thin film and surface characterization by specular x-ray reflectivity. *Critical Reviews in Solid State and Material Sciences*, 22(1):1–67, 1997.

[50] S-L. Chang. Thin-film characterization by grazing incidence x-ray diffraction and multiple beam interference. *Journal of Physics and Chemistry of Solids*, 62(9-10):1765–1775, 2001.

[51] G. Bracco and B. Holst. *Surface science techniques*. Springer Science & Business Media, 2013.

[52] D. Simeone, G. Baldinozzi, D. Gosset, S. Le Caer, and J-F. Bérar. Grazing incidence x-ray diffraction for the study of polycrystalline layers. *Thin Solid Films*, 530:9–13, 2013.

[53] Bruker AXS. D8 x-ray diffractometer vol.i. *URL: smse.seu.edu.cn*, I, 2010.

[54] Luis Grave de Peralta. *Thin film characterization by x-ray reflectivity.* PhD thesis, Texas Tech University, 2000.

[55] Horiba Scientific. T64000: Advanced research raman system. *URL: www.horiba.com/fileadmin/uploads/Scientific/Documents/Raman/T64000.pdf*, April 2013.

[56] Quantum Laser Ltd. Torus operating manual. *URL: https://www.laserquantum.com/uploads/files/manuals/cm/r-0158.pdf*, 2.0, "Accessed in September 2018".

[57] H-K. Lyeo, D.G. Cahill, B-S. Lee, J.R. Abelson, M-H. Kwon, K-B. Kim, S.G. Bishop, and B-k. Cheong. Thermal conductivity of phase-change material ge 2 sb 2 te 5. *Applied Physics Letters*, 89(15):151904, 2006.

[58] J. Akola and R.O. Jones. Structural phase transitions on the nanoscale: The crucial pattern in the phase-change materials ge 2 sb 2 te 5 and gete. *Physical Review B*, 76(23):235201, 2007.

[59] T. Tsafack, E. Piccinini, B-S. Lee, E. Pop, and M. Rudan. Electronic, optical and thermal properties of the hexagonal and rocksalt-like ge2sb2te5 chalcogenide from first-principle calculations. *Journal of Applied Physics*, 110(6):063716, 2011.

[60] P. Bauer Pereira, I. Sergueev, S. Gorsse, J. Dadda, E. Müller, and R.P. Hermann. Lattice dynamics and structure of gete, snte and pbte. *physica status solidi (b)*, 250(7):1300–1307, 2013.

[61] J. Akola and R.O. Jones. Density functional study of amorphous, liquid and crystalline ge2sb2te5: homopolar bonds and/or ab alternation? *Journal of Physics: Condensed Matter*, 20(46):465103, 2008.

[62] J. Akola and R.O. Jones. Binary alloys of ge and te: order, voids, and the eutectic composition. *Physical review letters*, 100(20):205502, 2008.

[63] A.C. Galca, F. Sava, I.D. Simandan, C. Bucur, V. Dumitru, C. Porosnicu, C. Mihai, and A. Velea. Structural and optical properties of optimized amorphous gete films for memory applications. *Journal of Non-Crystalline Solids*, 499:1–7, 2018.

[64] J. Akola and R.O. Jones. Amorphous structures of ge/sb/te alloys: Density functional simulations. *physica status solidi (b)*, 249(10):1851–1860, 2012.

[65] W.K. Njoroge, H-W. Wöltgens, and M. Wuttig. Density changes upon crystallization of ge 2 sb 2.04 te 4.74 films. *Journal of Vacuum Science & Technology A: Vacuum, Surfaces, and Films*, 20(1):230–233, 2002.

[66] X. Zhou, W. Dong, H. Zhang, and R.E. Simpson. A zero density change phase change memory material: Gete-o structural characteristics upon crystallisation. *Scientific reports*, 5:11150, 2015.

[67] C.Y. Khoo, H. Liu, W.A. Sasangka, R.I. Made, N. Tamura, M. Kunz, A.S. Budiman, C.L. Gan, and C.V. Thompson. Impact of deposition conditions on the crystallization kinetics of amorphous gete films. *Journal of materials science*, 51(4):1864–1872, 2016.

[68] T. Nonaka, G. Ohbayashi, Y. Toriumi, Y. Mori, and H. Hashimoto. Crystal structure of gete and ge2sb2te5 meta-stable phase. *Thin Solid Films*, 370(1-2):258–261, 2000.

[69] K.S. Siegert, F.R.L Lange, E.R. Sittner, H. Volker, C. Schlockermann, T. Siegrist, and M. Wuttig. Impact of vacancy ordering on thermal transport in crystalline phase-change materials. *Reports on Progress in Physics*, 78(1):013001, 2014.

[70] E.M. Vinod, K. Ramesh, and K.S. Sangunni. Structural transition and enhanced phase transition properties of se doped ge 2 sb 2 te 5 alloys. *Scientific reports*, 5:8050, 2015.

[71] J. Lee, E. Bozorg-Grayeli, S. Kim, M. Asheghi, H-S. Philip Wong, and K.E. Goodson. Phonon and electron transport through ge2sb2te5 films and interfaces bounded by metals. *Applied Physics Letters*, 102(19): 191911, 2013.

[72] S. Mukhopadhyay, J. Sun, A. Subedi, T. Siegrist, and D.J. Singh. Competing covalent and ionic bonding in ge-sb-te phase change materials. *Scientific reports*, 6:25981, 2016.

[73] T.H. Lee and S.R. Elliott. The relation between chemical bonding and ultrafast crystal growth. *Advanced Materials*, 29(24):1700814, 2017.

[74] H.L. Kagdada, K.J. Prafulla, Ś. Piotr, and K.J. Krzysztof. Structural stability, dynamical stability, thermoelectric properties, and elastic properties of gete at high pressure. *Physical Review B*, 97(13):134105, 2018.

[75] D. Campi, L. Paulatto, G. Fugallo, F. Mauri, and M. Bernasconi. First-principles calculation of lattice thermal conductivity in crystalline phase change materials: Gete, sb 2 te 3, and ge 2 sb 2 te 5. *Physical Review B*, 95(2):024311, 2017.

[76] K. Jeong, S. Park, D. Park, M. Ahn, J. Han, W. Yang, H-S. Jeong, and M-H. Cho. Evolution of crystal structures in gete during phase transition. *Scientific reports*, 7:955, 2017.

[77] G. Kalra and S. Murugavel. The role of atomic vacancies on phonon confinement in α-gete. *AIP Advances*, 5(4):047127, 2015.

[78] K.S. Andrikopoulos, S.N. Yannopoulos, A.V. Kolobov, P. Fons, and J. Tominaga. Raman scattering study of gete and ge2sb2te5 phase-change materials. *Journal of Physics and Chemistry of Solids*, 68(5-6):1074–1078, 2007.

[79] P. Němec, V. Nazabal, A. Moréac, J. Gutwirth, L. Beneš, and M. Frumar. Amorphous and crystallized ge–sb–te thin films deposited by pulsed laser: Local structure using raman scattering spectroscopy. *Materials Chemistry and Physics*, 136(2-3):935–941, 2012.

[80] J. Xu, C. Qi, L. Chen, L. Zheng, and Q. Xie. The microstructural changes of ge2sb2te5 thin film during crystallization process. *AIP Advances*, 8(5): 055006, 2018.

[81] S. Kozyukhin, M. Veres, H.P. Nguyen, A. Ingram, and V. Kudoyarova. Structural changes in doped ge2sb2te5 thin films studied by raman spectroscopy. *Physics Procedia*, 44:82–90, 2013.

[82] L. Bo, S. Zhi-Tang, Z. Ting, F. Song-Lin, and C. Bomy. Raman spectra and xps studies of phase changes in ge2sb2te5 films. *Chinese Physics*, 13 (11):1947, 2004.

[83] M.G. Beghi, F. Di Fonzo, S. Pietralunga, C. Ubaldi, and C.E. Bottani. Precision and accuracy in film stiffness measurement by brillouin spectroscopy. *Review of Scientific Instruments*, 82(5):053107, 2011.

[84] I.-M. Park, J.-K. Jung, S.-O. Ryu, K.-J. Choi, B.-G. Yu, Y.-B. Park, S.M. Han, and Y.-C. Joo. Thermomechanical properties and mechanical stresses of ge2sb2te5 films in phase-change random access memory. *Thin Solid Films*, 517(2):848–852, 2008.

[85] G. D'Arrigo, A. Mio, G. Favaro, M. Calabretta, A. Sitta, A. Sciuto, M. Russo, M. Calì, M. Oliveri, and E. Rimini. Mechanical properties of amorphous ge2sb2te5 thin layers. *Surface and Coatings Technology*, 355:227–233, 2018.

[86] R. Cecchini, K. Kohary, A. Fernández, M. Cabibbo, and A. Marmier. Determination of the anisotropic elastic properties of rocksalt ge2sb2te5 by xrd, residual stress, and dft. *The Journal of Physical Chemistry C*, 120(10):5624–5629, 2016.

[87] T. Blachowicz, M.G. Beghi, G. Güntherodt, B. Beschoten, H. Dieker, and M. Wuttig. Crystalline phases in the ge sb 2 te 4 alloy system: Phase transitions and elastic properties. *Journal of Applied Physics*, 102(9): 093519, 2007.

[88] K.M. Rabe and J.D. Joannopoulos. Structural properties of gete at t=0. *Physical Review B*, 36(6):3319, 3324.

[89] S. Perumal, S. Roychowdhury, and K. Biswas. High performance thermoelectric materials and devices based on gete. *Journal of Materials Chemistry C*, 4(32):7520–7536, 2016.

[90] V. Giraud, J. Cluzel, V. Sousa, A. Jacquot, A. Dauscher, B. Lenoir, H. Scherrer, and S. Romer. Thermal characterization and analysis of phase change random access memory. *Journal of Applied Physics*, 98(1): 013520, 2005.

[91] S. Roychowdhury, M. Samanta, S. Perumal, and K. Biswas. Germanium chalcogenide thermoelectrics: electronic structure modulation and low lattice thermal conductivity. *Chemistry of Materials*, 30(17):5799–5813, 2018.

[92] R. Fallica, E. Varesi, L. Fumagalli, S. Spadoni, M. Longo, and C. Wiemer. Effect of nitrogen doping on the thermal conductivity of gete thin films. *physica status solidi (RRL)–Rapid Research Letters*, 7(12):1107–1111, 2013.

[93] A. Kusiak, J.-L. Battaglia, P. Noé, V. Sousa, and F. Fillot. Thermal conductivity of carbon doped gete thin films in amorphous and crystalline state measured by modulated photo thermal radiometry. *Journal of Physics: Conference Series*, 745:032104, 2016.

[94] R. Lan, R. Endo, M. Kuwahara, Y. Kobayashi, and M. Susa. Electrical and heat conduction mechanisms of gete alloy for phase change memory application. *Journal of Applied Physics*, 112(5):053712, 2012.